July 2021

Designing Stimuli-Responsive Nanocomposites to Investigate Interface Dynamics

Huyen Vu
University of Massachusetts Amherst

DESIGNING STIMULI-RESPONSIVE NANOCOMPOSITES TO INVESTIGATE INTERFACE DYNAMICS

A Dissertation Presented

by

HUYEN VU

Submitted to the Graduate School of the
University of Massachusetts Amherst in partial fulfillment
of the degree requirements for the degree of

DOCTOR OF PHILOSOPHY

May 2021

Polymer Science and Engineering

DESIGNING STIMULI-RESPONSIVE NANOCOMPOSITES TO INVESTIGATE INTERFACE DYNAMICS

A Dissertation Presented

by

HUYEN VU

Approved as to style and content by:

_____

E. Bryan Coughlin, Chair

_____

Kenneth Carter, Member

_____

S. Thayumanavan, Member

_____

David A. Hoagland, Department Head
Polymer Science and Engineering

ACKNOWLEDGEMENTS

Foremost, I would like to thank my advisor, Professor E. Bryan Coughlin, for all of his guidance and support during my Ph.D. journey. He has shaped me to the scientist that I am today. From Bryan, I have learned to constantly be curious and asking questions because you never know what scientific discovery you might stumble upon. I always appreciate Bryan utilizing my mishaps and turning them into teaching moments to further improve me for the future. Thank you for being a great mentor and my academic father for these last five years and bestowing me with wisdom that I can carry forward in my career.

I would like to thank my committee members Professor Kenneth Carter and Professor Thayumanavan for their insightful discussions and feedback to my work. Their thought-provoking questions challenged me to look at my work from different angles in order to have a better understanding overall. I greatly appreciate their vast expertise that has provided guidance for my research and encouraging me to become a better scientist with a breath of knowledge.

I also had the opportunity to work with exceptional scientists at UMass and NIST throughout my graduate career. Their assistance enhanced my research projects in ways that I cannot do on my own. I would especially like to thank my collaborators at NIST, Dr. Jeffrey Gilman and Dr. Jeremiah Woodcock, for providing their expertise and guiding me through my research projects. I always enjoyed the in-person and virtual meetings to discuss science; your passion and enthusiasm for science explorations were contagious! I would also like to thank Dr. Weiguo Hu for his help in teaching me everything NMR related and his assistance in solid-state NMR experiments and Dr. James Chambers for his

constant assistance with fluorescence microscopy. I would also like to thank NIST for financially supporting my Ph.D. research through the Graduate Fellowship for STEM Diversity.

Through the course of my time here in PSE, I was fortunate to have the Coughlin Group family to support me through this journey. I would like to thank Dr. Rohit Gupta, Dr. Chinomso Nwosu, Dr. Joshua Enokida for being great mentors and teaching me everything in the lab as well as helping me navigate life after graduate school. I also want to thank the current group, Yifeng Du, Christian Steinmetz, Ria Ghosh, Anne Radzanowski, Roshni Chethalen, Yuhui (Helen) Du, for being my research family. I will hold dear to memories of our ventures outside of lab (when we had the chance) and our group lunches/dinners to relax and bond over food. In addition, I would like to thank the visiting Mainz students Nico Alleva, Matay Kaplan, and Adrian Hauck for sharing many joy and laughter with our group during their stay.

I am also grateful to have awesome roommates to keep me sane and having stress-relief activities outside of the Conte walls. For those memorable memories, I have to thank Daniel Camarda, Dr. Joshua Enokida, and James Pagaduan. We started many traditions like putting up the festive Christmas tree, roommate Christmas party, and countless movie nights! My graduate school experience would not be the same without you guys and I will miss you all dearly.

Of course, I want to thank the Class of 2016 for being there through my time here. I want to call out Daniel Camarda, Liz Stubbs, David Limberg, and Minjung Lee for being my support crew since our first year as we all went through the tough period of classes and CUMES together. Honestly do not know if I could have survived without you all. There

have been other troopers that came to my rescue, Hazel Davis, Ipek Sacligil, James Pagaduan, Ria Ghosh, Zach Fink, and Emily Maling, whether for a game night or a safety blanket in social situations. Thank you for willing to read over my documents and listen to my practice talks without a sigh. You all have brought me so much laughter and will always have a special place in my heart. I want to thank my partner in crime, Chris Cueto, for being there for me when I struggled with graduate school. You were willing to cook delicious meals while I was stressed by deadlines and milestones. I am grateful to have you in my life and as someone for me to lean on.

Most importantly, I am especially thankful for my family. Their endless love and support allowed me to get through some of the toughest challenges I encountered. From our weekly phone calls, they constantly reminded me of the big picture and how everything will work out in the end. Words cannot simply describe the sacrifices they endured for me to pursue my dream of being a scientist.

ABSTRACT

DESIGNING STIMULI-RESPONSIVE NANOCOMPOSITES TO INVESTIGATE INTERFACE DYNAMICS

MAY 2021

HUYEN VU, B.S., WORCESTER POLYTECHNIC INSTITUTE

M.S., UNIVERSITY OF MASSACHUSETTS AMHERST

Ph.D., UNIVERSITY OF MASSACHUSETTS AMHERST

Directed by: Professor E. Bryan Coughlin

Inspired by nature, this research focuses on designing multifunctional renewable nanocomposites with high toughness and stimuli-responsiveness. In recent years, cellulose nanocrystals (CNCs) have been explored due to their abundance, renewable resource, and unique mechanical strength and structural coloration. CNCs naturally self-assemble into the helicoidal (Bouligand) structure that effectively endure high impacts but is brittle without an attendant soft phase. A thermoresponsive polymer was incorporated into CNCs via evaporation-induced self-assembly to improve toughness of the resulting nanocomposites and to study responses in polymer dynamics under varying temperature and humidity conditions.

In the first project, poly(diethylene glycol methyl ether methacrylate) $PMEO_2MA$, with a lower critical solution temperature (LCST) of 26 °C, was blended with CNCs to form free-standing films through controlled evaporation-induced self-assembly. The CNCs structures were tuned by polymer loadings, humidity, and temperature conditions and

caused changes to structural colors of the resulting CNC nanocomposite films. Simply by increasing polymer loading from pure CNCs to 30 mass % of $PMEO_2MA$, the reflected color maxima transitioned from blue to red that corresponded to 530 nm $\pm$ 50 nm to 770 nm $\pm$ 90 nm. The reflected colors further shifted their reflectance wavelength by 140 nm to 200 nm when the films were exposed to 95 % RH. The CNCs contributed to the shift due to their hydrophilic nature that absorbed water molecules and expanded the structures. The process was reverted when water evaporated from the films and the reflected colors returned to the initial state. The resulting films demonstrated reversible responses to temperatures, going from transparent to opaque for temperatures below and above the LCST. The optical responses were detected within the visible light spectrum, making the CNC nanocomposites ideal in applications for materials sensitive to human-contact.

In the second project, the focus was on a microscopic scale response of $PMEO_2MA$ by implementing a water-sensitive dye to probe the chains dynamics via fluorescence lifetimes. The $PMEO_2MA$ homopolymer was labeled with the rhodamine B-based water-sensitive dye to make $PMEO_2MARhB$ then blended with CNCs. Fluorescence lifetime imaging microscopy (FLIM) generated a fluorescence lifetime distribution within the film that probed the different polymer dynamics. The average fluorescence lifetimes (τ_m) shifted to shorter lifetime with increasing $PMEO_2MARhB$ loadings from 3.1 ns to 2.4 ns. Two-component exponential fitting was needed and resulted in τ_1 and τ_2 values. The τ_1 had shorter lifetimes that associated with more hydrated domains while τ_2 had longer fluorescence lifetimes that likely related to polymer confined to the CNC interfaces. There are three postulated environments the polymer chains were experiencing in the CNCs structure: i) $PMEO_2MA$ confined to CNCs via physical absorption, ii) $PMEO_2MA$ in-

between CNCs structures, iii) $PMEO_2MA$ in hydrated regions. FLIM technique could be implemented in other water-sensitive systems and filler-matrix interfaces to study dynamic responses in nanoseconds regime.

The final project examined how anchoring $PMEO_2MARhB$ to CNCs would affect polymer dynamics and mechanical properties. The *grafting-from* technique was utilized to covalently bond the polymer chains to CNCs surface to form CNC-*g*-$PMEO_2MARhB$ with 74 % polymer content. The CNC-*g*-$PMEO_2MARhB$ was blended with pristine CNCs to make free-standing films. Due to one chain-end being restricted to CNCs, the Grafted-CNC films had longer fluorescence lifetimes when compared to their blended $PMEO_2MARhB$-CNC counterpart. The Grafted-CNC films showed improvement in tensile strength and modulus for 5 % and 15 % Grafted-CNC, indicating better stress-transfer in comparison to the blended $PMEO_2MARhB$-CNC. However, due to the polymer chains tethered to the CNCs surface, there was no excess polymer content present to lubricate the CNC rods. Therefore, the strain and toughness suffered at 40 % Grafted-CNC and the performance was dropped by a factor of three when comparing with the 30 % $PMEO_2MARhB$-CNC since they have comparable polymer content. This observation illustrated a correlation between the measured fluorescence lifetime and mechanical properties.

From these studies, CNCs nanocomposites can be tuned by environmental stimuli and different chain confinement resulted in optical responses and mechanical performances. Fluorescence lifetime imaging microscopy was co-opted from biological applications to capture sensitive events in nanoseconds at high resolution to experimentally study polymer dynamics. The technique provided insights at the microscopic scale to improve material design for CNCs nanocomposites.

TABLE OF CONTENTS

Page

LIST OF TABLES

Table Page

LIST OF FIGURES

Figure Page

LIST OF ABBREVIATIONS

ATRP	Atom transfer radical polymerization
BiB	α-bromoisobutyryl bromide
BDS	Broadband dielectric spectroscopy
CNCs	Cellulose nanocrystals
CNC-*g*-$PMEO_2MA$	Cellulose nanocrystals grafted poly(diethylene glycol methyl ether methacrylate)
CNC-*g*-$PMEO_2MA$RhB	Cellulose nanocrystals grafted poly(diethylene glycol methyl ether methacrylate-*co*-Rhodamine B methacrylate)
DMA	Dynamic mechanical analysis
DSC	Differential scanning calorimetry
EBriB	Ethyl α-bromoisobutyrate
EISA	Evaporation-induced self-assembly
ESI-TOF	Electrospray Ionization Time-of-Flight
FLIM	Fluorescence lifetime imaging microscopy
FT-IR	Fourier-transform infrared spectroscopy
GPC	Gel permeation chromatography
LCST	Lower critical solution temperature
MEO_2MA	Diethylene glycol methyl ether methacrylate
NIST	National Institute of Standards and Technology
NMR	Nuclear magnetic resonance
NSE	Neutron spin echo
$OEGMA_{300}$	Oligoethylene glycol) methyl ether methacrylate
PEO	Polyethylene oxide
PMDETA	*N,N,N',N'',N''*-Pentamethyldiethylenetriamine
$PMEO_2MA$	Poly(diethylene glycol methyl ether methacrylate)
$PMEO_2MA$RhB	Poly(diethylene glycol methyl ether methacrylate-*co*-Rhodamine B methacrylate)
$POEGMA_{300}$	Poly(oligoethylene glycol) methyl ether methacrylate
POEGMARhB	Poly(oligoethylene glycol) methyl ether methacrylate-*co*-Rhodamine B methacrylate)
POM	Polarized optical microscopy
QENS	Quasi-elastic neutron scattering
RH	Relative humidity
RhB	Rhodamine-B
SEM	Scanning electron microscope
TEA	Triethylamine
T_g	Glass transition
TGA	Thermogravimetric analysis
TMDSC	Temperature modulated differential scanning calorimetry
τ_1, τ_2	Tau 1, Tau 2 (shorter and longer fluorescence lifetime)
τ_m	Tau m (average fluorescence lifetime)
UV-Vis spectroscopy	Ultraviolet-visible spectroscopy
VFT	Vogel-Fulcher-Tammann

CHAPTER 1. INTRODUCTION

Cellulose is an abundant, renewable resource that has been used in the paper industry. With the discovery of cellulose nanocrystals (CNCs) around the 1950s, there has been a renewed interest recently to expand applications of CNCs into pharmaceuticals, the food industry, and composites.[1,2] Unlike traditional cellulose, cellulose nanocrystals self-assemble into helical structures, also called Bouligand structures, that allow them to have high strength. These Bouligand structures are also seen in the architecture of crustacean exoskeleton, such as crabs,[3] lobsters,[4] and mantis shrimp.[5] Alternating hard and soft phases provide a material that is both tough without being too flexible.[6] With CNCs strong mechanical properties coupled with their renewable and biodegradable nature, recent literature has explored their utilization for the next generation of nanocomposites that could mimic the design of biological composites and be responsive to external stimuli.

1.1. Introduction to Cellulose Nanocrystals

Cellulose is an abundant, renewable linear polymer, with β(1→4)-linked D-glucose units (**Figure 1.1**), that forms fibrils comprising amorphous and crystalline domains. Cellulose chains are held together by intra and interchain hydrogen bonding. The fibrils have elastic modulus of about 150 GPa and strength of roughly 10 GPa. Rånby isolated cellulose crystalline domains, called cellulose nanocrystals, by strong acid hydrolysis of cellulose.[1,2] A CNC rod has a degree of polymerization between 90 and 110 with approximately 3.7-6.7 sulfate groups per 100 glucose units. The sulfate esters at the surface of CNC provide additional electrostatic stability in aqueous suspensions. At a critical concentration, the suspension is birefringent. Hydrolysis can also be performed with hydrochloric, sulfuric, and phosphoric acids but the former hydrolysis does not form ester

groups. Due to the absence of ester groups, HCl-hydrolyzed CNCs have difficulty forming chiral nematic structures.[2]

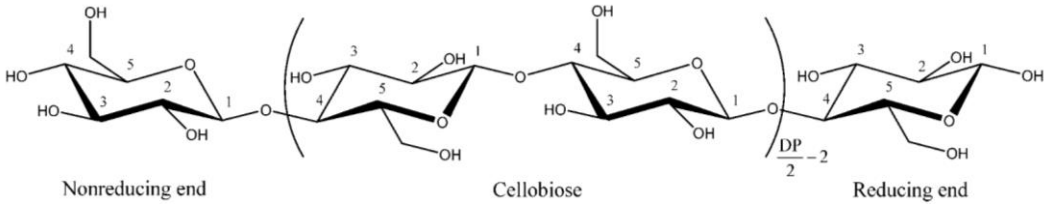

Figure 1.1. Repeating unit structure of cellulose. Image was taken from Ref. 1.

The most common source of cellulose nanocrystals is woody biomass but other sources of cellulosic materials can be derived from bacteria, tunicate, or cotton. An individual CNC rod is made of roughly 9 cellulose chains with the cross section of 5 nm − 15 nm in width and 90 nm −120 nm in length, resulting in an aspect ratio of 20 for wood pulp sources having 60 % crystallinity.[2] Depending on the source, the dimension of the CNC rods can vary. For the tunicate-CNCs, the length is about 1000 nm with an aspect ratio of 100 and a higher crystallinity of 80 %.[7,8] Due to the high cost and limited supply of tunicate-CNC, it is not commonly used despite its good mechanical properties. One advantage of using CNC is its high specific surface area of ~400 g/cm^2, which is about 100 times the surface area of the starting cellulosic material. CNCs have many other desirable properties, such as strength, self-assembly, photonic properties, and being lightweight that have expanded their applications as rheology modifiers, emulsion stabilizers, sensors, and reinforcement for polymer matrices.[2]

1.2. Structure and Mechanical Properties of Cellulose Nanocrystals

In a dilute aqueous suspension, the CNCs are isotropic. When the CNCs suspension undergoes evaporation-induced self-assembly, the rods arrange themselves into liquid

crystalline assemblies to decrease the electrostatic interactions, resulting in anisotropy due to the unidirectional orientation of the rods. When characterized by polarized optical microscopy (POM), this arrangement has a "fingerprint" patterns, showing left-handed chiral-nematic ordering, that gives an iridescent appearance. The chiral-nematic structures composed of stacked planes of CNC rods; the rods in each plane are aligned in one direction, is shown in **Figure 1.2**. The planes are rotated around the perpendicular axis due to entropically driven self-arrangement. This twisted plywood assembly is also called a Bouligand structure. It is possibly formed because of the twist dimension and the charge surface of CNC rods.[1,9]

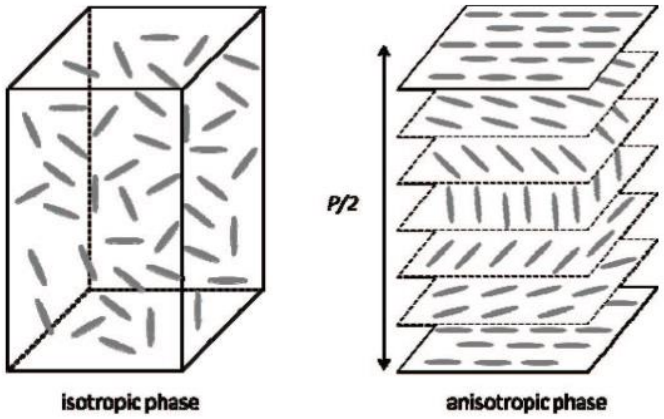

Figure 1.2. Orientation of the dilute (left) and concentrated (right) suspension of CNC in aqueous solution. Image was taken from Ref. 1.

There are several ways to tune the pitch length, such as the CNC dimensions, surface charge, the conditions of the evaporation-induced self-assembly process, and external stimuli (temperature and/or humidity). The concentration of CNCs suspension has a great effect on the pitch and reflectance wavelength; higher concentrations result in lower pitch and shorter reflectance wavelength and vice versa. Adding electrolytes disrupts the electrostatic repulsions by screening some of the negative charges of the sulfate groups,

resulting in a reduced pitch length. Interestingly, films dried at ambient conditions tend to have polydomain structures, resulting in inhomogeneity. Applying a magnetic field during the drying process can help align the CNC rods leading to more homogeneity.[10] Another method to influence the pitch is the drying rate; a slow drying rate of - 4 mg/min of water evaporation resulted in a very low pitch of 420 nm when compared to a faster drying rate of -13 mg/min (pitch = 1000 nm), **Figure 1.3**. At a slower drying rate, the CNC rods have more time to rearrange themselves into a tighter organization. Faster drying rates result in the rods restricted to configurations where the pitch tends to have broadened distribution and longer length.[11]

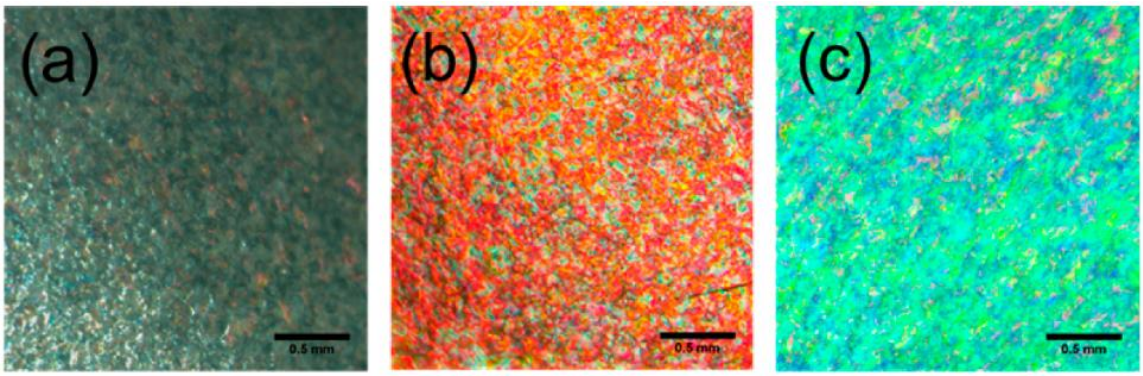

Figure 1.3. Polarized optical microscopy images of sodium-neutralized sulfated wood cellulose nanocrystals (Na-CNCs) at a) fast-dried (13 mg/min), b) slow-dried (7 mg/min), c) slowest-dried (4 mg/min). The images are obtained in cross-polarization configuration with 0.5 mm scale bar. Images taken from Ref. 11.

Bouligand structures observed in biological nanocomposites, like the exoskeleton of crabs,[3] lobsters,[4] and mantis shrimp,[5] provide greater mechanical integrity. Unlike CNC, biological nanocomposites have alternating layers of hard (helical configuration) and soft phases. This organized configuration prevents crack propagation by crack bridging, twisting, and deflecting the applied force to endure high impact energy while the soft phase acts as an energy-dissipating matrix.[3–6,12,13] Due to the helical arrangement, CNCs have

modulus of 10 GPa.[7] Based on axial Young's modulus, CNCs are theoretically stronger than steel with the native cellulose perfect crystal expected to have a modulus of 167.5 GPa. The high moduli make them candidates for advanced materials.[7,11,14,15]

The Bouligand structure is also responsible for the iridescence structural colors observed in some insects, for example the jewel beetle, **Figure 1.4**. For CNCs, the iridescent feature is observed when the distance of helical structure repeat unit – known as the pitch – is within the wavelengths of visible light.[10,13] The structure reflects circularly polarized light and the reflected light depends on the viewing angle, giving the iridescent appearance.[2,14] This has allowed CNCs to have applications in photonic materials, security papers (passports, banknotes), polarizing mirrors, packaging materials, sensors, as well as additives for paints and inks.[1,10]

Figure 1.4. Structural coloration and circularly polarized light reflection from jewel scarabs due to Bouligand structures. Image taken from Ref. 13.

1.3. Cellulose Nanocrystals Applications in Nanocomposites

Biological nanocomposites mentioned above have great mechanical properties due to high component of reinforcement (hard phase) that have an energy-dissipating soft phase to complement the composite system. This organization is different from engineered materials that generally have low loading of reinforcements that are usually at nanoscale lengths. Dispersion remains a challenge since the nanoparticles aggregate in the matrices, jeopardizing mechanical properties of the resulting composites.[1,9] Taking a new direction

from the previous approach for composites, the next generation of nanocomposites will take inspiration from nature's complex hierarchical ordering to enhance mechanical properties.[9]

There has been a focus of using cellulose nanocrystals for reinforcement of nanocomposites due to their ability to self-assemble into Bouligand structures, abundancy, low cost, lightweight (density = 1.61 g/cm^3), and high surface area.[1,9] Many literature reports embedded neat or functionalized CNCs into polymer matrices for applications in composites, photonic materials, and sensors.[2,14,16] Despite their advantages, CNCs suffer from brittleness due to the absence of an energy-dissipating binder phase. CNCs hydrophilic nature make it more straightforward to blend CNCs with water-based polymers to incorporate a soft phase.[7,9,14] Hydrophilic polymer matrices explored, include poly(vinyl alcohol) (PVOH),[9] waterborne polyurethane (WPU),[17] polyethylene oxide (PEO),[18] zwitterionic surfactant dimethyl(myristylammonio) propanesulfonate (DMAPs),[19] and copolymers of methacrylate derivatives with a 1-ureido-4-pyrimidinone group with a hydrogen-bonding motif to enhance ductility along with photonic properties.[15] Nanocomposite films were formed via evaporation-induced self-assembly from aqueous suspensions of CNCs and water-based polymers.[1] A recent study blended two different sources of CNCs, wood and tunicate, yielded optimized toughness and strength with a combination of 70 mass % wood-CNCs and 30 mass % tunicate-CNCs. These nanocomposites are promising for use in automotive, aerospace, infrastructure, and decorative coatings.[7] Another method to embed CNCs into a matrix is *in-situ* polymerization, to create a homogeneous incorporation within an elastomer that was stimuli-responsive by changing color as the material was stretched due to the unwinding

of the CNCs Bouligand structure.[20] Without modification, CNCs are only compatible with water-based polymer and dispersible polymer latexes.[1]

To blend CNCs with hydrophobic polymer matrices, research has focused on surface modifying CNCs to aid their dispersion. CNCs dispersity is vital to ensure enhancement in mechanical properties that is not hindered by aggregation.[1] To increase compatibility between CNCs and nonpolar matrices, one study grafted PEG chains to CNCs to help disperse the nanoparticles into poly(lactic acid) (PLA),[21] while another literature study used ring-opening polymerization to graft poly(ε-caprolactone) (PCL) to later blend with PCL[22]. There have been many studies on grafting thermoresponsive polymers to CNCs to create a stimuli-responsive CNCs in aqueous solution for various applications like sensors or thermo-sensitive materials.[23–29] These studies did not examine how thermoresponsive polymer will respond to various humidity levels and their ability to exclude water above the lower critical solution temperature (LCST) to protect CNCs from water penetration.

1.4. Water coverage on CNCs

Cellulose nanocrystals hydrophilic nature makes them prone to absorb water. The excess moisture at the CNCs surface affects dispersion, interfacial adhesion, and hydrothermal stability. CNCs dispersion is limited to polar solvents, making it difficult to disperse them in nonpolar solvents.[11] Despite functionalizing CNCs, and using solvent exchange to organic solvents in order to remove the water component, a layer of water surrounding CNCs surface is still present.[30,31] The layer of water prevents interfacial adhesion between CNC-matrix and CNC-CNC, more severely in hydrophobic matrices. When CNCs absorb water, they can act as water channels within the matrices, decreasing mechanical properties as a result.[32,33] A simulation study has looked at how moisture

influences CNCs interfaces observed the CNC-CNC shear modulus to drop by 2 orders of magnitude when the interface went from dry to wet, **Figure 1.5**.[33] Therefore, it is crucial to study the interaction between water and CNCs and correlate how the physical properties might be compromised.

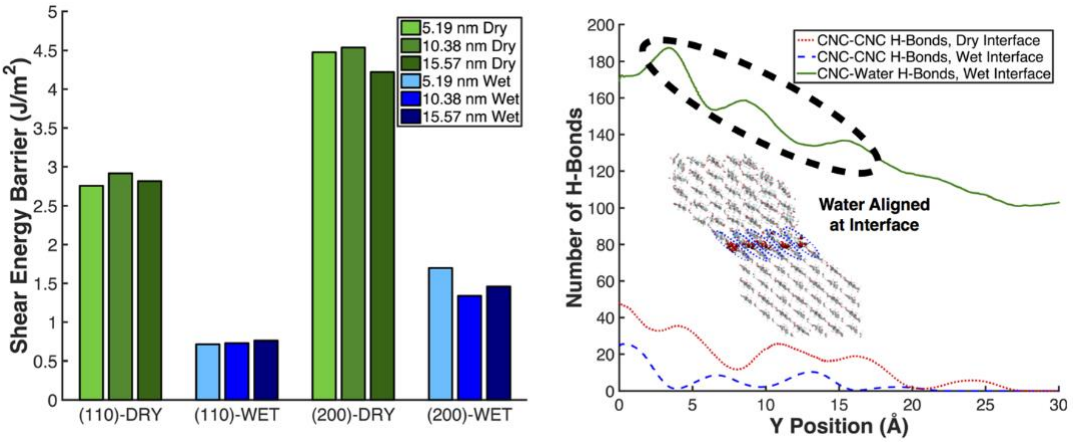

Figure 1.5. Shear energy barriers for dry interfaces (green bars) and wet interfaces (blue bars) showing how water at the interface decrease energy barriers to traction and interlayer shear modulus (left). Compared to dry and wet interfaces that reveals water-CNC hydrogen bonds replacing CNC-CNC hydrogen bonds for (110) interfaces (right). Image taken from Ref. 33.

A previous study done by our NIST collaborators looked into confined water in CNCs by measuring the dielectric constant using a noncontact microwave cavity perturbation method.[11] The study was able to probe the dimensions of the absorbed water on CNCs and the factors that affected water confinement. Between the sulfated-CNCs neutralized with either sodium (Na-CNC) or methyl (triphenyl) phosphonium cations ($MePh_3P$-CNC), the study found that the more hydrophobic cations ($MePh_3P$-CNC) yielded shorter pitch and spherical water confinement. However, to minimize the water content surrounding CNCs, we need have a polymer system that is compatible with CNCs (having hydrophilic characteristics), but also has the ability to exclude water from CNCs surface.

1.5. Thermoresponsive Polymers

Thermoresponsive polymers are triggered by a temperature change in the environment, resulting in a new polymer configuration that translates to a physical property change. A polymer in a solvent system would go through a phase separation brought on by a temperature change, and thus transition from a single phase to a two phase state. Two thermoresponsive changes can occur, either a lower critical solution temperature (LCST) or upper critical solution temperature (UCST), as shown in **Figure 1.6**. When phase separation occurs as temperature increases, the system demonstrates LCST behavior. A LCST is the minimum temperature where phase separation can occur. For the UCST case, the phase separation happens when temperature decreases. For the two cases, the polymer is not precipitating but is in equilibrium where one phase is polymer rich (high in concentration) while the other is polymer poor (low in concentration). Polymers with LCST behavior have been implemented in many biomedical applications.[34]

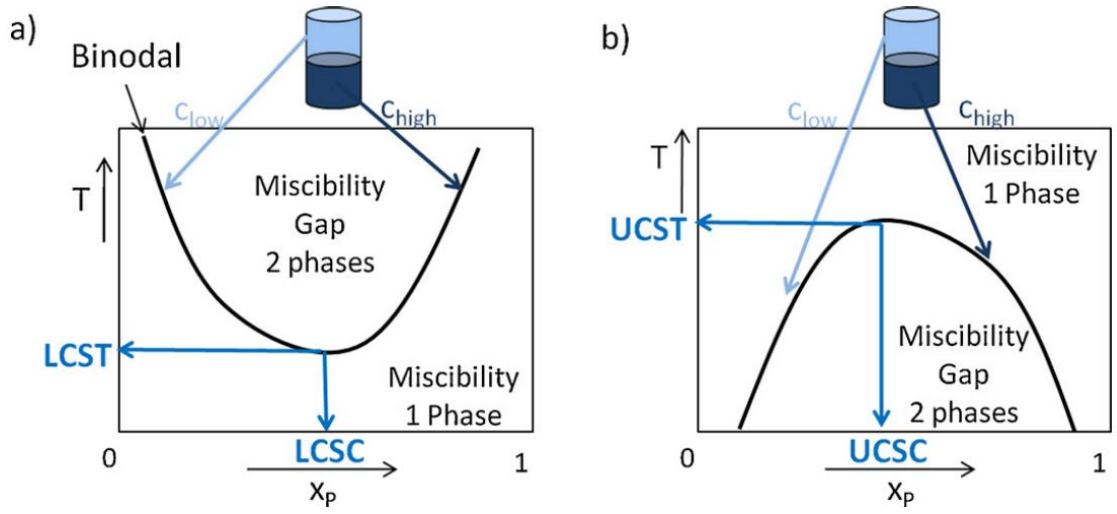

Figure 1.6. Phase diagram for polymer-solvent system with a) LCST and b) UCST behaviors. Figure was taken from Ref. 34.

Some common LCST polymers are poly(N,N'-diethyl acrylamide), poly(dimethylaminoethyl methacrylate), poly(N-acryloylpyrrolidine), poly(vinyl methyl

ether), and poly(N-isopropylacrylamide) (PNIPPAm).[23–29] Interestingly, PNIPPAm is the most common due to its LCST around 32 °C, which is close to the human body temperature. However, it has disadvantages in that it undergoes an irreversible phase transition, and for low molecular weight polymers, the end-groups greatly influence the thermal properties.[35]

In the 2000s, the discovery of oligo (ethylene oxide) methacrylate monomers expanded the library of accessible LCST polymers. Starting with the methacrylic acid, oligo ethylene oxide (ranging from one to nine PEO units) can be attached as the pendant ester groups. For the two ethylene oxide units, 2-(2-methoxyethoxy) ethyl methacrylate (MEO_2MA) has an LCST at 26 °C while $OEGMA_{475}$ (8-9 PEO units) has an LCST of 90 °C (**Figure 1.7**).[35,36] The shift in LCSTs is due to the increase in PEO chain length that increases the hydrophilicity of the polymer in aqueous solution, the solution needs to be heated to a higher temperature before $POEGMA_{475}$ exhibits a phase transition.[34]

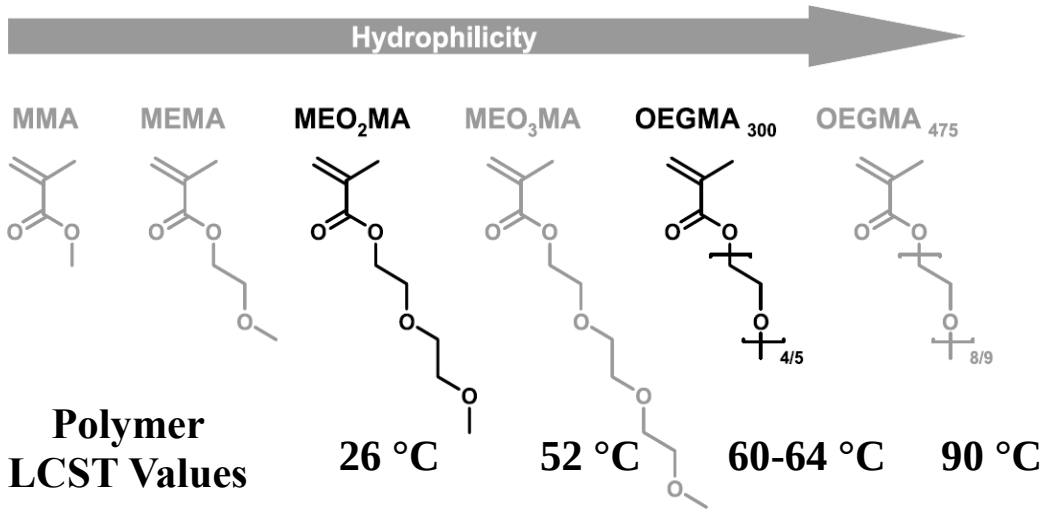

Figure 1.7. The structures of the oligo (ethylene oxide) methacrylate family and their corresponding polymers' LCSTs are listed below the monomer. Figure was modified from Ref. 35.

Lutz was able to co-polymerize MEO_2MA with $OEGMA_{475}$ at different mole ratios to obtain LCST values between 26 °C and 90 °C via ATRP.[35,36] This tuned LCST value could then target 32 °C to be analogous with PNIPPAm. Some advantages of the oligo (ethylene oxide) methacrylate are reversible phase transitions,[35,37] mainly unaffected by concentration in water and chain-length,[35] biocompatibility, and anti-fouling properties below LCST.[37] These advantages have allowed the oligo (ethylene oxide) methacrylate polymers to be used for drug-delivery, injectable hydrogels, cell-culture substrates, antibacterial surfaces, protein chromatography, and tissue engineering.[35,37]

For LCST polymers, their thermoresponsive ability is due to the balance between favorable and unfavorable interactions with water molecules.[35] Below the LCST value, the polymer chain is hydrophilic and forms hydrogen bonds with the surrounding water molecules. As the temperature increases, the hydrogen bonds would weaken.[34] Above LCST, the polymer-water bonding is less favorable than polymer-polymer interaction therefore the water molecules are expelled from polymer chains, resulting in polymer configuration that goes from coil to globule inducing phase separation.[34,35] Thermodynamically, the hydrogen bonding for polymer-polymer and water molecules is enthalpically favorable for free energy of mixing but the polymer-water bonding increases ordering. This increase ordering is not ideal for entropy of mixing, at high temperature, the entropy contribution $T\Delta S$ dominates and free energy of mixing becomes positive. This results in phase separation of the polymer from water, a proposed schematic is shown in **Figure 1.8**.[34]

The most common method to measure the phase transition for LCST polymers in aqueous solution is turbidimetry. At a fixed concentration, the transmittance of a solution is measured as temperature increases or decreases. At low temperatures, the solution is clear (100 % transmittance) and as temperature increases, the solution becomes opaque (< 50 % transmittance) because the polymer globules scatter light. When the temperature cools down, the polymer is again well-dispersed in water. Dynamic light scattering (DLS) can also measure this transition by recording the polymer size as it goes from coil to globule. The transition is endothermic so differential scanning calorimetry (DSC) and pressure perturbation calorimetry (PPC) can detect this phase transition by determining the enthalpy changes and volume change, respectively.[34]

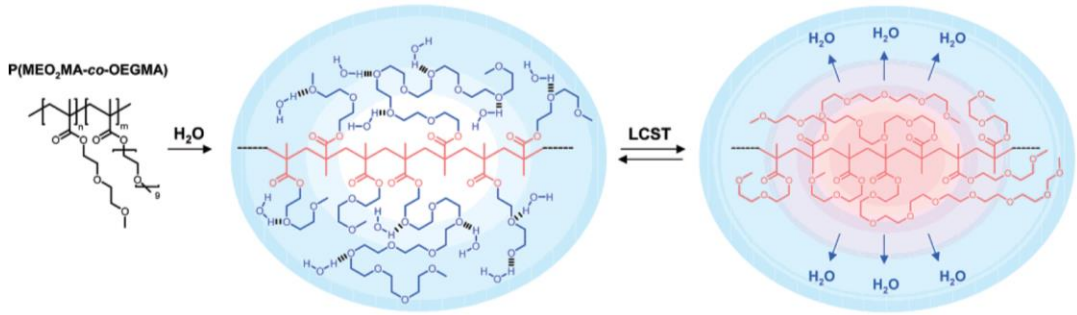

Figure 1.8. Proposed mechanism for temperature-induced phase transition of copolymers P(MEO$_2$MA-*co*-OEGMA) in aqueous solution. Schematic was taken from Ref. 34.

The LCST polymers have been explored in aqueous solution but only a few literature reports describe their behavior in the solid or dry state. Work from Lutz investigated the cross-linked networks of 10 mol % and 20 mol % OEGMA in P(MEO$_2$MA-*co*-OEGMA) swollen in water and they reported LCST values of 42-45 °C and 51-53 °C, respectively. When those temperatures were reached, the hydrogels deswelled and the gel collapsed, seen in **Figure 1.9**. The thermoresponsive behaviors observed were comparable to the corresponding uncrosslinked polymers.[35]

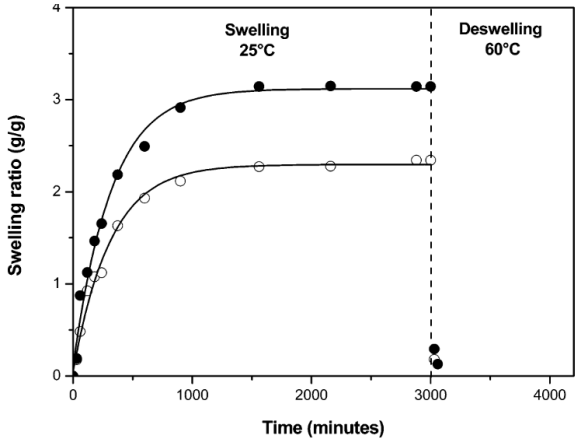

Figure 1.9. The swelling ratio as a function of time and temperature for P(MEO_2MA-*co*-OEGMA) hydrogels with 10 mol % and 20 mol % OEGMA at 60 °C. Taken from Ref. 35.

A recent study looked at gel networks of PNIPPAm with hydrophilic sodium alginate networks to absorb moisture from the atmosphere and excrete it in liquid form above the LCST value, in **Figure 1.10**. The gel system took in moisture at temperatures below 50 °C but would release about 20 mass % liquid water above 50 °C. Based on this study, the 80 % of water remained in the gel due to the alginate network that prevented the water from escaping. This absorb and desorb process is reversible.[38]

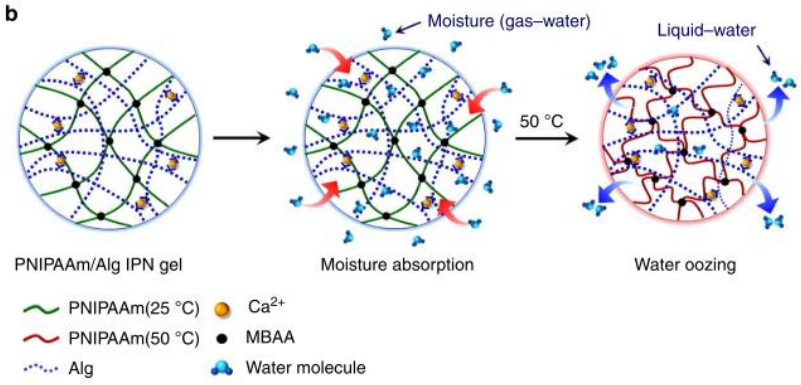

Figure 1.10. Illustration of the a) water-adsorption of dried PNIPPAm/Alg gel b) moisture absorption and oozing process of IPN gel with temperature fluctuation c) condensation of moisture with a standard absorbent. Image was taken from Ref. 38.

Some literature has utilized PNIPPAm hydrogel inverse opal particles as a drug delivery system due to its prominent temperature-induced volume change. The materials had a photonic band gap that allowed them to have structural colors and characteristic

reflection peaks. In **Figure 1.11,** the PNIPPam hydrogel particles where exposed to temperature ranges from ambient to 55 °C.[39] As the temperature is increased, the reflected colors transitioned from red to blue due to the contraction of the polymer system as it underwent phase transition. This example illustrated how the polymer configuration and volume change caused a linear color variation within the visible spectrum.

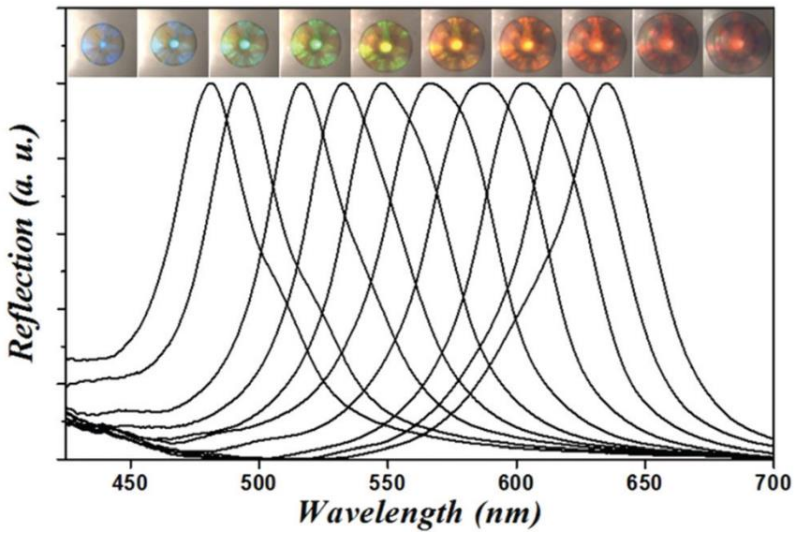

Figure 1.11. Reflection images and wavelength of the PNIPPAm hydrogel inverse opal particles from ambient to 55 °C. Image taken from Ref. 39.

1.6. Probing Interphase Dynamics

To understand structure-property relationships for composites, a focus has been on examining the interphase. The interphase region is where the filler and matrix interact, which would translate to bulk properties for the material.[40–42] The connectivity between the composite components is crucial to transfer stress from the matrix to filler. Despite a large volume of work dedicated to polymer nanocomposites, there is still a need to fundamentally understand polymer dynamics at different length scales. Understanding the microscopic polymer dynamics is vital to design and develop future materials with

desirable macroscopic properties. Fundamental studies on dynamic processes can provide insights to determine suitable processing methods and parameters for mass production and reduce costs.[43]

Polymer dynamics can have various meanings depending on the time and length scales measured, as seen in **Figure 1.12**. At the shortest levels, thermal vibrations are at the pico-second and sub-Ångstrom length-scale. Segmental dynamics happen at a range of time- and length scales, often defined as the non-diffusive polymer segments and polymer conformations.[44] Intermediate polymer dynamics entail non-diffusive relaxations and a collective motion of polymer segments, often described by a Rouse model in melts. The dynamics can be measured by neutron scattering and rheology.[45] Polymer chain diffusion has slower dynamics than segmental and intermediate processes and can be measured by rheology and neutron spin echo spectroscopy (NSE). As for nanoparticle diffusion, it has a wider range of time- and length-scales that depends on the size, volume fraction, dimension, and interaction of the nanoparticles. To measure the temporal fluctuations of these particles, X-ray photon correlation spectroscopy (XPCS) and dynamic light scattering (DLS) are often used to track the motions in polymer melt.[43]

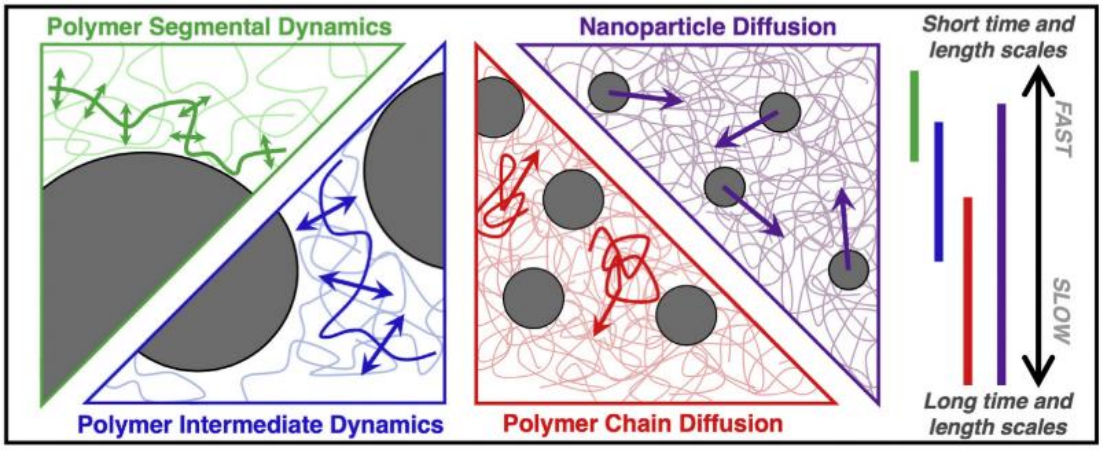

Figure 1.12. Schematic of the dynamic processes in nanocomposites based on time and length scales. Image taken from Ref. 43.

To understand and help design composites, many techniques and tools have been developed to probe polymer dynamics, as seen in **Figure 1.13**. For a slow relaxation time of 1 second at a temperature close to T_g, temperature modulated differential scanning calorimetry (TMDSC) is used to examine segmental dynamics.[46] At temperatures higher than T_g and dynamics in 10^{-7} s to 10^{0} s timescale, broadband dielectric spectroscopy (BDS) can probe a broad range of dynamics to the molecular level.[47] Despite its advantage, the technique is not length-scale selective, requires a permanent dipole on polymer system, and complex fitting.[48] Neutron spin echo spectroscopy (NSE) and quasi-elastic neutron scattering (QENS) can measure segmental dynamics in 10^{-11} s to 10^{-6} s at temperature significantly above T_g while providing length-scale information. The NSE technique is often used to measure intermediate dynamics (Rouse) while QENS measures the broadening of an elastic scattering peak that is dependent on hydrogen atoms in probe molecular relaxation.[49] Dynamic mechanical analysis (DMA), rheology, and NMR spectroscopy have been used to examine segmental and intermediate dynamics as well.[46]

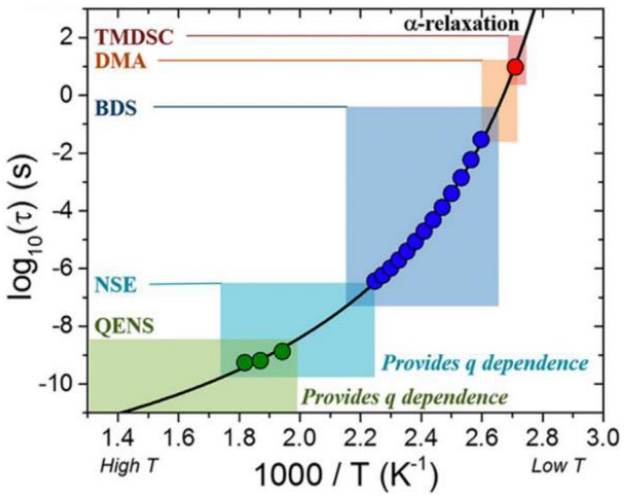

Figure 1.13. Diagram depicting segmental relaxation times of bulk 40 kg/mol P2VP as a function of inverse temperature and the corresponding temperature scale for techniques used to characterize polymer dynamics: TMDSC, DMA, BDS, NSE, and QENS. Black line represents a Vogel-Fulcher-Tammann (VFT) fit for TMDSC (red circle), BDS (blue circles), and QENS (green circles) measurements. Image taken from Ref. 50.

Segmental dynamics happen within nanometers length-scale and are sensitive to the local environments. Therefore, a range of dynamics exist because of the heterogeneous environments within the nanocomposites that is dependent on the polymer location in relation to the nanoparticles. Three models have been developed to describe different dynamics in polymer nanocomposites, **Figure 1.14**. The homogeneous model describes how the average dynamics encompass all the segmental dynamics in the material. The core-shell model indicates the existence of two dynamics that depend on the distance between polymer chains and the nanoparticles. Meanwhile, the interfacial layer model describes a gradual transition from interfacial to bulk dynamics. The nanoparticle-polymer interactions, nanoparticle size and volume fraction parameters often dictate which model is most suitable to describe segmental dynamics in polymer nanocomposites.[43]

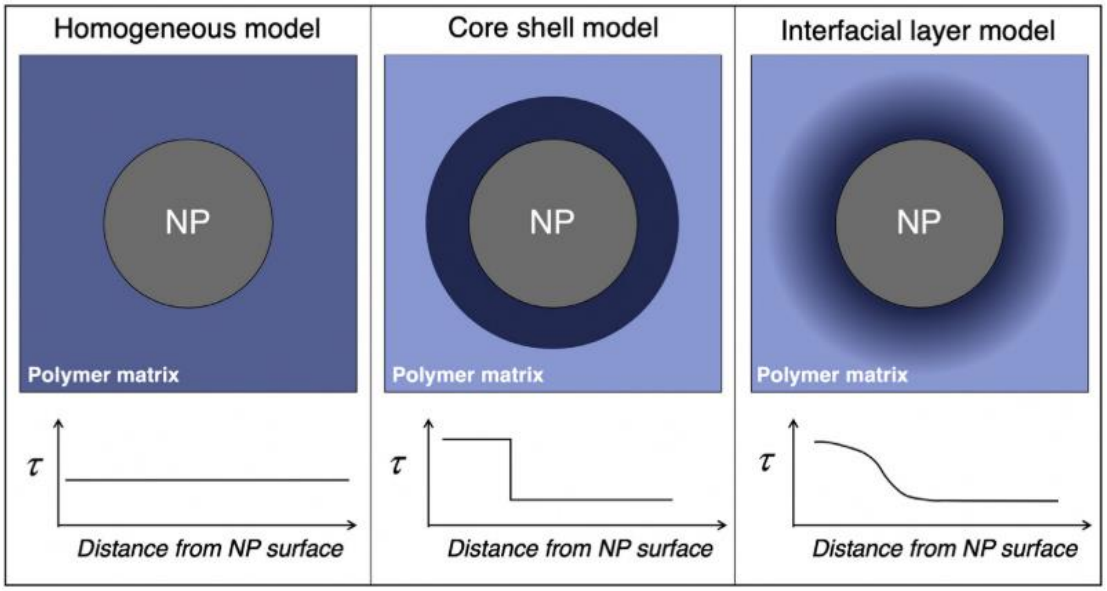

Figure 1.14. Schematic of three models describing polymer segmental dynamics as a function of distance from a nanoparticle. Image taken from Ref. 43.

More studies have looked into interfacial interactions utilizing neutron reflectivity or a fluorescence probe to understand the mechanical stress.[51,52] A study done by our NIST collaborators used a mechanophore covalently attached to silk fibers to directly observe the interphase portion when stress was applied. Using two-photon fluorescence lifetime imaging (TP-FLIM) and hyperspectral imaging, allowed for observation of the mechanophores activation during stress at the silk fiber interface.[41]

Using an optical output, some studies have looked at the glass transition (T_g) and how confinement affects polymer dynamics and segmental motion. There has been a focus on probing segmental motion by using fluorescent probes to measure glass transition (T_g). Techniques like ellipsometry, dielectric spectroscopy, and fluorescence spectroscopy have been used to measure T_g of thin films by examining the mobility of polymer chains at the sample-air interface. Some investigators have used the lattice "limited mobility" model to examine the mobility at these interfaces.[53] Work by Torkelson *et al.* looked into interfacial interactions of nanocomposites and how confinement influence T_g. He pioneered the usage of pyrene dyes to track chain mobility in bulk, and nanocomposite thin films based on the shift of fluorescence intensity. These studies found that confinement can result in a shift of glass transition temperature in polymer films. A decrease in T_g tends to be observed at the polymer-air interface due to free surface for greater polymer movement. An increase in T_g tends to be at the polymer-substrate interface due to attractive interactions that limit chain mobility.[54,55]

Fluorescent moieties have been utilized to observe how soft and hard confinements would result in the shift of T_g.[56] Work by Priestley *et al.* looked into how incorporating the pyrene probe at specific locations in a polymer chain can be used to determine the T_g at

local environments.[57] All of these studies were endeavoring to determine factors that affect chain mobility at interfaces. Fundamental understanding of chain mobility will link local dynamics and bulk material properties together, and allow physical properties to be tuned for different applications.[42]

A recent study done by Seethamraju *et al.* specifically used a water-sensitive dye (rhodamine B-based) to visualize water located at the glass fiber and epoxy interface via confocal optical microscopy. The fluorescence intensity correlates with the water concentration within the epoxy matrix, **Figure 1.15**. Most of the water resides at the epoxy-glass fiber interfaces.[58] While this work indicated where water prefers to migrate within an epoxy composites, there has yet to be a study on polymer responses at the interface between polymer and filler, and how that translates to mechanical properties.

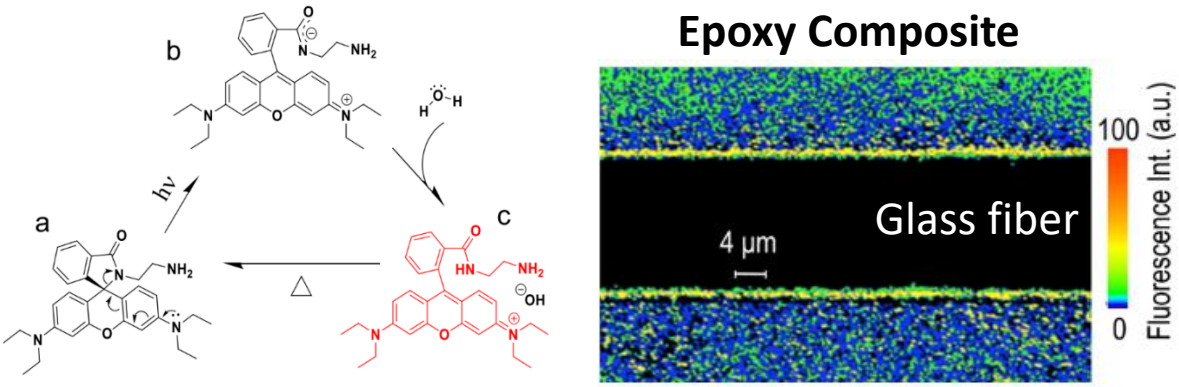

Figure 1.15. The activation mechanism of the water-sensitive dye (left) and the confocal image of epoxy labelled composite with glass fiber. Fluorescence intensity correlates to water concentration, residing at the epoxy-glass fiber interface. Images taken from Ref. 58.

1.7. Introduction to Fluorescence Lifetime Imaging Microscopy (FLIM)

Fluorescence lifetime imaging microscopy (FLIM) is a technique first introduced in 1959 that combined time resolved fluorescence spectroscopy with microscopy to determine

the spatial distribution of excited state lifetimes at the nanosecond time scale.[59] Fluorescent lifetime (τ) is the average time that an electron remains in the excited state before it decays to the ground state. The process of electrons leaving the excited state through radiative and non-radiative processes decays exponentially. During the lifetime period, a fluorophore can undergo conformation changes, diffusion, or interact with its environment. Luckily, the lifetime of most fluorophores is within the nanoseconds range, which is ideal for imaging.[60] To resolve lifetimes at this time scale, the modulation of excitation and detection need to function at very high speeds. Investigations using FLIM can provide a profile of single to multiple decay times in two and three dimensions. Due to its capabilities, FLIM has also been used in biological fields to observe biomolecules *in vivo*.[60] This technique has also been implemented in imaging ion concentration, tissue characterization, proteins, and living cells.[59,61–64]

FLIM can analyze in both the frequency-domain and time-domain. In the frequency-domain, the intensity of the excitation light is modulated and the lifetime is determined by analyzing the phase shift of the fluorescence emission. The time-domain is used for analysis where a short pulse of light excites the sample and the emitted time-resolved fluorescence is recorded to obtain decay curves of the lifetime. The decay curves can be obtained by tracking photons while another method divides the photon counts at certain time intervals using a gated detector.

For a single exponential decay, the fluorescent intensity is written as **Eq. 1** where I(t) is the fluorescent intensity as a function of time, I_0 is the initial intensity after the pulse, t is time after the pulse, and τ is the lifetime.[59] However, multicomponent exponential fitting is sometimes necessary to capture the different lifetimes, described by **Eq. 2**.

$$I(t) = I_0 e^{-(t/\tau)} \quad \textbf{Eq. 1}$$

$$I(t) = I_0 \sum_i \alpha_i e^{-(t/\tau_i)} \quad \textbf{Eq. 2}$$

The emission can decay slowly or quickly over time, seen in **Figure 1.16**. The decay profile is influenced by interactions that fluorophores undergo that would affect its quantum yield and lifetime, called fluorescence quenching. The quenching is categorized as: dynamic quenching (via interactions with a quencher and the fluorophore in the excited state), static quenching (interaction of fluorophore and quenching compound), self-quenching (due to high concentration of fluorophores), and color-quenching (the emitted photons are absorbed by a colored molecule). Advantageously, fluorescence lifetime is influenced by energy transfer and not affected by concentration, exposure duration, excitation intensity, or detection efficiency.

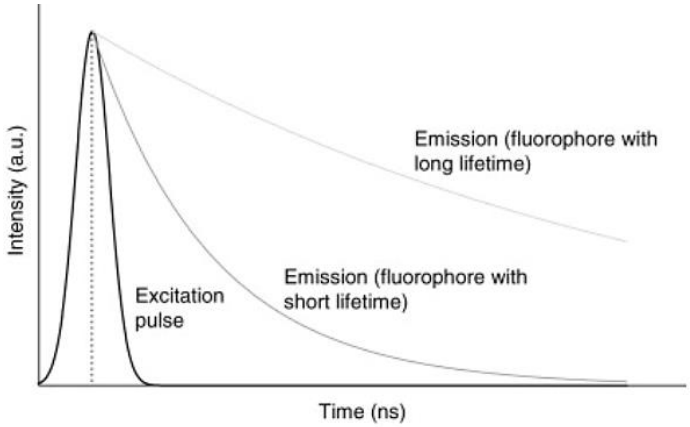

Figure 1.16. Time-domain lifetime measurement. Once the molecule is excited by excitation pulse, the decay curve is measured via the emitted fluorescence as a function of time. Figure was taken from Ref. 65.

Fluorescence lifetime is sensitive to the environment surrounding the fluorophores, such as pH, polarity, temperature, and refractive index. Due to these sensitivities, determining lifetimes via FLIM allows understanding of the dynamic changes in local environments that the fluorophores are experiencing.[60] Tanaka *et al*. studied polymer

dynamics and observed that fluorescence lifetime was dependent on molecular motion of the chains.[66] Longer lifetime means the fluorophores are in a mobility restricted region while a shorter lifetime is a result of non-radiative pathways present for fluorophores to decay quickly due to being in highly mobile environments.[41,66] This observation motivates the implementation of FLIM to extend exploration in chain dynamics for polymer composite systems and comprehend molecular motions at the microscopic scale.

Work by Okabe *et al.* demonstrated the first intracellular temperature mapping by utilizing a thermos-sensitive probe and FLIM. Using a fluorescent polymeric thermometer (FPT) that diffused throughout the COS7 cell and poly-N-*n*-propylacrylamide (NNPAM) with a LCST, they were able to show a temperature gradient between the nucleus and cytoplasm that depended on the cell cycle. With increasing temperature above the LCST, there was an increase in fluorescence intensity and a shift to longer lifetime by 2 ns. The longer lifetime occurred due to the polymer chains transition from hydrophilic coils to hydrophobic globules that resulted in a more restricted environment, as seen in **Figure 1.17**.[67] This revealed FLIM as a sensitive technique that had the capability to detect the change in polymer configurations and local environments.

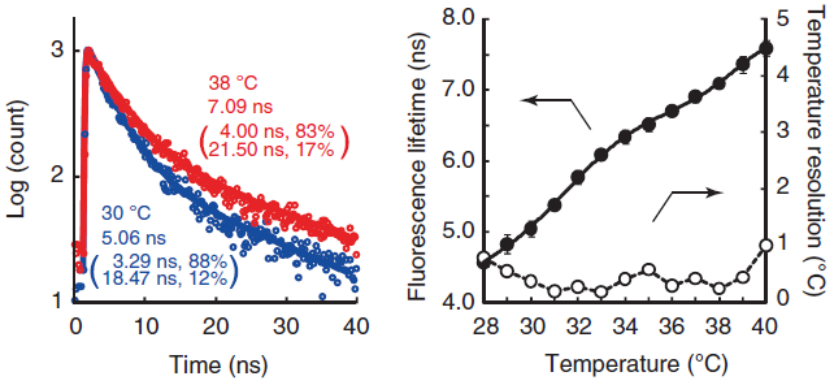

Figure 1.17. FLIM measurement of thermos-sensitive polymer system (FPT) in a COS_7 cell extract above and below the LCST. At 37 °C, fluorescence intensity increased and exhibited longer fluorescence lifetime while the inverse occurred at 30 °C. Image taken from Ref. 67.

1.8. Dissertation Objectives

Inspired by Bouligand structures that exist in biological composites, this dissertation aims to design multifunctional nanocomposites to investigate the fundamental structure-property relationships at polymer-CNCs interfaces. Previous work done by our collaborators at NIST visualized water at an epoxy-glass fiber interface via confocal imaging and utilized FLIM to understand applied force on silk fibers at the interface.[41,58] Merging these two concepts, polymer dynamics can be explored at polymer-CNCs interfaces using a water-sensitive dye to observe how water content and polymer confinement translate to macroscopic mechanical performance. Incorporating poly(diethylene glycol methyl ether methacrylate) ($PMEO_2MA$) as the soft polymer phase into CNCs matrix provided toughness and stimuli-responsiveness to the resulting nanocomposite films. In Chapter 2, investigations on how the thermoresponsive polymers self-assemble with CNCs as well as optical and mechanical properties will be explored. Using the knowledge from this initial study, Chapters 3 and 4 both focus on the local dynamics of confined polymer chains by copolymerizing Rhodamine-based water-sensitive dye into $PMEO_2MA$ polymer chains. Chapter 3 examined the physical absorption of polymer chains and examine the different dynamic environments via fluorescence lifetime measurements. In Chapter 4, a polymer dynamics comparison was made between the covalently bonded and physically adsorbed thermoresponsive polymer chains to CNCs surfaces. Finally, Chapter 5 will summarize the important findings and discuss future directions to further understand CNC nanocomposite films.

1.9. References

(1) Habibi, Y.; Lucia, L. A.; Rojas, O. J. Cellulose Nanocrystals: Chemistry, Self-Assembly, and Applications. *Chem. Rev.* **2010**, *110* (6), 3479–3500. https://doi.org/10.1021/cr900339w.

(2) Hamad, W. Y. *Cellulose Nanocrystals: Properties, Production and Applications*; 2017. https://doi.org/10.1002/9781118675601.

(3) Chen, P. Y.; Lin, A. Y. M.; McKittrick, J.; Meyers, M. A. Structure and Mechanical Properties of Crab Exoskeletons. *Acta Biomater.* **2008**, *4* (3), 587–596. https://doi.org/10.1016/j.actbio.2007.12.010.

(4) Raabe, D.; Sachs, C.; Romano, P. The Crustacean Exoskeleton as an Example of a Structurally and Mechanically Graded Biological Nanocomposite Material. *Acta Mater.* **2005**, *53* (15), 4281–4292. https://doi.org/10.1016/j.actamat.2005.05.027.

(5) Guarín-Zapata, N.; Gomez, J.; Yaraghi, N.; Kisailus, D.; Zavattieri, P. D. Shear Wave Filtering in Naturally-Occurring Bouligand Structures. *Acta Biomater.* **2015**, *23*, 11–20. https://doi.org/10.1016/j.actbio.2015.04.039.

(6) Grunenfelder, L. K.; Herrera, S.; Kisailus, D. Crustacean-Derived Biomimetic Components and Nanostructured Composites. *Small* **2014**, *10* (16), 3207–3232. https://doi.org/10.1002/smll.201400559.

(7) Natarajan, B.; Krishnamurthy, A.; Qin, X.; Emiroglu, C. D.; Forster, A.; Foster, E. J.; Weder, C.; Fox, D. M.; Keten, S.; Obrzut, J.; Gilman, J. W. Binary Cellulose Nanocrystal Blends for Bioinspired Damage Tolerant Photonic Films. *Adv. Funct. Mater.* **2018**, *28* (26), 1800032. https://doi.org/10.1002/adfm.201800032.

(8) Sacui, I. A.; Nieuwendaal, R. C.; Burnett, D. J.; Stranick, S. J.; Jorfi, M.; Weder, C.; Foster, E. J.; Olsson, R. T.; Gilman, J. W. Comparison of the Properties of Cellulose Nanocrystals and Cellulose Nanofibrils Isolated from Bacteria, Tunicate, and Wood Processed Using Acid, Enzymatic, Mechanical, and Oxidative Methods. *ACS Appl. Mater. Interfaces* **2014**, *6* (9), 6127–6138. https://doi.org/10.1021/am500359f.

(9) Wang, B.; Walther, A. Self-Assembled, Iridescent, Crustacean-Mimetic Nanocomposites with Tailored Periodicity and Layered Cuticular Structure. *ACS Nano* **2015**, *9* (11), 10637–10646. https://doi.org/10.1021/acsnano.5b05074.

(10) Mitov, M. Cholesteric Liquid Crystals in Living Matter. *Soft Matter* **2017**, *13* (23), 4176–4209. https://doi.org/10.1039/c7sm00384f.

(11) Natarajan, B.; Emiroglu, C.; Obrzut, J.; Fox, D. M.; Pazmino, B.; Douglas, J. F.; Gilman, J. W. Dielectric Characterization of Confined Water in Chiral Cellulose Nanocrystal Films. *ACS Appl. Mater. Interfaces* **2017**, *9* (16), 14222–14231. https://doi.org/10.1021/acsami.7b01674.

(12) Velasco-Hogan, A.; Xu, J.; Meyers, M. A. Additive Manufacturing as a Method to Design and Optimize Bioinspired Structures. *Adv. Mater.* **2018**, *30* (52), 1800940. https://doi.org/10.1002/adma.201800940.

(13) Vargas, W.; Avendano, E.; Hernández-Jiménez, M.; Azofeifa, D.; Libby, E.; Solís, Á.; Barboza-Aguilar, C. Photonic Crystal Characterization of the Cuticles of Chrysina Chrysargyrea and Chrysina Optima Jewel Scarab Beetles. *Biomimetics* **2018**, *3* (4), 30. https://doi.org/10.3390/biomimetics3040030.

(14) Natarajan, B.; Gilman, J. W. Bioinspired Bouligand Cellulose Nanocrystal Composites: A Review of Mechanical Properties. *Philos. Trans. A. Math. Phys. Eng. Sci.* **2018**, *376* (2112), 20170050. https://doi.org/10.1098/rsta.2017.0050.

(15) Zhu, B.; Merindol, R.; Benitez, A. J.; Wang, B.; Walther, A. Supramolecular Engineering of Hierarchically Self-Assembled, Bioinspired, Cholesteric Nanocomposites Formed by Cellulose Nanocrystals and Polymers. *ACS Appl. Mater. Interfaces* **2016**, *8*, 11031–11040. https://doi.org/10.1021/acsami.6b00410.

(16) Thielemans, W.; Wohlhauser, S.; Delepierre, G.; Labet, M.; Weder, C.; Zoppe, J. O. Grafting Polymers from Cellulose Nanocrystals : Synthesis , Properties , and Applications. *Macromolecules* **2018**, *51*, 6157–6189. https://doi.org/10.1021/acs.macromol.8b00733.

(17) Wan, H.; Li, X.; Zhang, L.; Li, X.; Liu, P.; Jiang, Z.; Yu, Z. Z. Rapidly Responsive and Flexible Chiral Nematic Cellulose Nanocrystal Composites as Multifunctional Rewritable Photonic Papers with Eco-Friendly Inks. *ACS Appl. Mater. Interfaces* **2018**, *10* (6), 5918–5925. https://doi.org/10.1021/acsami.7b19375.

(18) Yao, K.; Meng, Q.; Bulone, V.; Zhou, Q. Flexible and Responsive Chiral Nematic Cellulose Nanocrystal/Poly(Ethylene Glycol) Composite Films with Uniform and Tunable Structural Color. *Adv. Mater.* **2017**, *29* (28), 1–8. https://doi.org/10.1002/adma.201701323.

(19) Guidetti, G.; Atifi, S.; Vignolini, S.; Hamad, W. Y. Flexible Photonic Cellulose Nanocrystal Films. *Adv. Mater.* **2016**, *28* (45), 10042–10047. https://doi.org/10.1002/adma.201603386.

(20) Kose, O.; Tran, A.; Lewis, L.; Hamad, W. Y.; Maclachlan, M. J. Unwinding a Spiral of Cellulose Nanocrystals for Stimuli-Responsive Stretchable Optics. *Nat. Commun.* **2019**, *10* (510). https://doi.org/10.1038/s41467-019-08351-6.

(21) Geng, S.; Yao, K.; Zhou, Q.; Oksman, K. High-Strength, High-Toughness Aligned Polymer-Based Nanocomposite Reinforced with Ultralow Weight Fraction of Functionalized Nanocellulose. *Biomacromolecules* **2018**, *19* (10), 4075–4083. https://doi.org/10.1021/acs.biomac.8b01086.

(22) Habibi, Y.; Goffin, A. L.; Schiltz, N.; Duquesne, E.; Dubois, P.; Dufresne, A. Bionanocomposites Based on Poly(ε-Caprolactone)-Grafted Cellulose Nanocrystals by Ring-Opening Polymerization. *J. Mater. Chem.* **2008**, *18* (41), 5002–5010. https://doi.org/10.1039/b809212e.

(23) Risteen, B.; Delepierre, G.; Srinivasarao, M.; Weder, C.; Russo, P.; Reichmanis, E.; Zoppe, J. Thermally Switchable Liquid Crystals Based on Cellulose Nanocrystals with Patchy Polymer Grafts. *Small* **2018**, *14* (46), 1–10. https://doi.org/10.1002/smll.201802060.

(24) Zoppe, J. O.; Dupire, A. V. M.; Lachat, T. G. G.; Lemal, P.; Rodriguez-Lorenzo, L.; Petri-Fink, A.; Weder, C.; Klok, H. A. Cellulose Nanocrystals with Tethered Polymer Chains: Chemically Patchy versus Uniform Decoration. *ACS Macro Lett.* **2017**, *6* (9), 892–897. https://doi.org/10.1021/acsmacrolett.7b00383.

(25) Zoppe, J. O.; Österberg, M.; Venditti, R. A.; Laine, J.; Rojas, O. J. Surface Interaction Forces of Cellulose Nanocrystals Grafted with Thermoresponsive Polymer Brushes. *Biomacromolecules* **2011**, *12* (7), 2788–2796. https://doi.org/10.1021/bm200551p.

(26) Porsch, C.; Hansson, S.; Nordgren, N.; Malmström, E. Thermo-Responsive Cellulose-Based Architectures: Tailoring LCST Using Poly(Ethylene Glycol) Methacrylates. *Polym. Chem.* **2011**, *2* (5), 1114–1123. https://doi.org/10.1039/c0py00417k.

(27) Zoppe, J. O.; Habibi, Y.; Rojas, O. J.; Venditti, R. A.; Johansson, L. S.; Efimenko, K.; Österberg, M.; Laine, J. Poly(N -Isopropylacrylamide) Brushes Grafted from Cellulose Nanocrystals via Surface-Initiated Single-Electron Transfer Living Radical Polymerization. *Biomacromolecules* **2010**, *11* (10), 2683–2691. https://doi.org/10.1021/bm100719d.

(28) Azzam, F.; Siqueira, E.; Fort, S.; Hassaini, R.; Pignon, F.; Travelet, C.; Putaux, J. L.; Jean, B. Tunable Aggregation and Gelation of Thermoresponsive Suspensions of Polymer-Grafted Cellulose Nanocrystals. *Biomacromolecules* **2016**, *17* (6), 2112–2119. https://doi.org/10.1021/acs.biomac.6b00344.

(29) Grishkewich, N.; Akhlaghi, S. P.; Zhaoling, Y.; Berry, R.; Tam, K. C. Cellulose Nanocrystal-Poly(Oligo(Ethylene Glycol) Methacrylate) Brushes with Tunable LCSTs. *Carbohydr. Polym.* **2016**, *144*, 215–222. https://doi.org/10.1016/j.carbpol.2016.02.044.

(30) Viet, D.; Beck-Candanedo, S.; Gray, D. G. Dispersion of Cellulose Nanocrystals in Polar Organic Solvents. *Cellulose* **2007**, *14* (2), 109–113. https://doi.org/10.1007/s10570-006-9093-9.

(31) Klemm, D.; Kramer, F.; Moritz, S.; Lindström, T.; Ankerfors, M.; Gray, D.; Dorris, A. Nanocelluloses: A New Family of Nature-Based Materials. *Angew. Chemie - Int. Ed.* **2011**, *50* (24), 5438–5466. https://doi.org/10.1002/anie.201001273.

(32) Dagnon, K. L.; Shanmuganathan, K.; Weder, C.; Rowan, S. J. Water-Triggered Modulus Changes of Cellulose Nanofiber Nanocomposites with Hydrophobic Polymer Matrices. *Macromolecules* **2012**, *45* (11), 4707–4715. https://doi.org/10.1021/ma300463y.

(33) Sinko, R.; Keten, S. Effect of Moisture on the Traction-Separation Behavior of Cellulose Nanocrystal Interfaces. *Appl. Phys. Lett.* **2014**, *105* (24), 243702. https://doi.org/10.1063/1.4904708.

(34) Weber, C.; Hoogenboom, R.; Schubert, U. S. Temperature Responsive Bio-Compatible Polymers Based on Poly(Ethylene Oxide) and Poly(2-Oxazoline)S. *Prog. Polym. Sci.* **2012**, *37* (5), 686–714. https://doi.org/10.1016/j.progpolymsci.2011.10.002.

(35) Lutz, Jean-Francois, Weichenhan, Katja, Akdemir, Ozgur, Hoth, A. About the Phase Transitions in Aqueous Solutions of Thermoresponsive Copolymers and Hydrogels Based on 2- (2-Methoxyethoxy) Ethyl Methacrylate and Oligo (Ethylene Glycol) Methacrylate. *Macromolecules* **2007**, *40* (7), 2503–2508. https://doi.org/10.1021/ma062925q.

(36) Lutz, Jean-Francois and Hoth, A. Preparation of Ideal PEG Analogues with a Tunable Thermosensitivity by Controlled Radical Copolymerization of 2-(2-Methoxyethoxy)Ethyl Methacrylate and Oligo(Ethylene Glycol) Methacrylate. *Macromolecules* **2006**, *39* (2), 893–896. https://doi.org/10.1021/ma0517042.

(37) Lutz, J. Thermo-Switchable Materials Prepared Using The. *Adv. Mater.* **2011**, *23* (19), 2237–2243. https://doi.org/10.1002/adma.201100597.

(38) Matsumoto, K.; Sakikawa, N.; Miyata, T. Thermo-Responsive Gels That Absorb Moisture and Ooze Water. *Nat. Commun.* **2018**, *9* (1), 1–7. https://doi.org/10.1038/s41467-018-04810-8.

(39) Zhang, B.; Cheng, Y.; Wang, H.; Ye, B.; Shang, L.; Zhao, Y.; Gu, Z. Multifunctional Inverse Opal Particles for Drug Delivery and Monitoring. *Nanoscale* **2015**, *7*, 10590–10594. https://doi.org/10.1039/c5nr02324f.

(40) Sharpe, L. H. The Interphase in Adhesion†. *J. Adhes.* **1972**, *4* (1), 51–64. https://doi.org/10.1080/00218467208072210.

(41) Woodcock, J. W.; Beams, R.; Davis, C. S.; Chen, N.; Stranick, S. J.; Shah, D. U.; Vollrath, F.; Gilman, J. W. Observation of Interfacial Damage in a Silk-Epoxy Composite, Using a Simple Mechanoresponsive Fluorescent Probe. *Adv. Mater. Interfaces* **2017**, *4* (10), 1–5. https://doi.org/10.1002/admi.201601018.

(42) Lin, C. C.; Parrish, E.; Composto, R. J. Macromolecule and Particle Dynamics in Confined Media. *Macromolecules* **2016**, *49* (16), 5755–5772. https://doi.org/10.1021/acs.macromol.6b00471.

(43) Bailey, E. J.; Winey, K. I. Dynamics of Polymer Segments , Polymer Chains , and Nanoparticles in Polymer Nanocomposite Melts : A Review. *Prog. Polym. Sci.* **2020**, *105*, 101242. https://doi.org/10.1016/j.progpolymsci.2020.101242.

(44) Priestley, R. D.; Cangialosi, D.; Napolitano, S. On the Equivalence between the Thermodynamic and Dynamic Measurements of the Glass Transition in Con Fi Ned Polymers. *J. Non. Cryst. Solids* **2015**, *407*, 288–295. https://doi.org/10.1016/j.jnoncrysol.2014.09.048.

(45) Rubinstein, M.; Colby, R. *Polymer Physics*; Oxford University Press: New York, 2003.

(46) Robertson, C. G.; Roland, C. M. Glass Transition and Interfacial Segmental Dynamics in Polymer-Particle Composites. *Rubber Chem. Technol.* **2008**, *81* (3), 506–522.

(47) Kremer, F.; Schonhals, A. *Broadband Dielectric Spectroscopy*; Springer-Verlag: Berlin, 2002.

(48) Carroll, B.; Cheng, S.; Sokolov, A. P. Analyzing the Interfacial Layer Properties in Polymer Nanocomposites by Broadband Dielectric Spectroscopy. *Macromolecules* **2017**, *50* (16), 6149–6163. https://doi.org/10.1021/acs.macromol.7b00825.

(49) Richter, D.; Monkenbusch, S. D. Neutron Scattering. In *Polymer science: a comprehensive reference*; Matyjaszewski, K., Moller, M., Eds.; Elsevier BV: Amsterdam, 2012; pp 331–360.

(50) Bailey, E. J.; Gri, P. J.; Tyagi, M.; Winey, K. I. Quasi-Elastic Neutron Scattering Study. *Macromolecules* **2019**, *52* (2), 669–678. https://doi.org/10.1021/acs.macromol.8b01716.

(51) Lenhart, J. L.; Van Zanten, J. H.; Dunkers, J. P.; Parnas, R. S. Studying the Buried Interfacial Region with an Immobilized Fluorescence Probe. *Macromolecules* **2001**, *34* (7), 2225–2231. https://doi.org/10.1021/ma0015572.

(52) Davis, D. A.; Hamilton, A.; Yang, J.; Cremar, L. D.; Van Gough, D.; Potisek, S. L.; Ong, M. T.; Braun, P. V.; Martínez, T. J.; White, S. R.; Moore, J. S.; Sottos, N. R. Force-Induced Activation of Covalent Bonds in Mechanoresponsive Polymeric Materials. *Nature* **2009**, *459* (7243), 68–72. https://doi.org/10.1038/nature07970.

(53) Tito, N. B.; Lipson, E. G.; Milner, S. T. Soft Matter Lattice Model of Mobility at Interfaces : Free Surfaces ,. *Soft Matter* **2013**, *9*, 9403–9413. https://doi.org/10.1039/c3sm51287h.

(54) Rittigstein, P.; Torkelson, J. M. Polymer – Nanoparticle Interfacial Interactions in Polymer Nanocomposites : Confinement Effects on Glass Transition Temperature and Suppression of Physical Aging. *J. Polym. Sci. Part B Polym. Phys.* **2006**, *44* (20), 2935–2943. https://doi.org/10.1002/polb.

(55) Kim, S.; Hewlett, S. A.; Roth, C. B.; Torkelson, J. M. Confinement Effects on Glass Transition Temperature , Transition Breadth , and Expansivity : Comparison of Ellipsometry And. *Eur. Phys. J. E* **2009**, *92* (30), 83–92. https://doi.org/10.1140/epje/i2009-10510-y.

(56) Christie, D.; Register, R. A.; Priestley, R. D. Role of Chain Connectivity across an Interface on the Dynamics of a Nanostructured Block Copolymer. *Phys. Rev. Lett.* **2018**, *121* (24), 247801. https://doi.org/10.1103/PhysRevLett.121.247801.

(57) Christie, D.; Register, R. A.; Priestley, R. D. Direct Measurement of the Local Glass Transition in Self-Assembled Copolymers with Nanometer Resolution. *ACS Cent. Sci.* **2018**, *4*, 504–511. https://doi.org/10.1021/acscentsci.8b00043.

(58) Seethamraju, S.; Obrzut, J.; Douglas, J. F.; Woodcock, J. W.; Gilman, J. W. Quantifying Fluorogenic Dye Hydration in an Epoxy Resin by Noncontact Microwave Dielectric Spectroscopy. *J. Phys. Chem. B* **2020**, *124* (14), 2914–2919. https://doi.org/10.1021/acs.jpcb.9b11622.

(59) Munster, E. B. Van; Gadella, T. W. J. Fluorescence Lifetime Imaging Microscopy (FLIM) Alternating Current. In *Microscopy Techniques*; 2005; Vol. 95, pp 143–175. https://doi.org/10.1007/b102213.

(60) Ishikawa-ankerhold, H. C.; Ankerhold, R.; Drummen, G. P. C.; Biology, C.; Zeiss, C.; Gmbh, M.; Program, B.; Stress, C.; Program, A. Advanced Fluorescence Microscopy Techniques—FRAP , FLIP , FLAP , FRET and FLIM. *Molecules* **2012**, *17* (4), 4047–4132. https://doi.org/10.3390/molecules17044047.

(61) Blacker, T. S.; Mann, Z. F.; Gale, J. E.; Ziegler, M.; Bain, A. J.; Szabadkai, G.; Duchen, M. R. Separating NADH and NADPH Fluorescence in Live Cells and Tissues Using FLIM. *Nat. Commun.* **2014**, *5* (3936). https://doi.org/10.1038/ncomms4936.

(62) Provenzano, P. P.; Eliceiri, K. W.; Keely, P. J. Multiphoton Microscopy and Fluorescence Lifetime Imaging Microscopy (FLIM) to Monitor Metastasis and the Tumor Microenvironment. *Clin Exp Metastasis* **2009**, *26*, 357–370. https://doi.org/10.1007/s10585-008-9204-0.

(63) Wallrabe, H.; Periasamy, A. Imaging Protein Molecules Using FRET and FLIM Microscopy. *Curr. Opin. Biotechnol.* **2005**, *16* (1), 19–27. https://doi.org/10.1016/j.copbio.2004.12.002.

(64) Padilla-Parra, S.; Tramier, M. FRET Microscopy in the Living Cell: Different Approaches, Strengths and Weaknesses. *BioEssays* **2012**, *34* (5), 369–376. https://doi.org/10.1002/bies.201100086.

(65) Jain, A.; Blum, C.; Subramaniam, V. Chapter 4 - Fluorescence Lifetime Spectroscopy and Imaging of Visible Fluorescent Proteins. In *Advances in Biomedical Engineering*; 2009; pp 147–176.

(66) Shundo, A.; Okada, Y.; Ito, F.; Tanaka, K. Fluorescence Behavior of Dyes in Thin Films of Various Polymers. *Macromolecules* **2012**, *45* (1), 329–335. https://doi.org/10.1021/ma201901x.

(67) Okabe, K.; Inada, N.; Gota, C.; Harada, Y.; Funatsu, T.; Uchiyama, S. Intracellular Temperature Mapping with a Fluorescent Polymeric Thermometer and Fluorescence Lifetime Imaging Microscopy. *Nat. Commun.* **2012**, *3* (705), 1–9. https://doi.org/10.1038/ncomms1714.

CHAPTER 2. BOULIGAND NANOCOMPOSITES: SELF-ASSEMBLY OF CELLULOSE NANOCRYSTALS WITH THERMORESPONSIVE POLYMERS

2.1. Abstract

This work focuses on designing multifunctional cellulose nanocrystal nanocomposites with high toughness and stimuli-responsiveness. To overcome CNCs brittle nature, a thermoresponsive polymer ($PMEO_2MA$) was incorporated into CNC matrices as the soft phase to dissipate impact energy. Nanocomposite films of $PMEO_2MA$-CNC with 0 to 30 mass % of $PMEO_2MA$ loadings were prepared via controlled evaporation-induced self-assembly. As the polymer infiltrates CNCs' helical structure, the resulting films' reflectance wavelength transitions from blue to red. $PMEO_2MA$-CNC nanocomposites exhibited reversible humidity and temperature responses in the solid-state, demonstrating the tunability of the self-assembled films. Dynamic mechanical analysis revealed polymer incorporation improved flexibility and toughness of CNC matrices.

2.2. Experimental

2.2.1. Materials

The 12.1 mass % of sodium-neutralized sulfated wood cellulose nanocrystals (Na-CNCs) in aqueous suspensions were obtained from the University of Maine Process Development Center. Di(ethylene glycol) methyl ether methacrylate (MEO_2MA, 95 %), copper (I) bromide (CuBr, 99.999 %), and ethyl α-bromoisobutyrate (EBriB, 98 %) were purchased from Sigma-Aldrich. Hexanes (95 %) was purchased from Fisher Scientific. Toluene, anhydrous (99.8 %), Copper (II) bromide ($CuBr_2$, 99 %) and 2,2'-bipyridine (bpy, 99+ %) were purchased from Alfa Aesar. The chemicals were used as received.

2.2.2. Synthesis of PMEO$_2$MA

Diethylene glycol methyl ether methacrylate (MEO$_2$MA) was passed through a basic alumina column to remove inhibitors before polymerization. In a 20 mL reaction vial, 3 mL of MEO$_2$MA, 3 mL of anhydrous toluene, 2,2'-bipyridine (Bpy 0.039 g, 0.25 mmol), $CuBr_2$ (0.0024g, 0.011 mmol), and CuBr (0.016 g, 0.11 mmol) were added and the vial was purged with nitrogen for 25 minutes. The initiator ethyl α-bromoisobutyrate (EBriB 0.016 ml, 0.11 mmol) was then added and the reaction performed for 7 hours at 70 °C. The reaction solution was passed through basic alumina column to remove the copper species before precipitating the polymer in hexanes. The PMEO$_2$MA polymer has M_n of 15.7 kDa with Đ = 1.29 based on DMF-GPC, shown in **Figure 2.1**

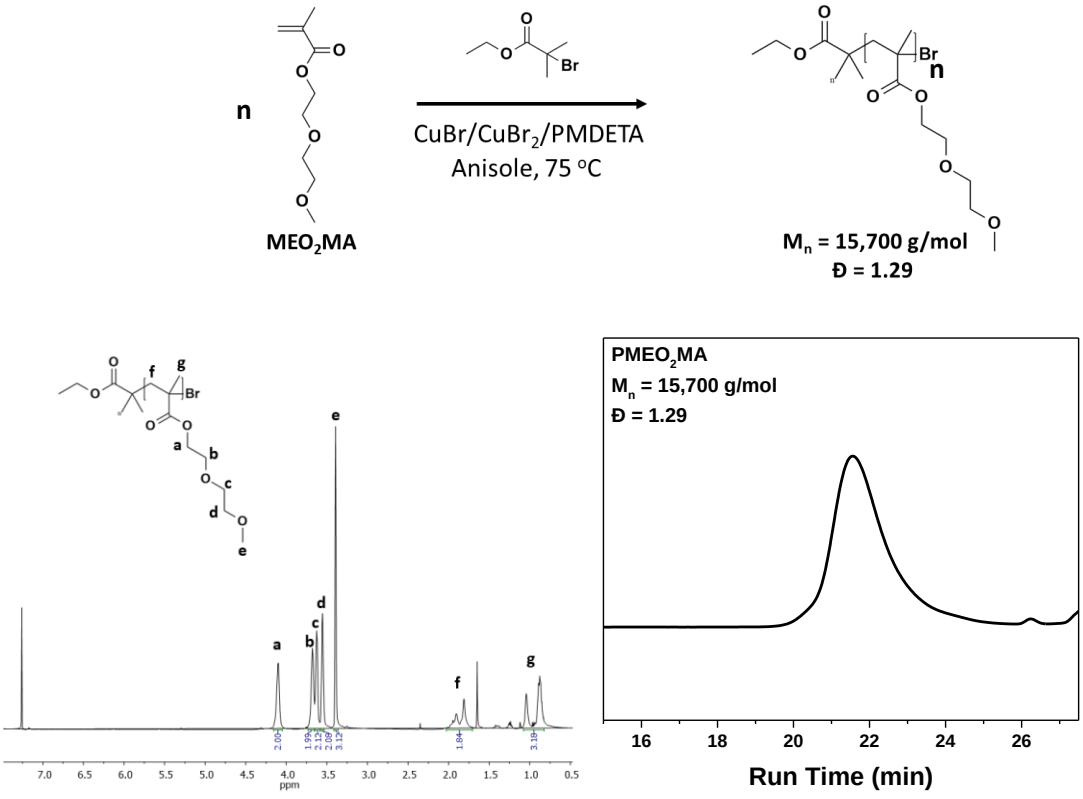

Figure 2.1. Schematic of the polymerization conditions of PMEO$_2$MA (top). ^{1}H NMR spectrum of PMEO$_2$MA homopolymer in chloroform-d and DMF-GPC spectrum.

2.2.3. Film Casting Procedure

The 12.1 mass % Na-CNCs was diluted to 2 mass % with deionized (DI) water and sonicated for 1 hour. The $PMEO_2MA$ was dispersed at 2 mass % in water and vortexed, followed by sonication for 1 hour in an ice-filled bath. The CNC dispersion and $PMEO_2MA$ solution were mixed together at respective quantities to yield films of various $PMEO_2MA$ mass fractions. Each prepared $PMEO_2MA$-CNC mixture [(0, 5, 10, 15, 20, 30) mass % of $PMEO_2MA$] was sonicated for one hour in an ice-filled bath before being poured into a polystyrene petri-dish (diameter = 50 mm). To control the drying rate of the solutions to -7 mg min^{-1}, the petri-dish was placed on a balance inside a custom-built Plexiglass chamber with a controlled flow of humid air flow (**Figure 2.2**). The casting ended once the films' mass remained constant (typically within 48 hours).

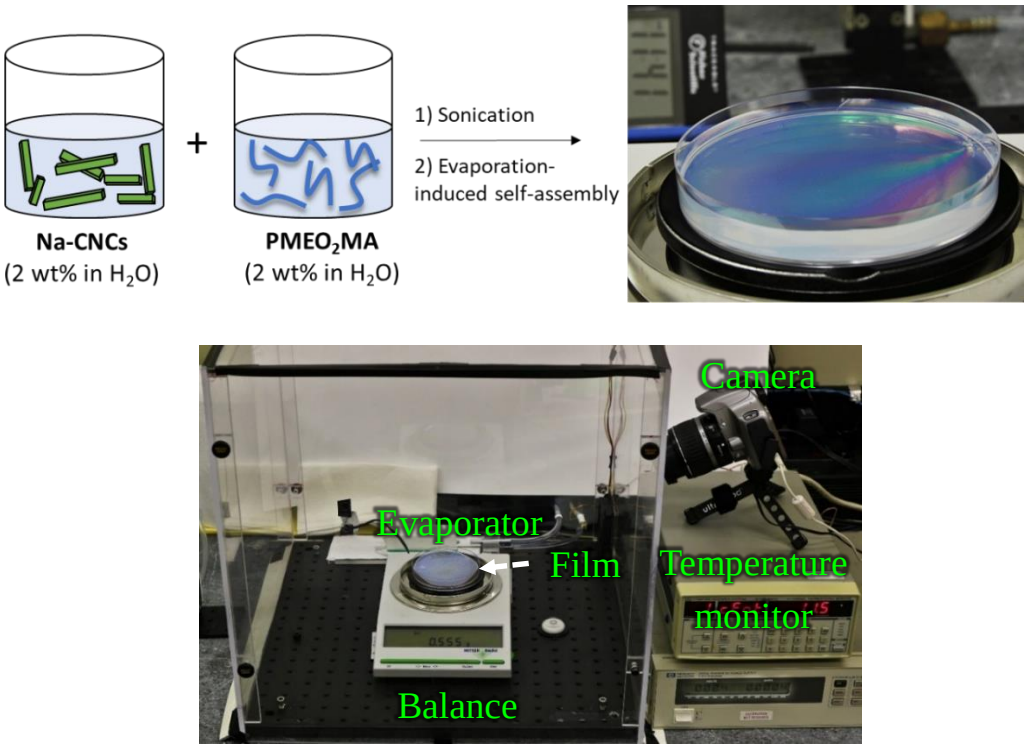

Figure 2.2. Schematic of the casting procedure of $PMEO_2MA$-CNC films. The combined solution was sonicated in an ice bath and formed a film via evaporation-induced self-assembly in a controlled humidity chamber.

2.2.4. Instrumentation and Characterization

Polarized optical microscopy (POM) images were obtained using a 5× objective, a cross polarization setting in reflection mode, and with a black backing surface. Perkin Elmer Lambda 950 spectrophotometer with a 150 mm integrating sphere kit measured the reflectance of the films from 200 nm to 2000 nm (10 nm slit widths) in 1 nm steps. Shimadzu UV-2600 UV-Vis Spectrophotometer equipped with temperature controlled was used to record reflectance and transmittance wavelengths from 400 nm to 900 nm in intervals of 1 nm step. Dimension 3100 SPM AFM analyzed the surface topography and phase modes with 4 μm scan size and scan rate of 1 Hz (512 samples/line). ^{1}H NMR was performed using a Bruker Advance III HD 500 MHz spectrometer at 25 °C. Gel permeation chromatography (GPC) was performed in DMF with RI detector. Infrared spectroscopy was performed on a Perkin-Elmer Spectrum One FT-IR spectrometer with ATR sampling accessory recorded between 650 cm^{-1} and 4000 cm^{-1} with 8 scans. Thermogravimetric analysis (TGA) Q500 was used with a heating rate of 10 K min^{-1} from 21 °C to 150 °C then an isothermal hold for 30 minutes under a nitrogen environment. The FEI Magellan 400 XHR-SEM was used to image the cross-sections of the gold coated (1 nm to 2 nm layer) fractured films at 5 kV and 13 pA. For mechanical properties, the films (cut into 30 mm × 4 mm dimensions) were measured by a RSA G2 Dynamic Mechanical Analyzer, equipped with a 35 N load cell, in constant strain-rate mode. The gauge length and strain rate used were 15 mm to 18 mm and 0.09 mm min^{-1}, respectively.

2.3. Results and Discussion

2.3.1. Optical and Structural Characterization

Cellulose nanocrystal sources can come from wood, bacteria, and tunicate with varying crystallinity and rods' dimensions.[1–3] For this study, sulfated wood CNCs with sodium cations (Na-CNCs) were used with 3 nm − 5 nm width and 100 nm − 200 nm length.[3] The thermoresponsive polymer, poly(diethylene glycol methyl ether methacrylate) ($PMEO_2MA$), with a LCST value of 26 °C, was chosen for its amphiphilic nature and accessible LCST close to ambient temperature.[4,5] $PMEO_2MA$ was synthesized via ATRP to obtain low dispersity polymers with a defined cloud point transition. The CNCs and polymer components were kept in separate aqueous solutions at 2 mass % and sonicated for one hour. The two suspensions were added and sonicated at varying quantities to yield 0 % to 30 % mass fraction of $PMEO_2MA$ in CNC matrices. The films were prepared by evaporation-induced self-assembling (EISA) inside a controlled humidity chamber at 20 °C at a constant drying rate. Previous efforts have shown CNCs structural property is affected by the rate of evaporation, hence -7 mg min^{-1} rate was chosen to yield homogenous films.[6,7]

In aqueous suspensions, CNCs are isotropic rod-like nanoparticles. Water evaporation during EISA causes the CNC rods to self-assemble into cholesteric structures with periodicities within the visible light spectrum.[8] The structural coloration of $PMEO_2MA$-CNC iridescent films was captured via polarized optical microscopy (POM) in reflection mode, shown in **Figure 2.3**. The $PMEO_2MA$-CNC films reflected colors transitioned from blue to red as the mass fraction of $PMEO_2MA$ increased. The shift in colors had been observed in literature for other water-soluble polymers-CNCs blended

systems due to the polymer chains inserting between CNC layers.[9–11] UV-vis spectroscopy quantified the reflectance wavelength of 0 % to 30 % $PMEO_2MA$-CNC films, **Figure 2.4**, and revealed a red-shift of peak reflectance from 530 nm ± 50 nm to 770 nm ± 90 nm, respectively. The shift to longer wavelength was due to polymer infiltrating and expanding CNCs pitch, in agreement with POM images. The reflectance wavelength broadness is due to variation of pitch within the films, which has been observed in biological systems.[12]

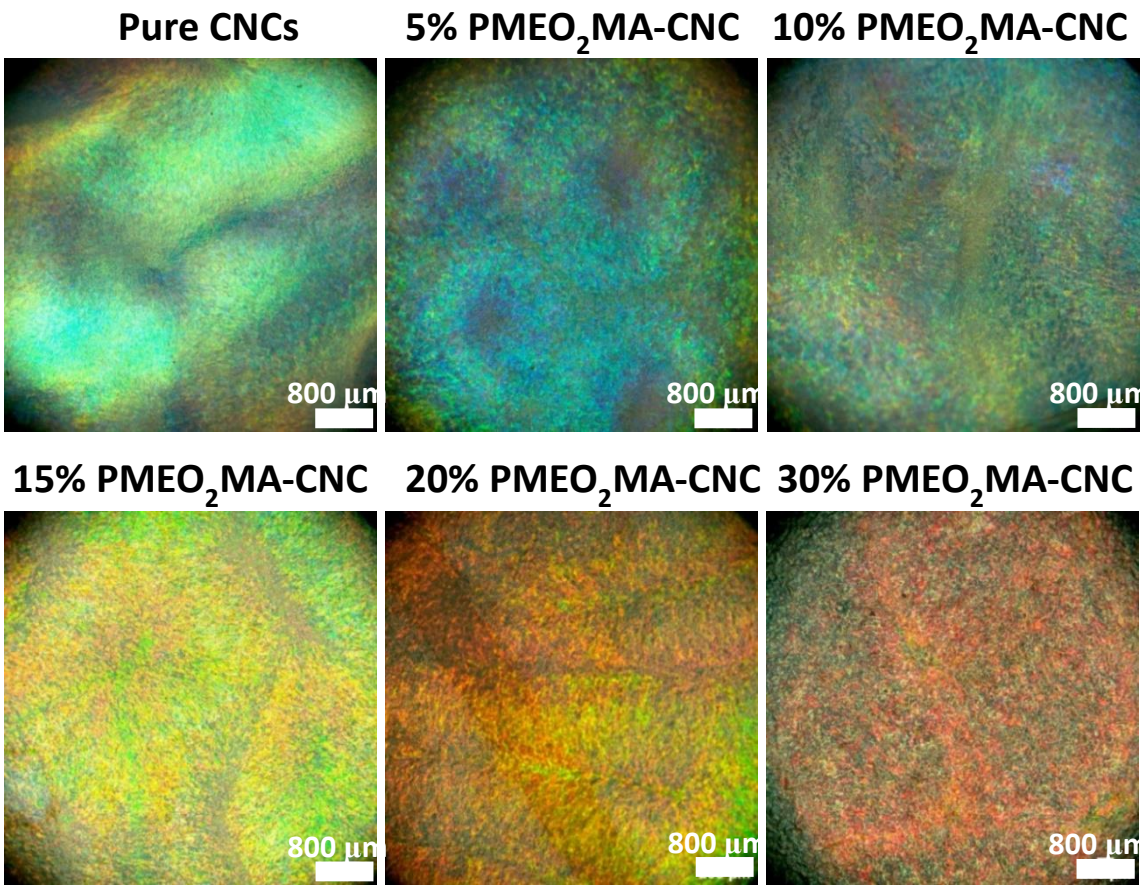

Figure 2.3. POM images of nanocomposite films of $PMEO_2MA$-CNC with [(0, 5, 10, 15, 20, 30) mass % of $PMEO_2MA$] were prepared via controlled evaporation-induced self-assembly at 20 °C. Scale bar in all images is 800 µm.

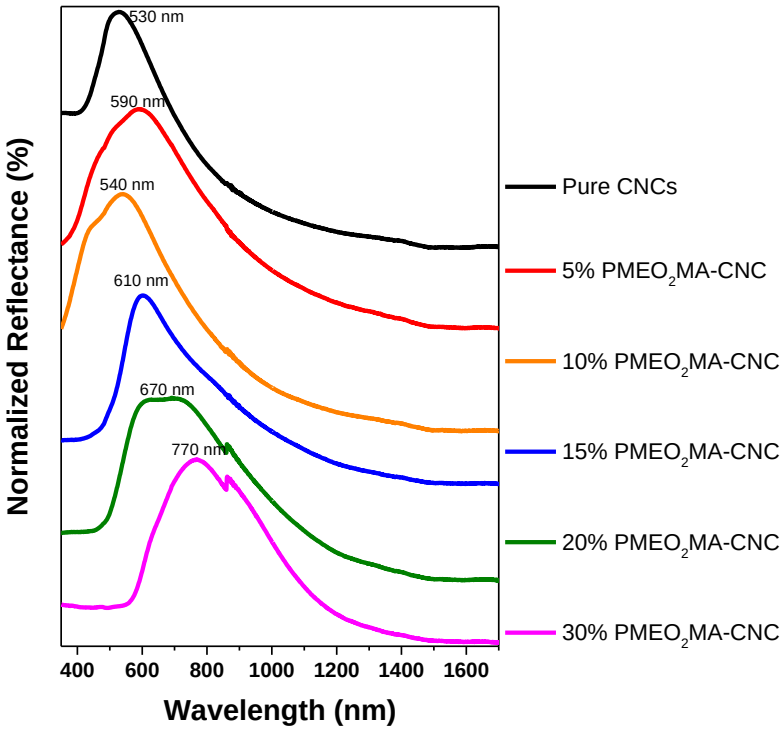

Figure 2.4. Reflectance measurements of nanocomposite films of $PMEO_2MA$-CNC with [(0, 5, 10, 15, 20, 30) mass % of $PMEO_2MA$].

Literature has reported a relative correlation between reflectance wavelength and CNCs pitch distance measured via SEM for water-soluble polymer-CNC blended systems.[9–11] To connect optical and structural properties, cross-sectional SEM images of $PMEO_2MA$-CNC fractured films were captured to obtain the pitch distances listed in **Figure 2.5** and **Table 2.1**. The films all exhibited planar cholesteric CNC layers and were uniform with pitch variation dependent on the location of the cross-sections, **Figure 2.6**. The cross-sections revealed good integration of polymer and CNC components, suggesting their compatibility through physical adsorption. The SEM measurements showed an increasing polymer loading led to an increase in pitch. For the 30 % $PMEO_2MA$-CNC, there were polymer rich regions that demonstrated inhomogeneity at high polymer loading due to polymer saturation. Water-soluble polymer-CNCs systems tend to reach polymer saturation at 40

mass % and we observe phase separation above this concentration.[9–11] Phase separation could be due to kinetics that causes the loss of ordering.[10] For the 30 % $PMEO_2MA$-CNC, there were regions were the helical structures were homogeneous while some regions were more polymer rich, shown in **Figure 2.5**. This demonstrated that for this high concentration of polymer, the composite was not homogeneous and the polymer was not well incorporated. The regions outside and within the polymer rich area varied in pitch, with an average pitch of 0.63 μm ± 0.04 μm and 0.72 μm ± 0.10 μm, respectively.

Table 2.1. Summary of $PMEO_2MA$-CNC films thickness, pitch, and reflectance

Sample	Thickness (μm)	Pitch average (μm)	Reflectance (nm)
Pure CNCs	117 ± 2.6	0.41 ± 0.07	530 ± 49
5% $PMEO_2MA$-CNC	128 ± 1.2	0.47 ± 0.07	590 ± 77
10% $PMEO_2MA$-CNC	98.2 ± 1.3	0.28 ± 0.04	540 ± 77
15% $PMEO_2MA$-CNC	90.2 ± 3.4	0.38 ± 0.06	610 ± 53
20% $PMEO_2MA$-CNC	131 ± 1.9	0.50 ± 0.1	670 ± 100
30% $PMEO_2MA$-CNC	118 ± 21	0.51 ± 0.1	770 ± 90

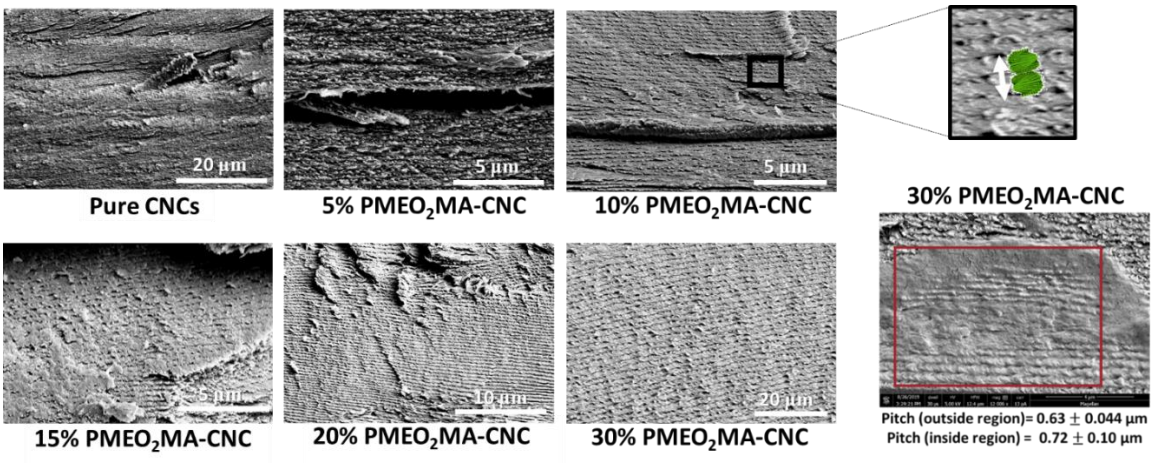

Figure 2.5. Cross-sectional SEM images for [(0, 5, 10, 15, 20, 30) mass % of $PMEO_2MA$]. There are regions in 30 % $PMEO_2MA$-CNC film with polymer rich (bottom right image) that shows a variation in pitch value.

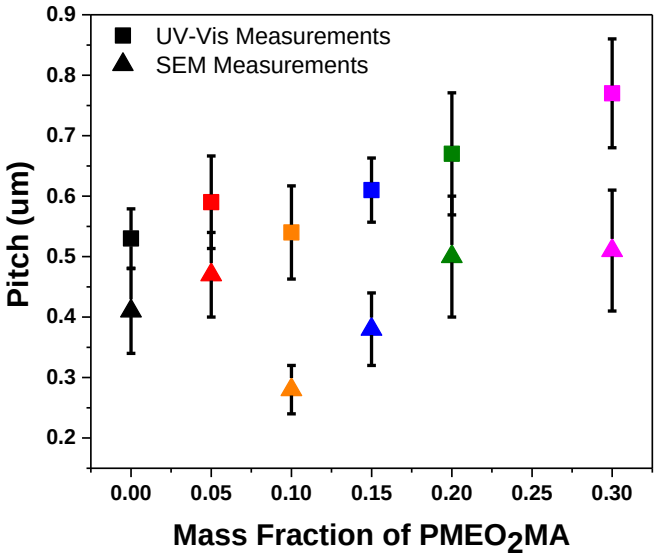

Figure 2.6. Comparison of pitch based on UV-Vis and SEM measurements for $PMEO_2MA$-CNC films.

2.3.2. Humidity and Thermal Responses

We examined CNC nanocomposite responses to 50 % and 95 % relative humidity (RH) by measuring change in reflectance wavelengths. To create a 95 % RH environment, the films were tape to one side of a closed polystyrene cuvette with saturated potassium sulfate (K_2SO_4) solution at the bottom of the cuvette for 3 days. The $PMEO_2MA$-CNC films responded to higher humidity by a shift to longer wavelength with reflectance differences ranging from 140 nm to 200 nm, shown in **Figure 2.7**. This reversible expansion of pitch was observed for other blended CNC systems with glycerol or polyethylene oxide (PEO) when they were exposed to various humidity conditions.[11,13] There was no significant correlation between the shift in reflectance and polymer loadings, which implied water adsorption was dependent on CNCs component. The observation was in contrast from work by Yao *et al.* where CNCs were blended with PEO and experienced reversible response when exposed to 50 % RH to 100 % RH. The difference in reflectance shift and water absorption increased with higher PEO loading in comparison to the pure CNCs film. For

the 20 mass % PEO-CNC film, polyethylene oxide's hydroscopic nature contributed to the water absorption going from 3 mass % to 30 mass % water, shifting the transmittance peak from 500 nm to 750 nm when exposed to 50 % RH to 95% RH environments.[11]

Despite being hydrophilic in nature, $PMEO_2MA$ does not absorb a lot of water in comparison to CNCs when ambient temperature was close to its LCST. With an increased in polymer loading, the water adsorption decreased for both 50 % RH and 95 % RH, **Figure 2.8**. Water content measurements revealed the change in CNCs structural coloration is due to the water molecules residing at the rods' surface, infiltrating CNC layers, and expanding the pitch.[11,14] This was observed in GISAXS measurement (**See Appendix A2)** in which the d-spacing of the soaked films linearly increased from 6.3 nm to 8.9 nm for 5 % to 30 % $PMEO_2MA$-CNC. Varying the $PMEO_2MA$ loading and humidity conditions provide tunability of reflectance wavelength in visible light spectrum. The response is reversible; the films can revert back to the initial reflectance when the water content is evaporated slowly and does not affect CNCs cholesteric structure. However, reflectance peak broadening could be due to uneven water penetration.[6]

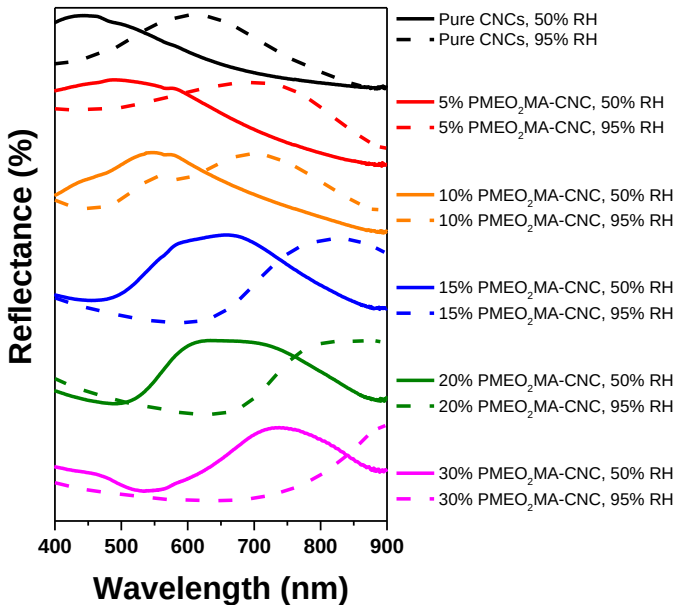

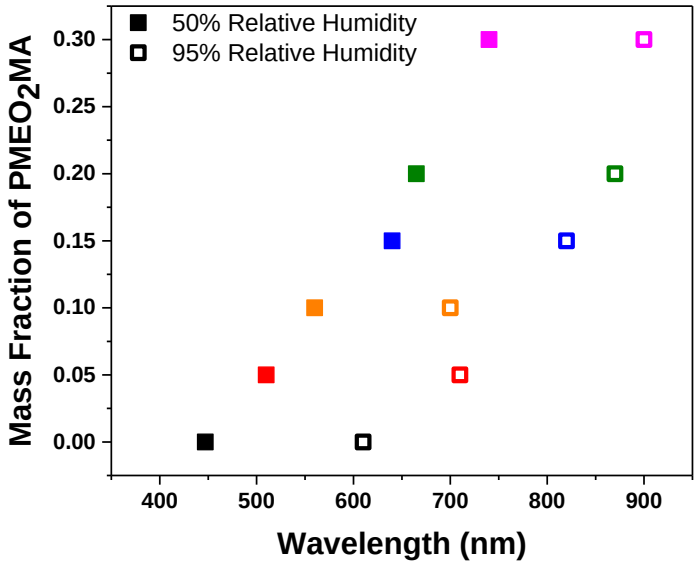

Figure 2.7. Reflectance spectra of the CNC nanocomposite films at 55 % RH (solid lines) and 95 % RH (dashed lines) (top). The reflectance peaks shifted 140 nm – 200 nm to higher wavelengths (bottom).

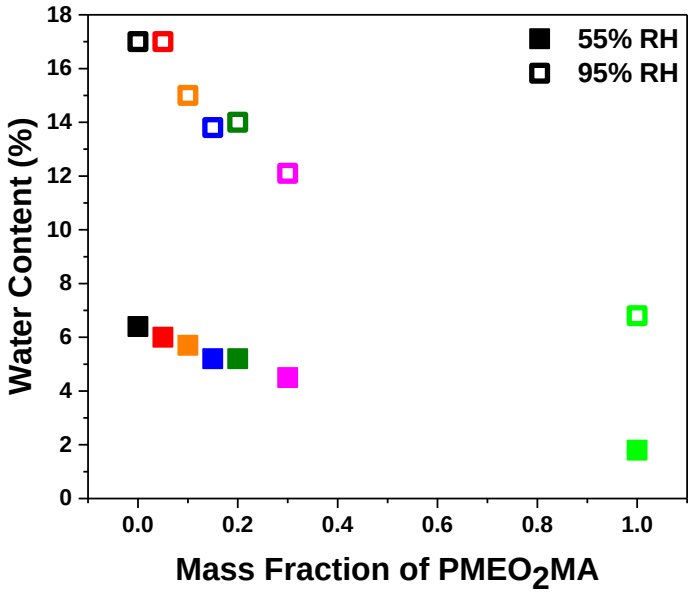

Figure 2.8. TGA of the $PMEO_2MA$-CNC samples to quantify the water content at 19 °C in 55 % RH and 95 % RH. Analysis done in N_2 environment heating from room temperature to 150 °C with 10 K/minute ramp rate then allowed to equilibrate for 30 minutes at 150 °C.

At 95 % RH hydration level, the $PMEO_2MA$-CNC films did not exhibit thermoresponsive behavior when heated above the critical temperature of 26 °C. Literature

has reported on thermoresponsive polymers with LCSTs, poly(N-isopropylacrylamide), poly(oligoethylene glycol methacrylate), and Jeffermine polyetheramine, grafted on CNCs to create a stimuli-responsive CNCs in aqueous solution for applications in sensors or thermo-sensitive materials.[15–21] The grafted thermoresponsive CNC systems behaved similarly to their homopolymer counterpart and exhibited reversible phase transition in aqueous solution with very low concentration of grafted CNCs. Despite these explorations, they have yet to examine how thermoresponsive polymers will behave in the solid-state with a minimal amount of water present.

To induce phase transition in the films, $PMEO_2MA$-CNC films was exposed to a limited amount of water and then temperatures of 0 °C, 21 °C, and 50 °C. Pure CNCs did not undergo optical change in the temperature range. The CNC nanocomposites films showed a progression from being transparent at 0 °C to opaque at 50 °C, in **Figure 2.9**. The opacity appeared to increase with polymer loading because of $PMEO_2MA$ contribution to temperature response similar to when it is in aqueous solution. The phase transition was reversible and occurred in less than 3 seconds. When water is removed from the soaked films, the films lost the thermoresponsive behavior and revert back to the initial color. The experiment indicated the importance of water component for $PMEO_2MA$-CNC films to undergo phase transition.

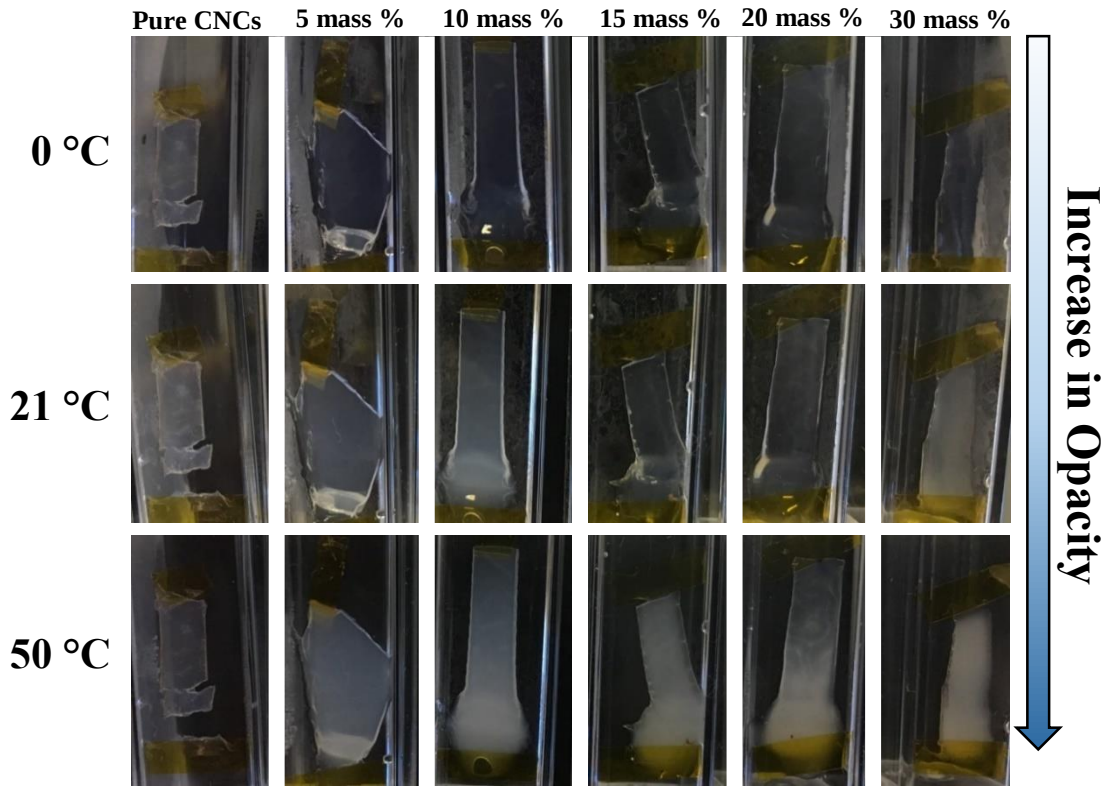

Figure 2.9. All the $PMEO_2MA$-CNC films soaked in water were exposed to three temperatures: 0 °C (top), 21 °C (middle), and 50 °C (bottom).

To determine the cloud point temperatures in solid-state, UV-vis spectroscopy measured change in the transmittance wavelength of soaked $PMEO_2MA$-CNC films from 18 °C to 50 °C, shown in **Figure 2.10**. The transmittance for pure CNCs remained constant throughout the temperature range while the transmittance decreased for $PMEO_2MA$-CNC nanocomposites. The phase transition occurred around 25 °C to 29 °C when transmittance reached 50 %. This range is comparable to $PMEO_2MA$ LCST at 26 °C in aqueous solution.[22] The observation reveals $PMEO_2MA$ still undergoes the reversible phase separation in solid-state and responds similarly to when it is in aqueous solution.

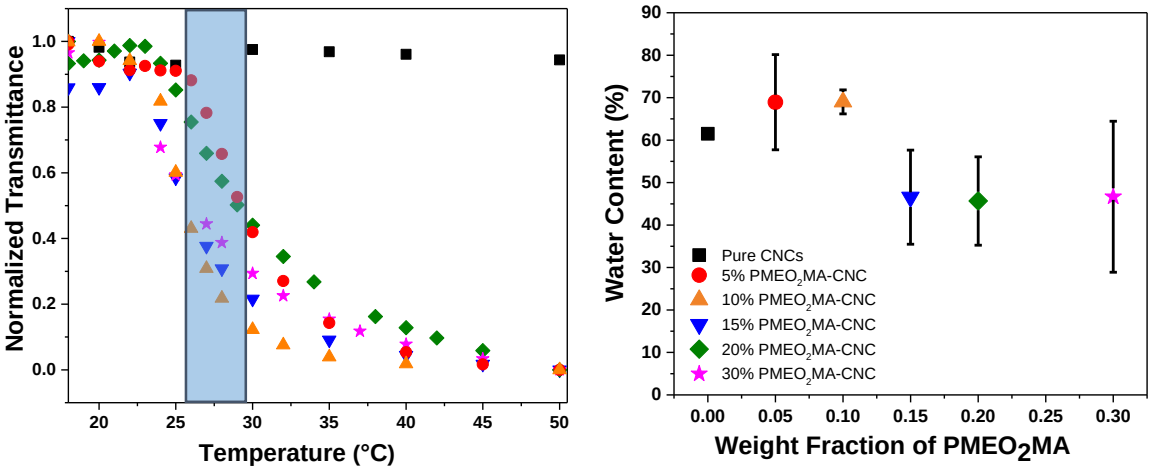

Figure 2.10. Transmittance measurements of soaked $PMEO_2MA$-CNC samples from 18 °C to 50 °C to determine the cloud point at 650 nm wavelength (left). The cloud points range from 25 °C to 29 °C. Comparison between water content versus mass fraction of $PMEO_2MA$ was plotted (right).

Water content in soaked nanocomposite films were measured to estimate the minimum amount of water needed to exhibit phase transition behavior. The 5 mass % and 10 mass % $PMEO_2MA$-CNC needed an average of 70 mass % of water while 15 % to 30 mass % $PMEO_2MA$-CNC needed 45 mass % of water to observe the thermoresponsive behavior, shown in **Figure 2.10**. At lower polymer loadings, water might have been adsorbed by CNCs component before it reached $PMEO_2MA$, hence, higher water content is needed to induce the phase transition. Demand for water content was reduced at higher polymer content and increased the chance of interaction between $PMEO_2MA$ and water for the cloud point to occur. A significant amount of water is needed for thermoresponsive behavior to occur in comparison to the water content at 95 % RH (12 % to 17 mass % of water), **Figure 2.8**.

To determine if there is hysteresis with heating versus cooling cycles, transmittance measurements were conducted on soaked 5 % to 30 % $PMEO_2MA$-CNC from 18 °C to 45 °C. All $PMEO_2MA$-CNC samples exhibited hysteresis but there was a prominent hysteresis

in the 5 % $PMEO_2MA$-CNC. There are two hypotheses to explain this observation. At 5 mass % polymer loading, it could take 5 % $PMEO_2MA$-CNC longer to respond to the heating/cooling cycle while the other $PMEO_2MA$-CNC samples have a substantial amount of polymer that response time is not delayed. The other possibility has to do with the polymer component in 5 % $PMEO_2MA$-CNC being physically attracted to the CNCs surface due to secondary forces (van der Waals and hydrogen bonding). The adhesion could hinder the polymer chains mobility, making it difficult for the chains to change configuration and ultimately result in hysteresis.

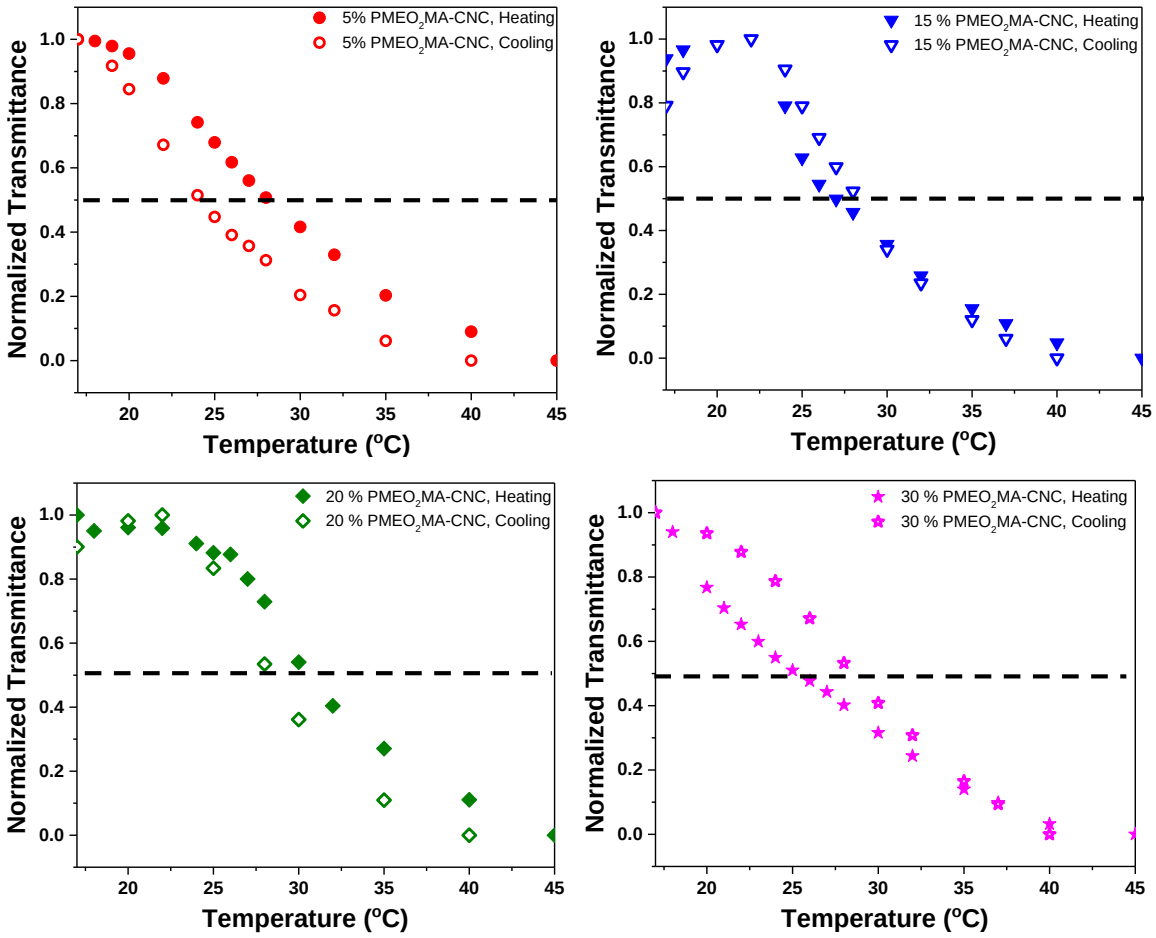

Figure 2.11. Transmittance measurements of $PMEO_2MA$-CNC from 18 °C to 45 °C at 650 nm wavelength. The closed and opened symbols represent heating and cooling cycles, respectively.

2.3.3. Mechanical and Morphology Characterization

Mechanical properties were examined to observe the effects of $PMEO_2MA$ on the films' mechanical performances. To ensure the stress of the material was recorded accurately, the $PMEO_2MA$-CNC films thickness was measured via SEM. Using the equation below, the stress was calculated with the measured thickness.

$$\boldsymbol{Stress}\ [\boldsymbol{Pa}] = \frac{\boldsymbol{Force}}{\boldsymbol{Cross-section}} = \frac{\boldsymbol{Force}\ [\boldsymbol{N}]}{(\boldsymbol{Thickness} \times \boldsymbol{Width})\ [\boldsymbol{m^2}]}$$

The sample strips were 4 mm in width and 30 mm in length while the thickness was measured by SEM and summarized in **Table 2.1**. From the stress-strain curves shown in **Figure 2.12**, pure CNCs had high tensile strength but suffered from brittleness due to the absence of an energy-dissipating polymer component.[11] As polymer incorporation increased, tensile strength decreased but the strain increased. The $PMEO_2MA$-CNC nanocomposite films had more flexibility and yield compared to pure CNCs. Toughness and strain peaked at 20 % $PMEO_2MA$-CNC sample. Its cross-section exhibited the Bouligand structures like other samples but AFM phase images (**Figure 2.13**), revealed a unique self-assembly of a nonwoven morphology at the film's interface that could contribute to high toughness. Mechanical trends obtained from $PMEO_2MA$-CNC samples were observed similar to other reported blended polymer-CNCs composites.[9–11,23,24] Improvement in flexibility can be observed at 10 mass % polymer. The soft polymer component dissipated friction from CNC rods against each other, indicating good interfacial adhesion and stress transfer between the polymer and CNC components.[10,11]

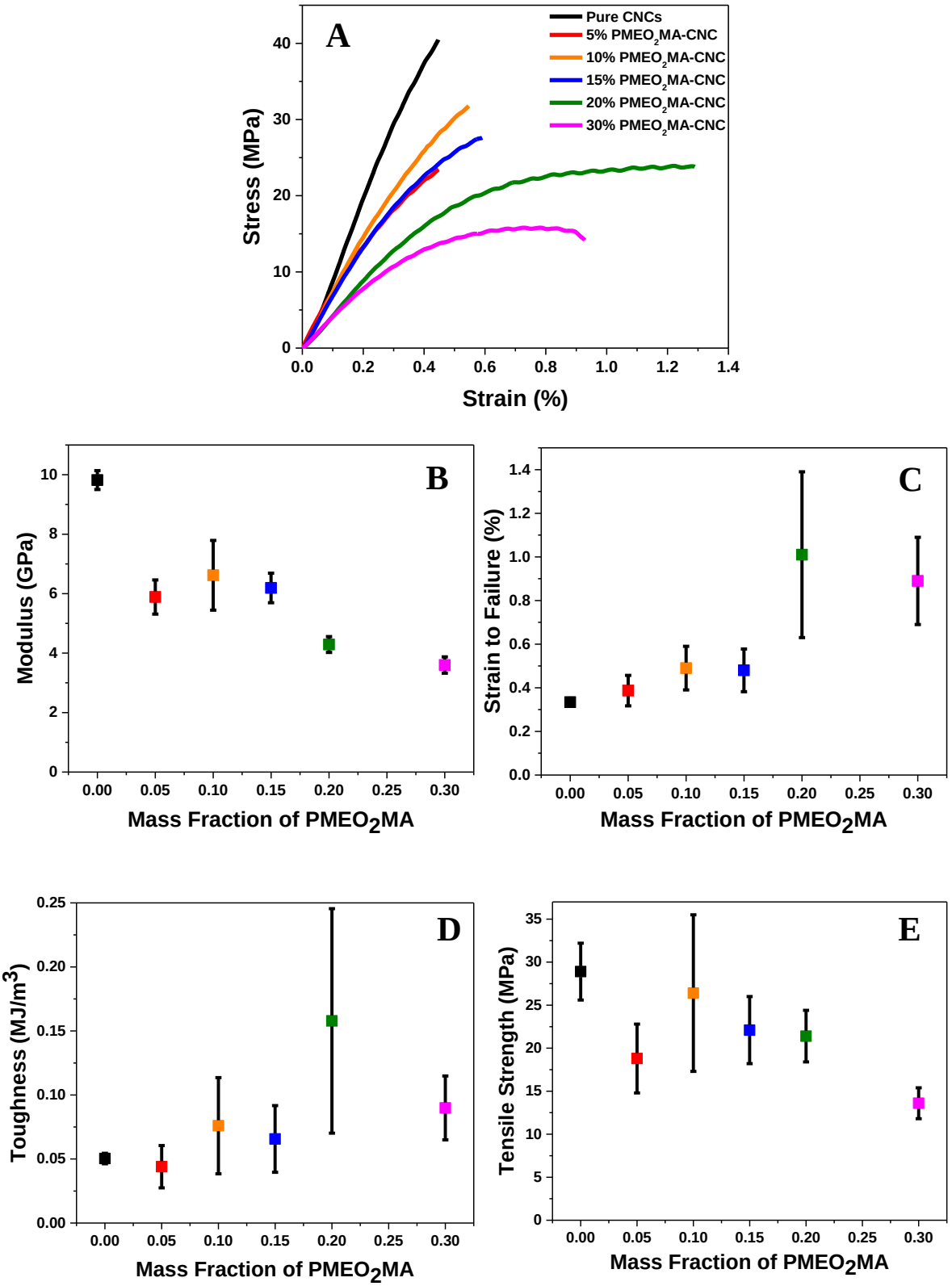

Figure 2.12. Mechanical properties of $PMEO_2MA$-CNC films where A) stress-strain curves, B) modulus, C) strain to failure, D) toughness, and E) tensile strength as a function of $PMEO_2MA$.

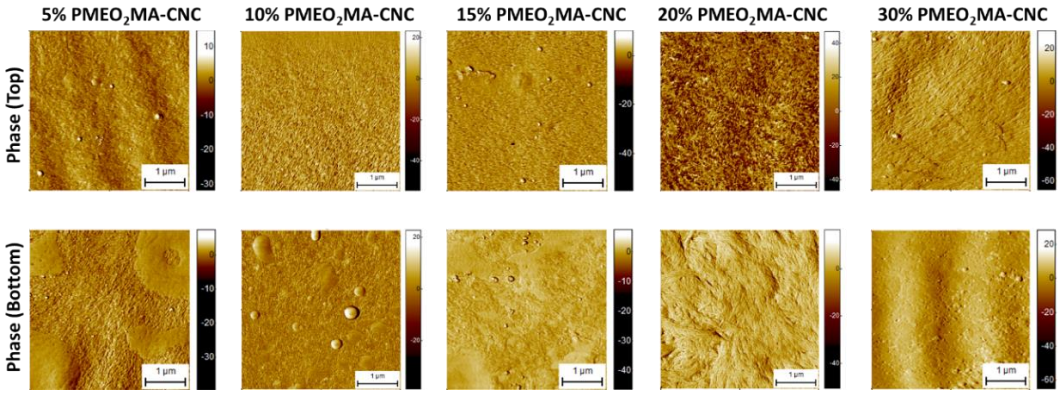

Figure 2.13. Phase images for the [(5, 10, 15, 20, 30) mass % of $PMEO_2MA$] films are shown. The top side of the CNC films (sample-air interface) are on the top row and the bottom side of the films (sample-substrate interface) are the bottom row.

2.4. Conclusions

Blending $PMEO_2MA$ with CNCs was a facile method to provide stimuli-responsiveness and toughness to CNC films. By varying $PMEO_2MA$ mass loading, the CNCs structural colors could be tuned from blue to red. The resulting CNC nanocomposite films demonstrated reversible optical responses under humidity and temperature conditions within the visible light spectrum. The tunability of CNCs nanocomposites make them ideal as visual detectors, expanding potential applications to colorimetric sensors, photonics, optically active coatings, and materials sensitive to human-contact. The dynamic responses of CNC nanocomposites led to further explorations that seek to understand how the microscopic scale translates to macroscopic properties.

2.5. References

(1) Habibi, Y.; Lucia, L. A.; Rojas, O. J. Cellulose Nanocrystals: Chemistry, Self-Assembly, and Applications. *Chem. Rev.* **2010**, *110* (6), 3479–3500. https://doi.org/10.1021/cr900339w.

(2) Sacui, I. A.; Nieuwendaal, R. C.; Burnett, D. J.; Stranick, S. J.; Jorfi, M.; Weder, C.; Foster, E. J.; Olsson, R. T.; Gilman, J. W. Comparison of the Properties of Cellulose Nanocrystals and Cellulose Nanofibrils Isolated from Bacteria, Tunicate, and Wood Processed Using Acid, Enzymatic, Mechanical, and Oxidative Methods. *ACS Appl. Mater. Interfaces* **2014**, *6* (9), 6127–6138. https://doi.org/10.1021/am500359f.

(3) Anglès, M. N.; Dufresne, A. Plasticized Starch/Tunicin Whiskers Nanocomposite Materials. 2: Mechanical Behavior. *Macromolecules* **2001**, *34* (9), 2921–2931. https://doi.org/10.1021/ma001555h.

(4) Lutz, Jean-Francois and Hoth, A. Preparation of Ideal PEG Analogues with a Tunable Thermosensitivity by Controlled Radical Copolymerization of 2-(2-Methoxyethoxy)Ethyl Methacrylate and Oligo(Ethylene Glycol) Methacrylate. *Macromolecules* **2006**, *39* (2), 893–896. https://doi.org/10.1021/ma0517042.

(5) Lutz, Jean-Francois, Weichenhan, Katja, Akdemir, Ozgur, Hoth, A. About the Phase Transitions in Aqueous Solutions of Thermoresponsive Copolymers and Hydrogels Based on 2- (2-Methoxyethoxy) Ethyl Methacrylate and Oligo (Ethylene Glycol) Methacrylate. *Macromolecules* **2007**, *40* (7), 2503–2508. https://doi.org/10.1021/ma062925q.

(6) Natarajan, B.; Emiroglu, C.; Obrzut, J.; Fox, D. M.; Pazmino, B.; Douglas, J. F.; Gilman, J. W. Dielectric Characterization of Confined Water in Chiral Cellulose Nanocrystal Films. *ACS Appl. Mater. Interfaces* **2017**, *9* (16), 14222–14231. https://doi.org/10.1021/acsami.7b01674.

(7) Natarajan, B.; Krishnamurthy, A.; Qin, X.; Emiroglu, C. D.; Forster, A.; Foster, E. J.; Weder, C.; Fox, D. M.; Keten, S.; Obrzut, J.; Gilman, J. W. Binary Cellulose Nanocrystal Blends for Bioinspired Damage Tolerant Photonic Films. *Adv. Funct. Mater.* **2018**, *28* (26), 1800032. https://doi.org/10.1002/adfm.201800032.

(8) Salajkova, M.; Noh, J.; Park, J. H.; Lagerwall, J. P. F.; Schu, C. Cellulose Nanocrystal-Based Materials : From Liquid Crystal Self-Assembly and Glass Formation to Multifunctional Thin Films. *NPG Asia Mater.* **2014**, No. 6, 1–12. https://doi.org/10.1038/am.2013.69.

(9) Wan, H.; Li, X.; Zhang, L.; Li, X.; Liu, P.; Jiang, Z.; Yu, Z. Z. Rapidly Responsive and Flexible Chiral Nematic Cellulose Nanocrystal Composites as Multifunctional Rewritable Photonic Papers with Eco-Friendly Inks. *ACS Appl. Mater. Interfaces* **2018**, *10* (6), 5918–5925. https://doi.org/10.1021/acsami.7b19375.

(10) Wang, B.; Walther, A. Self-Assembled, Iridescent, Crustacean-Mimetic Nanocomposites with Tailored Periodicity and Layered Cuticular Structure. *ACS Nano* **2015**, *9* (11), 10637–10646. https://doi.org/10.1021/acsnano.5b05074.

(11) Yao, K.; Meng, Q.; Bulone, V.; Zhou, Q. Flexible and Responsive Chiral Nematic Cellulose Nanocrystal/Poly(Ethylene Glycol) Composite Films with Uniform and Tunable Structural Color. *Adv. Mater.* **2017**, *29* (28), 1–8. https://doi.org/10.1002/adma.201701323.

(12) Vargas, W.; Avendano, E.; Hernández-Jiménez, M.; Azofeifa, D.; Libby, E.; Solís, Á.; Barboza-Aguilar, C. Photonic Crystal Characterization of the Cuticles of Chrysina Chrysargyrea and Chrysina Optima Jewel Scarab Beetles. *Biomimetics* **2018**, *3* (4), 30. https://doi.org/10.3390/biomimetics3040030.

(13) He, Y.; Zhang, Z.; Xue, J.; Wang, X.; Song, F.; Wang, X.; Zhu, L.; Wang, Y. Biomimetic Optical Cellulose Nanocrystal Films with Controllable Iridescent Color and Environmental Stimuli-Responsive Chromism. *ACS Appl. Mater. Interfaces* **2018**, *10* (6), 5805–5811. https://doi.org/10.1021/acsami.7b18440.

(14) Aulin, C.; Ahok, S.; Josefsson, P.; Nishino, T.; Hirose, Y.; Österberg, M.; Wågberg, L. Nanoscale Cellulose Films with Different Crystallinities and Mesostructures - Their Surface Properties and Interaction with Water. *Langmuir* **2009**, *25* (13), 7675–7685. https://doi.org/10.1021/la900323n.

(15) Risteen, B.; Delepierre, G.; Srinivasarao, M.; Weder, C.; Russo, P.; Reichmanis, E.; Zoppe, J. Thermally Switchable Liquid Crystals Based on Cellulose Nanocrystals with Patchy Polymer Grafts. *Small* **2018**, *14* (46), 1–10. https://doi.org/10.1002/smll.201802060.

(16) Zoppe, J. O.; Dupire, A. V. M.; Lachat, T. G. G.; Lemal, P.; Rodriguez-Lorenzo, L.; Petri-Fink, A.; Weder, C.; Klok, H. A. Cellulose Nanocrystals with Tethered Polymer Chains: Chemically Patchy versus Uniform Decoration. *ACS Macro Lett.* **2017**, *6* (9), 892–897. https://doi.org/10.1021/acsmacrolett.7b00383.

(17) Zoppe, J. O.; Österberg, M.; Venditti, R. A.; Laine, J.; Rojas, O. J. Surface Interaction Forces of Cellulose Nanocrystals Grafted with Thermoresponsive Polymer Brushes. *Biomacromolecules* **2011**, *12* (7), 2788–2796. https://doi.org/10.1021/bm200551p.

(18) Porsch, C.; Hansson, S.; Nordgren, N.; Malmström, E. Thermo-Responsive Cellulose-Based Architectures: Tailoring LCST Using Poly(Ethylene Glycol) Methacrylates. *Polym. Chem.* **2011**, *2* (5), 1114–1123. https://doi.org/10.1039/c0py00417k.

(19) Zoppe, J. O.; Habibi, Y.; Rojas, O. J.; Venditti, R. A.; Johansson, L. S.; Efimenko, K.; Österberg, M.; Laine, J. Poly(N -Isopropylacrylamide) Brushes Grafted from Cellulose Nanocrystals via Surface-Initiated Single-Electron Transfer Living Radical Polymerization. *Biomacromolecules* **2010**, *11* (10), 2683–2691. https://doi.org/10.1021/bm100719d.

(20) Azzam, F.; Siqueira, E.; Fort, S.; Hassaini, R.; Pignon, F.; Travelet, C.; Putaux, J. L.; Jean, B. Tunable Aggregation and Gelation of Thermoresponsive Suspensions of Polymer-Grafted Cellulose Nanocrystals. *Biomacromolecules* **2016**, *17* (6), 2112–2119. https://doi.org/10.1021/acs.biomac.6b00344.

(21) Grishkewich, N.; Akhlaghi, S. P.; Zhaoling, Y.; Berry, R.; Tam, K. C. Cellulose Nanocrystal-Poly(Oligo(Ethylene Glycol) Methacrylate) Brushes with Tunable LCSTs. *Carbohydr. Polym.* **2016**, *144*, 215–222. https://doi.org/10.1016/j.carbpol.2016.02.044.

(22) Han, S.; Hagiwara, M.; Ishizone, T. Synthesis of Thermally Sensitive Water-Soluble Polymethacrylates by Living Anionic Polymerizations of Oligo (Ethylene Glycol) Methyl Ether Methacrylates. *Macromolecules* **2003**, *36* (22), 8312–8319. https://doi.org/10.1021/ma0347971.

(23) Vollick, B.; Kuo, P. Y.; Thérien-Aubin, H.; Yan, N.; Kumacheva, E. Composite Cholesteric Nanocellulose Films with Enhanced Mechanical Properties. *Chem. Mater.* **2017**, *29* (2), 789–795. https://doi.org/10.1021/acs.chemmater.6b04780.

(24) Tatsumi, M.; Teramoto, Y.; Nishio, Y. Polymer Composites Reinforced by Locking-in a Liquid-Crystalline Assembly of Cellulose Nanocrystallites. *Biomacromolecules* **2012**, *13* (5), 1584–1591. https://doi.org/10.1021/bm300310f.

CHAPTER 3. LOCAL DYNAMIC OF THERMORESPONSIVE POLYMERS ON CELLULOSE NANOCRYSTALS

3.1. Abstract

Polymer nanocomposites containing self-assembled cellulose nanocrystals (CNCs) are ideal for advanced applications requiring both strength and toughness, as their helical structure deflects crack propagation and the polymer matrix dissipates impact energy. However, any adsorbed water layer surrounding the CNC rods may compromise interfacial adhesion between the polymer matrix and the CNCs, thus impacting stress transfer at that interface. Therefore, it is critical to study the role of water at the interface on the coupling between polymer dynamics and the resulting mechanical performance of the nanocomposite. Here, we explore the role of polymer confinement and water content on polymer dynamics in CNC nanocomposites by covalently attaching a fluorogenic water-sensitive dye to poly(diethylene glycol methyl ether methacrylate) ($PMEO_2MA$), to provide insight into the observed mechanical performance. Utilizing fluorescence lifetime imaging microscopy (FLIM), the lifetime of the dye fluorescence decay was measured to probe polymer chain dynamics of $PMEO_2MA$ in the CNC nanocomposite films. These studies demonstrated FLIM as a method to investigate polymer nanosecond-dynamics in CNC nanocomposites.

3.2. Experimental

To track chain dynamics, the $PMEO_2MA$ was labelled with a Rhodamine-based water-sensitive dye. First, Rhodamine-B was modified with ethanolamine to synthesize the water-sensitive dye, called RhB-ethanolamine. The RhB-ethanolamine precursor was then reacted with methacryloyl chloride to modify it into a monomer that can then be copolymerized with MEO_2MA. A synthesis schematic is shown in **Figure 3.1.**

3.2.1. Materials

A 12.1 mass % of sodium-neutralized sulfated wood cellulose nanocrystals (Na-CNCs) as an aqueous suspension was obtained from the University of Maine Process Development Center. Di(ethylene glycol) methyl ether methacrylate (MEO_2MA, 95 %), copper (I) bromide (CuBr, 99.999 %), N,N,N',N'',N''-pentamethyldiethylenetriamine (PMDETA, 99 %), ethyl α-bromoisobutyrate (EBriB, 98 %), Rhodamine B (RhB, ≥ 95 %), ethanolamine (≥ 95 %), methacryloyl chloride (97 %), ethyl alcohol, anhydrous (EtOH, > 99.5 %), anisole, anhydrous (99.7 %) were purchased from Sigma-Aldrich. Hexanes (95 %) and dichloromethane (DCM) were purchased from Fisher Scientific. Copper (II) bromide ($CuBr_2$, 99 %) and triethylamine (TEA, 99 %) were purchased from Alfa Aesar.

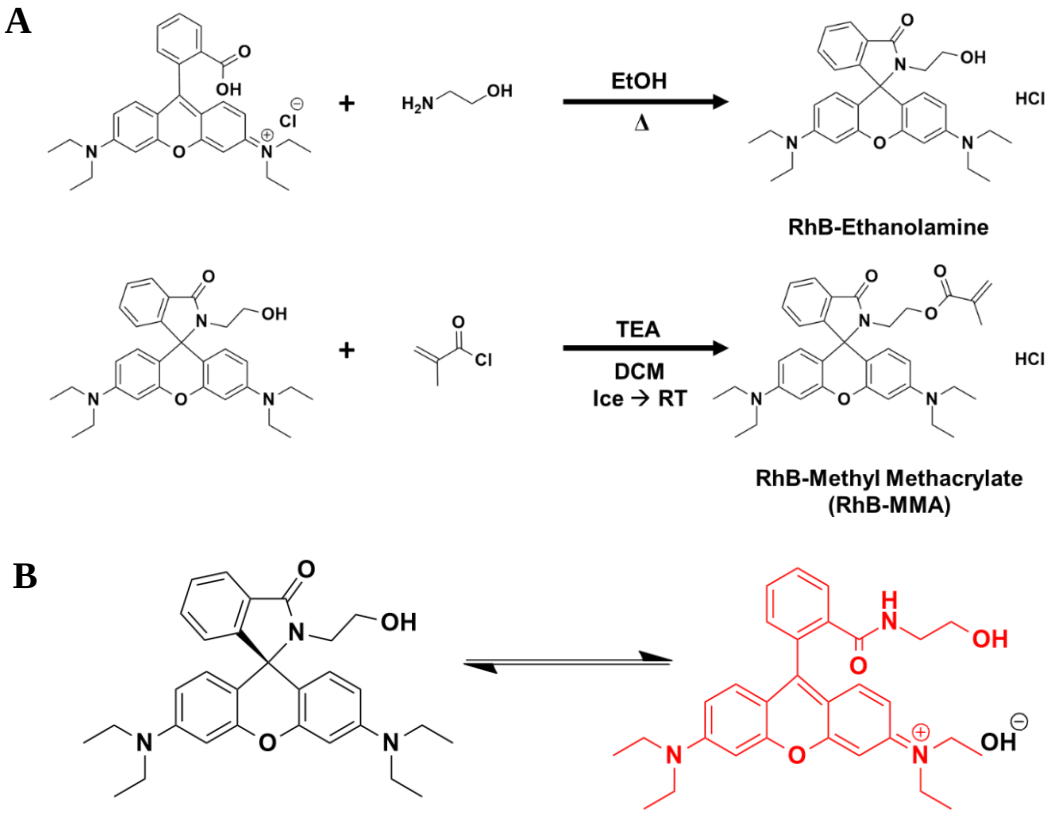

Figure 3.1. Schematic of a) rhodamine-B was reacted with ethanolamine to form a spirolactam intermediate (RhB-ethanolamine). The RhB-ethanolamine intermediate is further reacted with methacryloyl chloride to form the methacrylated monomer (RhB-MMA) b) RhB dye is activated with 365 nm light and water to open the spirolactam ring.

3.2.2. Synthesis of Rhodamine-ethanolamine precursor

To synthesize the water-sensitive dye, a synthetic route was adapted from the literature.[1] In a 50 mL round-bottomed flask, Rhodamine-B (RhB) (0.57 g, 1.2 mmol) and 20 mL of anhydrous ethanol were added and stirred for 15 minutes under nitrogen. Ethanolamine (3.7 g, 61 mmol) was then added to the flask and the reaction refluxed overnight in the dark to prevent photoactivation of the product. For the purification process, 100 mL deionized (DI) water was added and the resulting solution was extracted against chloroform. The chloroform solution was collected, dried over sodium sulfate overnight, then the chloroform was removed via rotary evaporation. The recovered Rhodamine-ethanolamine (RhB-ethanolamine) was dissolved with a minimum amount of ethyl acetate, and the solution was passed through a neutral alumna column to remove unreacted Rhodamine-B. Ethyl acetate was removed via rotary evaporation and the product was dried in a vacuum oven. The product was isolated as a white powder; proton nuclear magnetic resonance (^{1}H NMR) is shown in **Figure 3.2**.

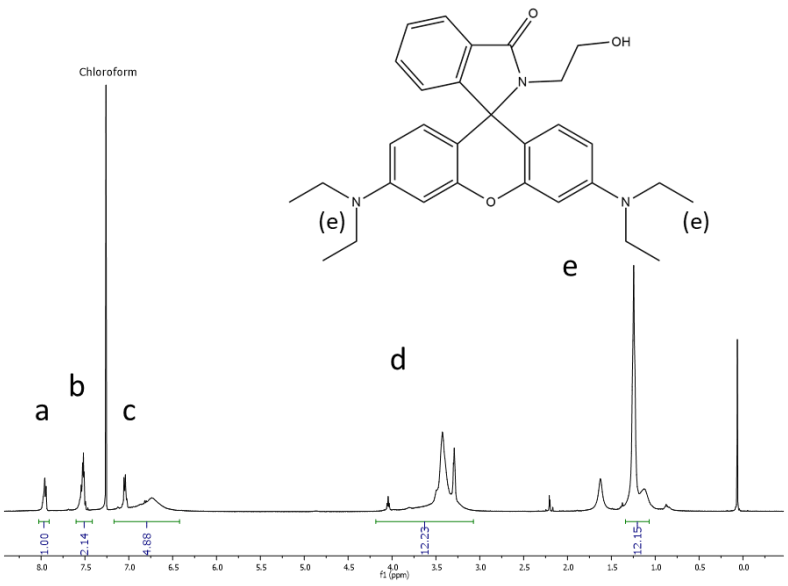

Figure 3.2. ^{1}H NMR of RhB-Ethanolamine

3.2.3. Synthesis of Rhodamine-Methyl Methacrylate (RhB-MMA)

In a 100 mL round-bottomed flask, RhB-ethanolamine (0.09 g, 0.18 mmol), 15 mL of anhydrous dichloromethane (DCM), and triethylamine (TEA, 0.26 g, 2.6 mmol) were added and stirred for 15 minutes under nitrogen. A dilute solution of methacryloyl chloride (0.21 g, 2 mmol) in 3 mL DCM was added dropwise to the reaction solution that had been placed in an ice bath. The ice bath was removed after the addition was completed, and the reaction was conducted at room temperature overnight. To purify the product, the reaction solution was diluted with DCM and washed with saturated sodium bicarbonate, a 0.5 M NaOH solution, and then rinsed with water. The organic phase was dried with $MgSO_4$ and the DCM was removed via rotary evaporation. Rhodamine-MMA (RhB-MMA) was dissolved in a minimum amount of ethyl acetate, and the solution passed through neutral alumina column. Ethyl acetate was removed via rotary evaporation and the product was dried in a vacuum oven. The product was a clear and viscous oil; ^{1}H NMR and ESI-TOF are shown in **Figure 3.3**.

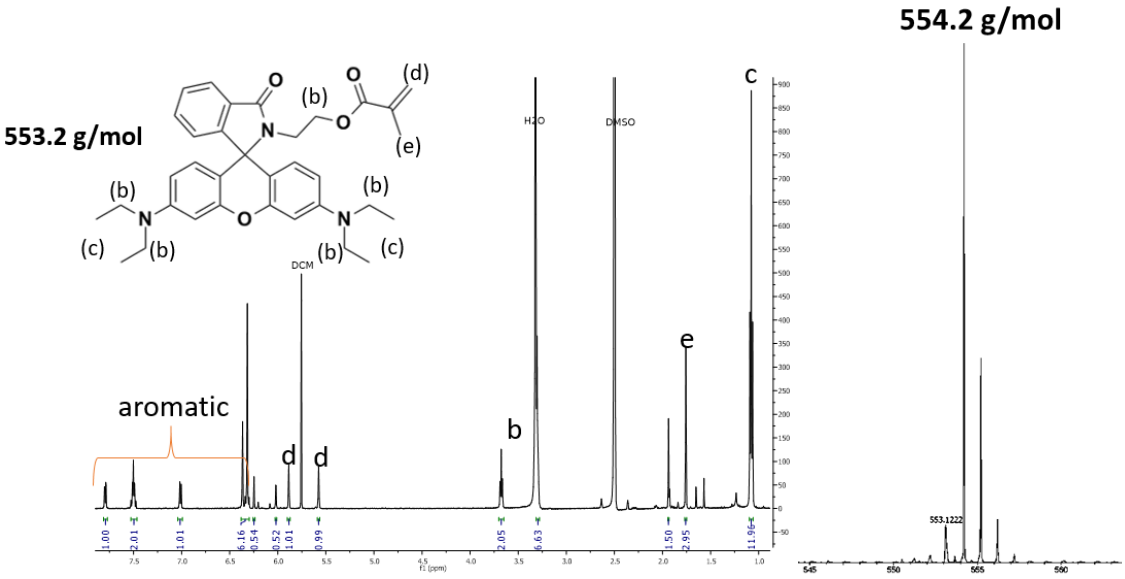

Figure 3.3. ^{1}H NMR (left) and ESI-TOF of RhB-MMA (right)

3.2.4. Copolymerization of MEO_2MA with RhB-MMA

Diethylene glycol methyl ether methacrylate (MEO_2MA) was passed through basic alumina column to remove inhibitors before polymerization. In a 20 mL reaction vial, 3 mL of MEO_2MA, 3 mL anhydrous anisole, $CuBr_2$ (0.0024g, 0.011 mmol), and CuBr (0.016 g, 0.11 mmol) were added and purged with nitrogen. The ligand (PMDETA, 0.023 g, 0.13 mmol), the initiator (EBriB 0.016 ml, 0.11 mmol), and a solution of RhB-MMA in anisole (0.03 g, 0.055 mmol) were then added. The reaction solution was heated to 70 °C for 7 hours. To terminate the polymerization, the reaction solution was placed in an ice bath then exposed to air. The solution was then diluted using a minimum amount of acetone and passed through basic alumina column to remove the copper species before precipitating the polymer in hexanes. The poly((diethylene glycol methacrylate)-*co*-RhB-MMA) ($PMEO_2MA$-RhB) had a number average relative molecular mass (M_n) of 19,900 g/mol with Đ = 1.3 based on dimethylformamide-gel permeation chromatography (DMF-GPC) with polymethylmethacrylate (PMMA) standards. The polymer was also analyzed by another DMF-GPC equipped with a UV detector at 254 nm to ensure that the water-sensitive dye was incorporated to the polymer chains and there is no free dye present at low molecular mass, show in **Figure 3.4.**

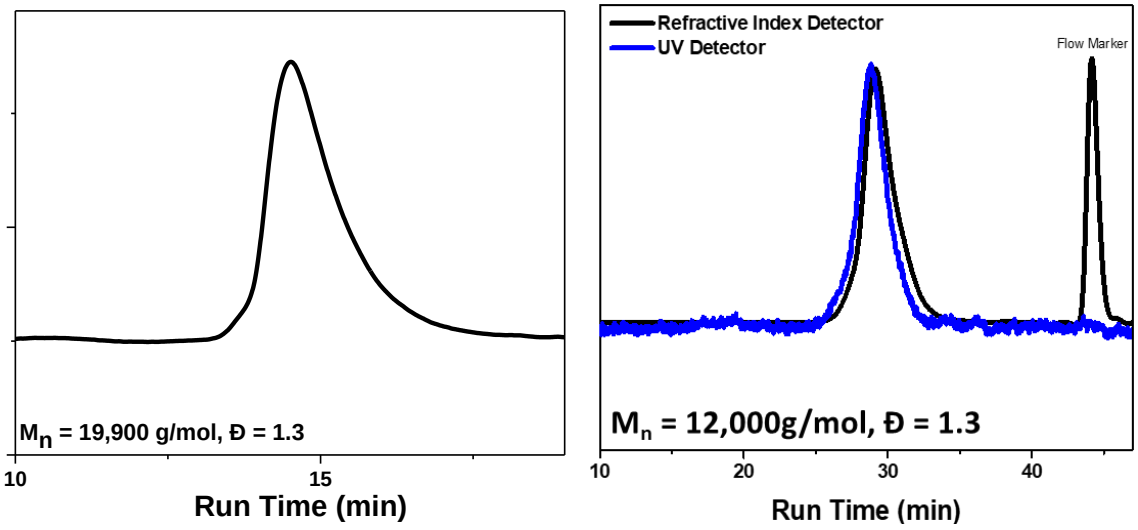

Figure 3.4. Molecular mass of $PMEO_2MA$RhB using DMF-GPC with PMMA standards (left) and DMF-GPC with both refractive index and UV detectors with PEG standards (right).

3.2.5. Experimental Conditions

The $PMEO_2MA$-RhB-CNCs films were cast via evaporation induced self-assembly following the same procedure as mentioned in **Section 2.3**. Since the water-sensitive dye is UV-sensitive, the Rhodamine-based water-sensitive dye $PMEO_2MA$ solution was placed in amber vials to prevent activation. The room where the casting took place also had amber lighting. For FLIM measurements, the $PMEO_2MA$-RhB-CNCs films were placed in a humidity chamber at 55 % relative humidity overnight to ensure all the films were equilibrated before imaging. To activate the RhB dye, films were placed under an UV-lamp (365 nm) until they turned pink. A Nikon A1 Spectral Detector Confocal with FLIM module was used to measure fluorescence lifetime in time domain with 40× objective with 0.6 numerical aperture and 488 nm laser pulse at 50 kHz. For FLIM measurements, the dwell time per pixel was 27.2 ns, with a scan size of 512 pixels × 512 pixels and a 0.39 µm pixel size. Images were taken under laser raster mode. The fluorescence was monitored by

binning events over time to construct a decay curve. The decay curves can be fitted as an exponential decay, using either single or multicomponent exponential fit.

3.3. Results and Discussion

3.3.1. Optical and Structural Characterization

To synthesize the water-sensitive dye, rhodamine-B was reacted with ethanolamine to form a spirolactam intermediate, RhB-ethanolamine, see **Figure 3.1A**. The RhB dye is non-fluorescent until activated with 365 nm light and water to open the spirolactam ring, see **Figure 3.1B**. The RhB cation forms a complex with $^{-}$OH that emits fluorescence around 590 nm. This ring-opening process can be reversed when heated above 80 °C, **Figure 3.1B**.[1] The RhB-ethanolamine intermediate is further reacted with methacryloyl chloride to form the methacrylated monomer (RhB-MMA), the synthesis schematic is shown in **Figure 3.1A**. The RhB-MMA was attached to $PMEO_2MA$ via ATRP. Based on absorbance of RhB-ethanolamine, roughly one out of every ten polymer chains have RhB-MMA molecule attached (**A4 & A5**).

Separate aqueous solutions containing 2 mass % of $PMEO_2MARhB$ and 2 mass % of Na-CNCs were combined in respective quantities to yield different polymer loading. The films were prepared by evaporation induced self-assembly (EISA) with varying mass fractions of $PMEO_2MARhB$ [(0, 5, 10, 15, 20, 30, 100) mass % of $PMEO_2MARhB$] at a constant drying rate. Previous efforts have shown that EISA of CNCs is affected by the rate of evaporation, thus it was crucial to maintain the same drying rate for all the samples to avoid major structural differences.[2,3]

Characterizing polymer confinements between the CNC rods can be assessed by observing the change in CNC pitch. Since the pitch is the height of a single helicoidal layer

in the Bouligand CNC structure,[4,5] a comparison between the polymer loading and pitch can be measured using polarized optical microscopy (POM), ultraviolet-visible (UV-vis) spectroscopy, and scanning electron microscopy (SEM).

The POM images in reflection mode record the structural coloration of the $PMEO_2MARhB$-CNC films, shown in **Figure 3.5**. The self-organized films indicate chiral-nematic ordering and form iridescent films that influence the photonic properties in the visible light spectrum.[6,7] As the $PMEO_2MARhB$ loading increased, the films transitioned from blue to red due to polymer infiltration. This observation was also seen in the literature that has blended CNCs with polymer and surfactant systems.[7–10] Structural and photonic properties can be tuned by incorporating polymers to expand the chiral-nematic pitch so as to scatter light from the visible to the near-IR. To quantify the reflective colors of the films, a UV-vis spectroscopy equipped with an integrating sphere spectrophotometer was used to measure average reflectance wavelength from different angles.[6] UV-vis spectra showed the peak reflectance maxima increased in wavelength linearly from 505 nm to 730 nm, as is shown in **Figure 3.6**. Interestingly, the 30 % $PMEO_2MARhB$-CNC has a very broad reflectance peak of 660 nm $\pm$ 97 nm. The broad reflectance range indicates some inhomogeneity in the film, with some regions being polymer rich resulting in higher reflectance wavelength. Polymer saturation in CNC Bouligand structures has been observed in literature for CNC-polymer blend films where there is an upper-limit of polymer content of 30 to 40 mass % in CNC matrix before it becomes phase separated.[7–9] There is a possible discrepancy in polymer distribution dependent on the region of the film due to the drying process that starts from the center and cascades outward.[2,5] To minimize this effect, POM and UV-vis measurements were analyzed at the center region of the film.

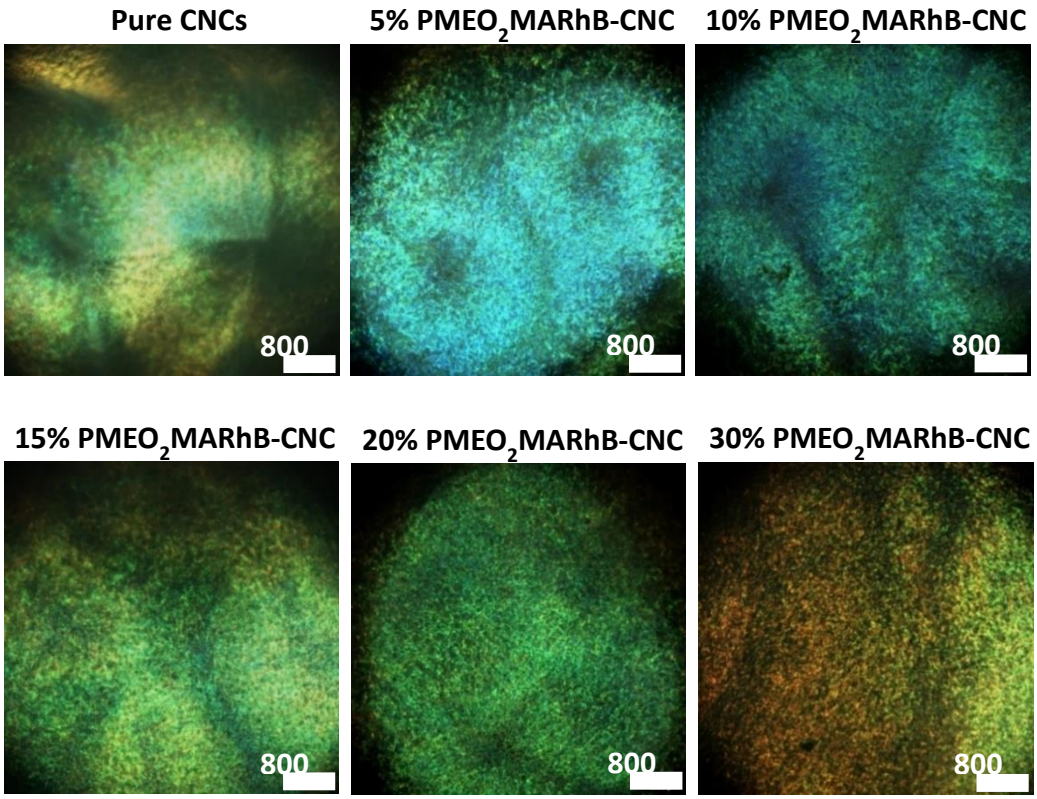

Figure 3.5. POM images of nanocomposite films of $PMEO_2MARhB$-CNC with [(0, 5, 10, 15, 20, 30, 100) mass % of $PMEO_2MARhB$] prepared via evaporation-induced self-assembly. Scale bar is 800 µm.

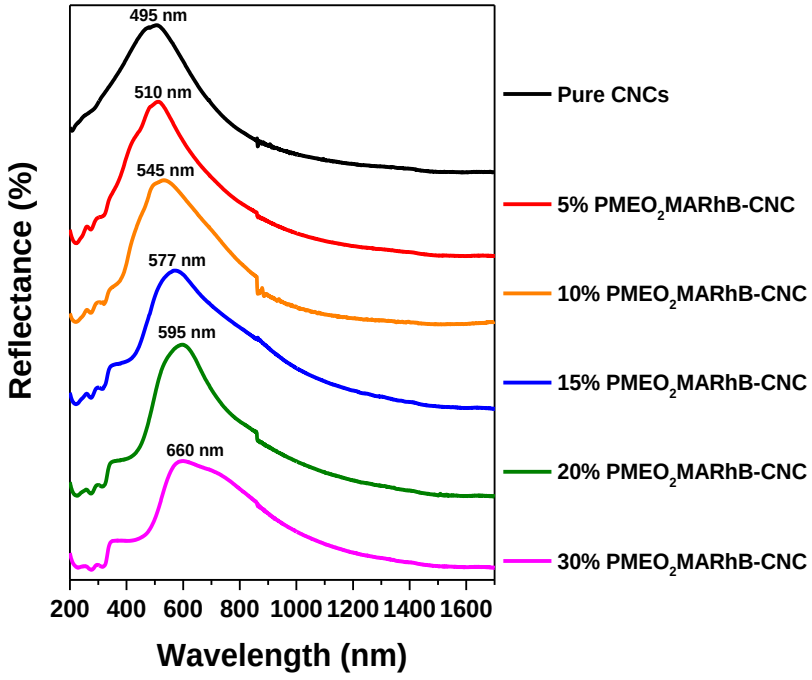

Figure 3.6. Reflectance measurements of pure CNCs and nanocomposite films of $PMEO_2MARhB$-CNC with [(0, 5, 10, 15, 20, 30, 100) mass % of $PMEO_2MARhB$].

CNC pitch can also be measured by looking at the films' cross-sections via SEM (**Figure 3.7**) and then compared to the results from UV-vis, **Table 3.1**. Based on the SEM measurements, the pitch from each sample exhibited the layered helical structure. The increasing distance between layered structure corresponds with the increasing polymer loading, which has been observed in other polymer-CNC blended systems.[7,9] To capture the variation in pitch within a sample, multiple measurements were taken at four different sections: top quartile, middle-top quartile, middle-bottom quartile, bottom quartile. Since the measured pitch via SEM and reflectance wavelength are complimentary, there is a linear correlation with both results showing polymer infiltration that intercalated between the CNC Bouligand structures. The pitch expansion results in longer reflectance wavelength and pitch length. With the physical polymer characterized, polymer dynamics was examined to correlate with this spatial restriction.

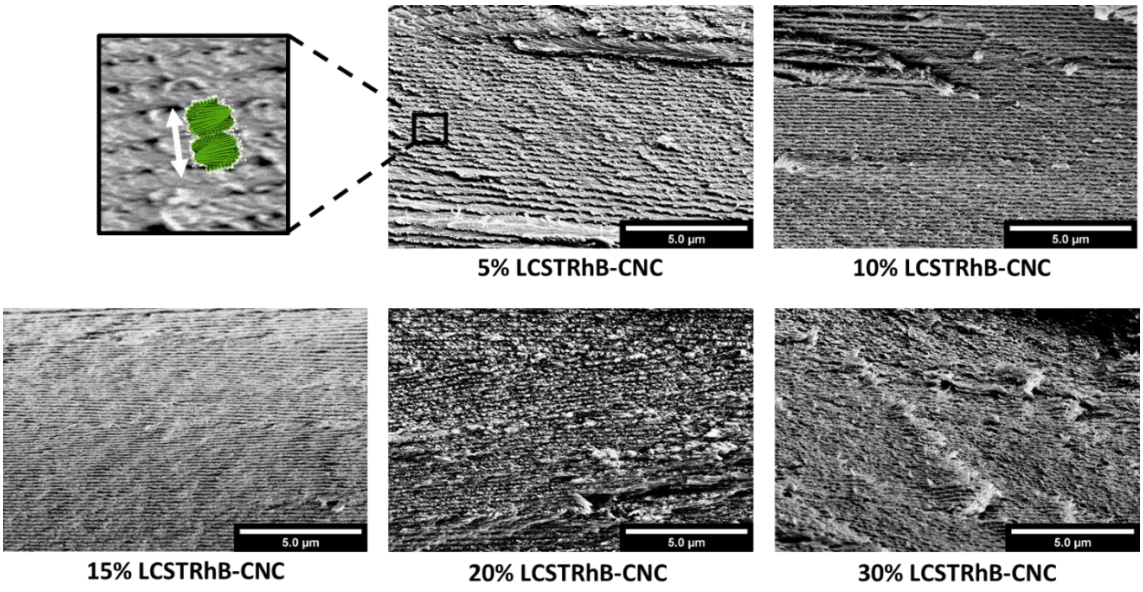

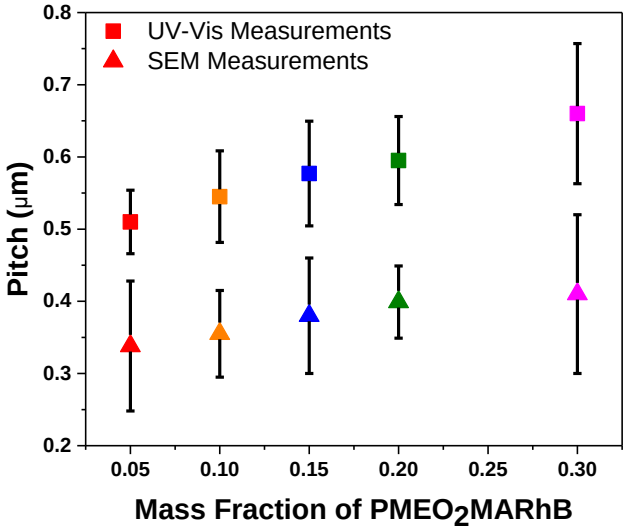

Figure 3.7. SEM images for the cross-sections of $PMEO_2MARhB$-CNC with [(0, 5, 10, 15, 20, 30, 100) mass % of $PMEO_2MARhB$] (top). Scale bar is 5 μm. Comparison between pitch measurements from UV-Vis and SEM for the $PMEO_2MARhB$-CNC films (bottom).

Table 3.1. Summary of $PMEO_2MARhB$-CNC films with thickness, pitch, and reflectance measurements

Sample	Thickness (μm)	Pitch average (μm)	Reflectance (nm)
5% $PMEO_2MARhB$-CNC	108 ± 2.8	0.338 ± 0.09	510 ± 44
10% $PMEO_2MARhB$-CNC	67.1 ± 1.5	0.355 ± 0.06	545 ± 64
15% $PMEO_2MARhB$-CNC	67.4 ± 1.8	0.380 ± 0.08	577 ± 73
20% $PMEO_2MARhB$-CNC	60.9 ± 0.71	0.399 ± 0.05	595 ± 61
30% $PMEO_2MARhB$-CNC	64.5 ± 29	0.41 ± 0.11	660 ± 97

3.3.2. Fluorescence Lifetime Imaging Microscopy to Probe Chains Dynamics

Utilizing time-resolved fluorescence lifetime imaging microscopy (FLIM), the fluorescence decay was measured to probe the dynamics of the labelled $PMEO_2MA$. The fluorescence lifetime is defined as the average time that a fluorophore remains in an excited state before returning to the ground state by emitting a photon. Fluorescence lifetime of the fluorophore is sensitive to the nano-environment and interactions with other molecules that cause non-radiative energy losses. FLIM provides the spatial distributions of the fluorophores and information about the molecular environment of the fluorophore at the nanosecond timescale.

Tanaka *et al*. used FLIM to study dynamics of confined polymers. They observed that fluorescence lifetime was dependent on molecular motion of the chains.[11] In general, a longer lifetime means that the decay is slow and the fluorophores are in a mobility restricted region. Conversely, a shorter lifetime is a result of non-radiative pathways present for fluorophores to decay quickly due to mobility in the surrounding environment. [11,12] FLIM images were captured to reveal the distribution of fluorescence lifetimes within the sample, **Figure 3.8 (top).** The images were scaled to the same color scheme for comparison, showing 5 and 10 mass % samples having more confinements while 30 mass % sample having more mobility. The average fluorescence lifetimes distribution (τ_m) for the $PMEO_2MA$RhB-CNC films were plotted to reveal a decrease in τ_m with increasing polymer loading. The 5 % $PMEO_2MA$RhB-CNC had a longer fluorescence lifetime since most of the polymer chains appeared to be confined CNCs surface due to physical absorption and attractive interactions. As more polymer is incorporated, the fluorescence lifetime shortened with fewer polymer chains being confined and instead having more mobility as polymer saturation was reached. This was explored in work by Seethamraju *et al.* where the fluorescence lifetime of the dye is more influenced by polymer dynamics than the nonradiative energy transfer to water molecules.[1]

However, while a single exponential is sufficient to obtain a good fit for the pure polymer or a uniform sample, all of the CNC films require two-component exponential fitting (τ_1 and τ_2) to capture the different local dynamics existing in CNC nanocomposites. Fluorescence lifetime distribution were offset and normalized for different polymer loadings in **Figure 3.8**. The three postulated environments are: i) polymer confined at the CNC interface, ii) polymer in-between the CNC structures where they are not confined at

the CNC interface, iii) polymer that is interacting with the water phase present in the composite films. All of the CNC nanocomposite films exhibit two or three environments where τ_1 and τ_2 represent short and long lifetimes, respectively. For τ_1, there is a bimodal distribution where 1.5 ns peak might relate to polymer chains in the water phase while 2.3 ns to 2.4 ns peak might represent polymer in-between CNC structures. The distribution for τ_2 centers at 3.5 ns, corresponding to polymer chains in confinement or restricted at the CNC interface due to interactions between polymer chains and CNC surfaces.

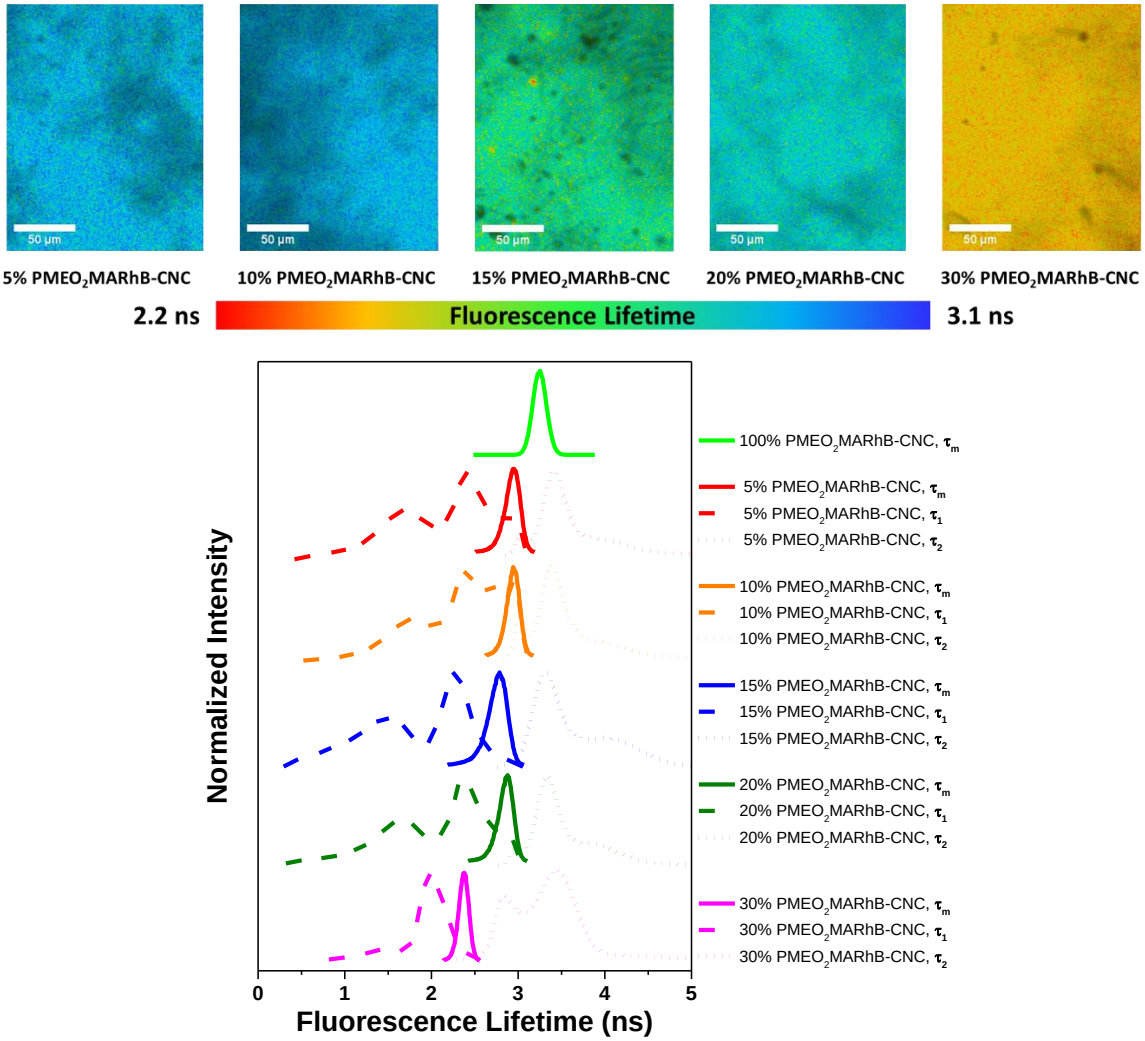

Figure 3.8. FLIM images of the $PMEO_2MARhB$-CNC series (top) were scaled on the sample color scheme for τ_m comparison within the sample. Normalized fluorescence lifetime for $PMEO_2MARhB$-CNC series (bottom) where solid lines represent the average fluorescence lifetime and the dashes and dots show τ_1 and τ_2 are short and long lifetimes, respectively.

Interestingly, pure $PMEO_2MARhB$ had the longest average fluorescence lifetime in comparison to the nanocomposite films. This observation indicates there are two opposing parameters that influence the fluorescence lifetimes: polymer confinement and water content. When polymer loading increases, polymer confinement decreases as the CNC structure is expanding, resulting in shorter fluorescence lifetimes. To further understand whether water content or confinement has a larger role in influencing the fluorescence lifetime, a dynamic study of 10 % $PMEO_2MARhB$-CNC was conducted. Water reversible absorption/desorption process was shown to expand/contract CNCs pitch by infiltrating the helical structure.[9] In the presence of water, fluorescence lifetime is shortened due to chain mobility and water is acting like a plasticizer. The lack of water would have the opposite effect and shift the fluorescence lifetime to a longer time. The 10 % $PMEO_2MARhB$-CNC sample was exposed to 95 % RH then FLIM acquisition took place as the water evaporated over time, **Figure 3.9**. When comparing the normalized fluorescence lifetime from 2.5 hours to 3 days after the film is removed from the humidified environment, there is a significant shift to longer lifetime for τ_1 than in τ_2. This supports the assignment of τ_1 peak between 0.5 ns to 1.5 ns where polymer chains are likely in the mobile water phase. The shift for τ_2 is less affected by the water evaporation since polymer confined at CNC interface is not exposed to water aside from the intrinsic water surrounding the CNC rods.

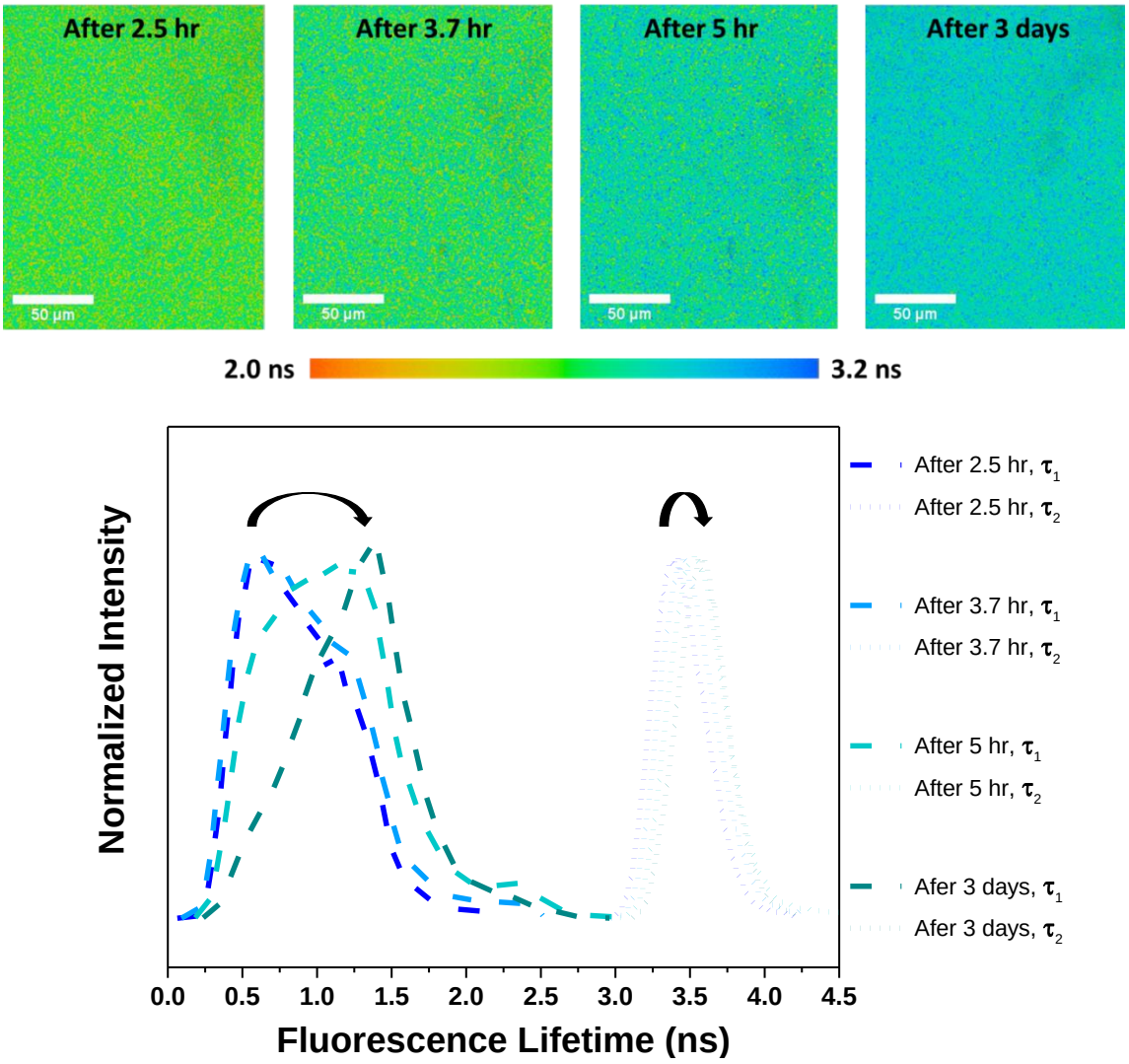

Figure 3.9. Normalized FLIM images and fluorescence lifetime of 10% PMEO$_2$MARhB-CNC after 2.5 hours to 3 days outside of 95% RH environment with τ_1 (dashes) and τ_2 (dots) are short and long lifetimes, respectively.

Thermogravimetric analysis was used to estimate water present in PMEO$_2$MARhB-CNC films at different humidities. The films were first equilibrated at 55% RH and 75% RH at 20 °C overnight. Based on the results, pure CNCs had the highest percent of water and the pure PMEO$_2$MARhB had the least at both relative humidities. This was expected due to CNCs hydrophilic nature. Even though PMEO$_2$MARhB is below its LCST (26 °C) at room temperature (21 °C) it does pick up 1% to 2% water but the polymer is still more

hydrophobic than CNCs. Water content is decreased with increase in polymer loading, explaining the longer fluorescence lifetime observed for $PMEO_2MARhB$ homopolymer in **Figure 3.10**. The measured water content for 10% $PMEO_2MARhB$-CNC decreased over time as the sample was allowed to re-equilibrate to ambient condition of 45% RH, aligning with the observed shift to longer fluorescence lifetime.

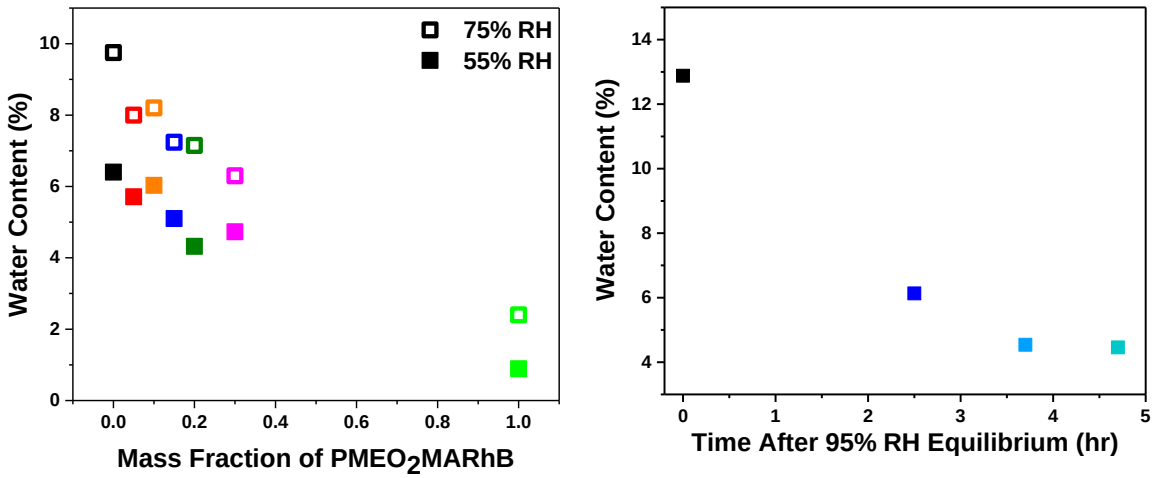

Figure 3.10. Water content for $PMEO_2MARhB$-CNC films at 55 % RH and 75 % RH (left). Water content for 10% $PMEO_2MARhB$-CNC that was allowed to equilibrate at 95 % RH overnight then allowed to re-equilibrate to ambient at 45 % RH (right).

The water measurements provided insights on how the opposing forces of polymer attraction to CNCs and water influenced the τ_1 and τ_2 that ultimately leads to τ_m. The shorter lifetimes (τ_1) indicated a more mobile environment with higher water content while the longer fluorescence lifetimes (τ_2) suggested a more restricted environment than $PMEO_2MARhB$ polymer matrix due to polymer attracted to the CNC interfaces. Together, the contribution of τ_1 and τ_2 are summarized in τ_m, showing an overall shift to shorter fluorescence lifetime with increasing polymer loading.

3.3.3. Probing Water and Polymer Chains Dynamics via Solid-State NMR

While FLIM provided information about polymer chain dynamics, the technique could not probe the dynamic of the water component. Hence, ^{1}H solid-state NMR was explored to examine both the water and polymer through variation of water content and temperature range. In general, the water signal is narrow in the CNCs nanocomposites and reveals that the water is separated from CNCs. The average separation distance between the CNCs and water domains is 10 nm. This demonstrated that the $PMEO_2MA$ has molecular-level miscibility with cellulose nanocrystals.

Pure CNCs and 20 % $PMEO_2MA$RhB-CNC were compared against each other. The water peak was targeted for the two samples at 50 % RH while being exposed to 2 °C to 50 °C, shown in **Figure 3.11.** With increasing temperature, the water peak sharpened and shifted upfield. The peak sharpening observation indicated the mobility of water while the shifting upfield translated to a reduction in hydrogen bonding. This is a common observation for water with increasing temperature.[13]

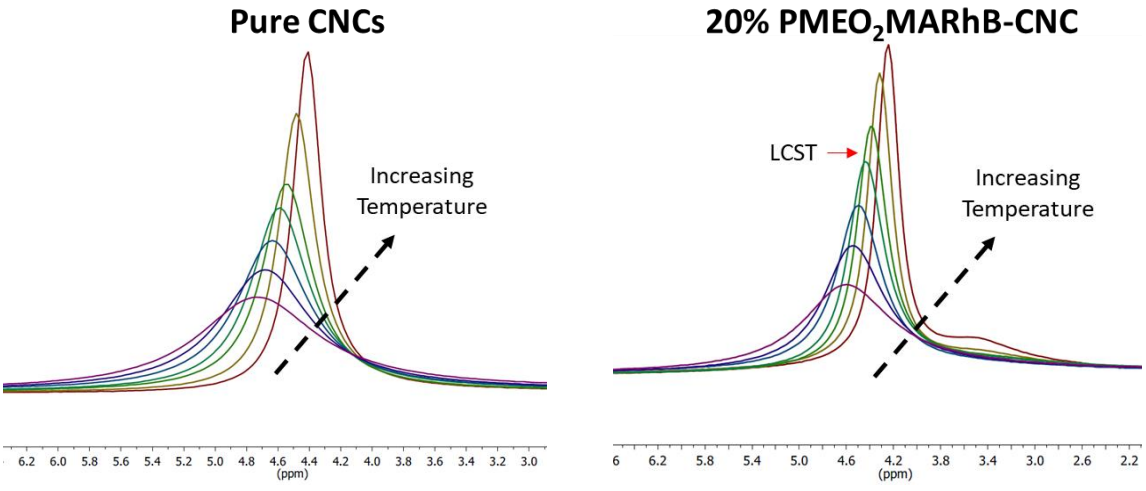

Figure 3.11. ^{1}H solid state NMR of water peak of pure CNCs (left) and 20 % $PMEO_2MA$RhB-CNC (right) through a series of temperature from 2 °C to 50 °C at 50 % RH (2.5 kHz spin rate).

Using the same samples, 25 mass % of water was added then exposed to the same temperature range, shown in **Figure 3.12.** Interestingly, the water peak increased in broadness for both pure CNCs and 20 % $PMEO_2MA$RhB-CNC, which was associated with a decrease in water dynamics in the system. The observation was counter-intuitive considering the peak sharpening should be prominent with more water present and indicated the CNCs component was contributing to the decreased mobility of water. As water was extracted from 20 % $PMEO_2MA$RhB-CNC in **Figure 3.12 C**, the water peak appeared to revert back to decreasing in broadness, revealing the reversibility of the process and how evaporation did not take place in the closed system.

The $PMEO_2MA$ mobility increased with high temperature and water content, counterintuitive to the observed LCST process where polymer peak should broaden with increasing temperature instead of becoming more prominent.[13–15] We hypothesized that in the closed system, the water was trapped and forced to interact with the polymer component, resulting in the water dynamics decreasing since it was in a more restricted environment. Solid-state NMR also revealed $PMEO_2MA$ segmental dynamic was slowed by CNCs with the polymer peak not noticeable in **Figure 3.11**. The observation corresponds to the longer fluorescence lifetime (τ_2) in $PMEO_2MA$RhB-CNC samples. The dynamics for these polymer chains could not be further extracted from solid-state NMR because the events happen faster than the microseconds regime.

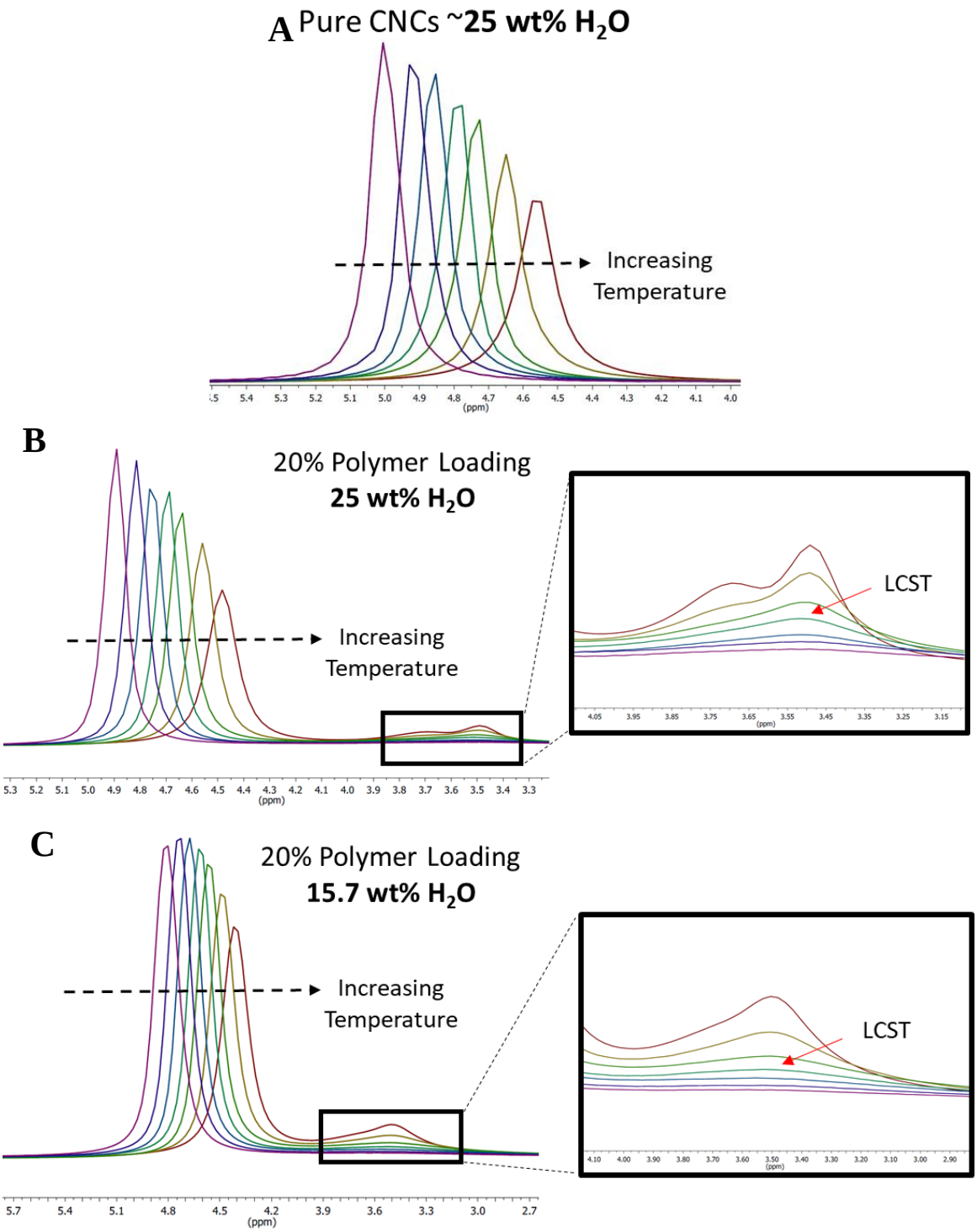

Figure 3.12. ^{1}H solid state NMR of water peak and polymer peak from 2 °C to 50 °C (2.5 kHz spin rate) where A) pure CNCs with 25 mass % water B) 20 % PMEO$_2$MARhB-CNC with 25 mass % water, and C) 20 % PMEO$_2$MARhB-CNC with 15.7 mass % water.

3.3.4. Polymer Dynamics Response to Temperature

Taking advantage of $PMEO_2MA$ thermoresponsive capability, FLIM was used to measure the polymer response in CNC nanocomposites and whether $PMEO_2MA$ component would expel water content. From Chapter 2, the dry $PMEO_2MA$-CNC films did not exhibit optical change at temperatures above its LCST except when at least 50 mass % of water was present. To examine the effects of temperature on polymer dynamics, the 10 % $PMEO_2MA$RhB-CNC sample was investigated under dry and wet conditions at 20 °C and 40 °C, shown in **Figure 3.13A**. First, the effect of temperature was accounted for by examining the sample in ambient (dry) conditions at 20 °C and 40 °C. The average fluorescence lifetime had a narrow distribution at around 3.1 ns. The 0.1 ns difference in lifetimes could be due to the $PMEO_2MA$RhB chains having more mobility at 40 °C.

To observe the phase transition, a sufficient amount of water was added to 10 % $PMEO_2MA$RhB-CNC sample and it was sealed with a cover slip to ensure water was not evaporating during acquisition. In the wet conditions at 20 °C, 40 °C, and cooled back to 20 °C, they all exhibited longer and broader distribution of fluorescence lifetimes, around 4.0 ns and 4.2 ns, comparing to the dry conditions. The broadness could be accounted for by the multiple environments the chains were experiencing. It is still unclear as why the fluorescence shifted to longer fluorescence besides the possibility that the polymer chains preferred to aggregate in the presence of water, as seen in the FLIM images where high fluorescence intensity was, which resulted in restricted mobility.

To have a better depiction of polymer dynamics, the FLIM images of the wet conditions were scaled to a color scheme ranged from 3.7 ns to 4.5 ns in **Figure 3.13B**. When 10 % $PMEO_2MA$RhB-CNC was exposed to 20 °C, the $PMEO_2MA$RhB chains were

highly fluorescent with longer fluorescence times than the surrounding regions shown in red. This revealed how the polymer did not prefer water even at temperature below LCST. The observation was more prominent at 40 °C where the highly fluorescent polymer regions shifted to longer lifetime (shown in blue) and the surrounding areas remained with shorter lifetime where water resided. The sample demonstrated the reversible thermoresponsiveness of the FLIM images and fluorescence distribution was similar to the initial 20 °C condition after it was cooled down to 20 °C. The results from the temperature experiments resembled work down by Okabe *et al.* where they observed labeled thermo-sensitive polymer chains having an increase in fluorescence intensity and longer fluorescence lifetime at elevated temperatures.[16]

In the presence of water, the $PMEO_2MARhB$ chains transitioned from hydrophilic coils to hydrophobic globules from 20 °C to 40 °C, respectively. The conformation change was observed by the shift to longer lifetime as the polymer chains became more restricted in the globular state. Despite the occurrence of the phase transition, the average fluorescence lifetime distribution for the wet conditions in **Figure 3.13A** showed a 0.2 ns difference at temperatures above and below LCST. This difference appeared insignificant and did not represent the change in polymer configuration because the fluorescence distribution took the average of the entire sample instead of the selected regions. Therefore, a closer analysis of selected regions with distinct features was performed for the wet condition experiments. At 20 °C, the highly fluorescent region (green) had a fluorescence lifetime around 4.1 ns while the mobile regions (red) had 3.8 ns lifetime, providing a 0.3 ns difference between the two extremes. At 40 °C, the highly fluorescent regions (blue) had an average of 4.5 ns lifetime while the surrounding shorter lifetime regions had around

3.8 ns. Comparing the highly fluorescent (polymer rich regions), there was a 0.4 ns to longer fluorescence lifetime at temperature below and above LCST that illustrated the chains transitioning from coil to globule. Meanwhile, the mobile areas (red) had similar lifetime of 3.8 ns, indicating how a portion of the water component was expelled from the polymer system. This demonstrated the concept of polymer resistant to water but there is work needed to be done on where the water goes and how it would affect the overall CNC nanocomposites.

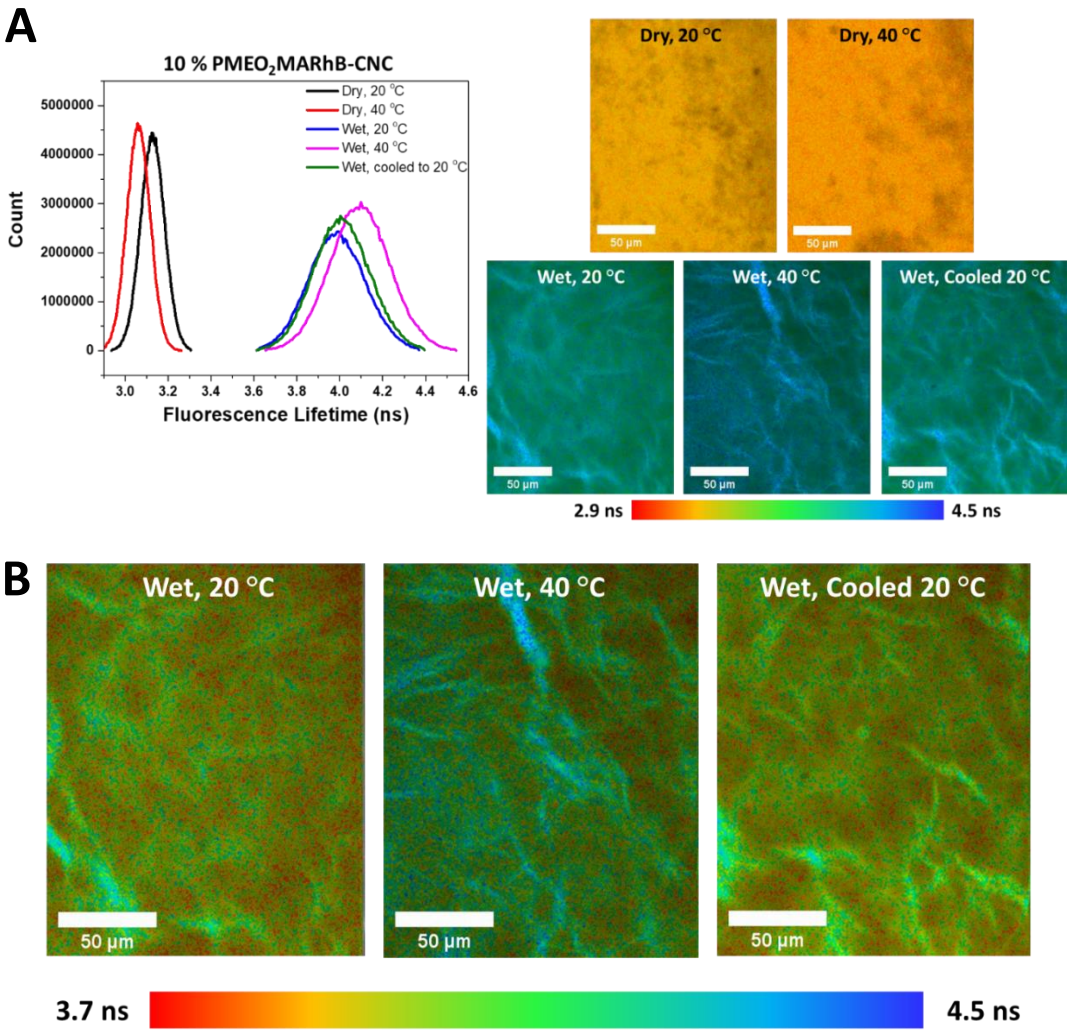

Figure 3.13. FLIM temperature study of 10% PMEO$_2$MARhB-CNC where A) fluorescence lifetime distribution and FLIM images with color scheme scaled to 2.9 ns to 4.5 ns of dry and wet conditions at 20 °C and 40 °C while B) only shows the wet conditions with a color scheme scaled to 3.7 ns to 4.5 ns to enhance contrast.

3.3.5. Mechanical and Morphology Characterization

To connect interfacial polymer dynamics to mechanical properties, DMA was used to measure in-plane uniaxial tensile properties of the nanocomposites, shown in **Figure 3.14**. Pure CNCs film has the highest strength with low strain of 0.3 % because of the high crystallinity content and the absence of energy-dissipating phase.[9] By blending $PMEO_2MARhB$ with CNCs, the low volume polymer phase acts as the energy-dissipating portion to suppress brittleness. At low polymer loadings of 5 % and 10 % $PMEO_2MARhB$, the tensile strength and modulus decreased by about 50 % comparing to pure CNCs. Polymer loadings above 10 mass % had similar strength and modulus while toughness and strain continued to improve. The mechanical properties of 30 % $PMEO_2MARhB$-CNC had a greater variation due to fracture mechanisms ranging from a brittle fracture to tearing.

The observation corresponds well with other reported CNC/hydrophilic polymer nanocomposites.[7,9,17,18] The polymer phase allows the resulting material to improve yielding and toughness but causes a drop in elastic modulus and tensile strength.[3,7] For the $PMEO_2MARhB$-CNC films, polymer confined at the CNC interfaces contributes to the mechanical performance by increasing stress transfer efficiency between CNCs and polymer.[19] However, additional polymer content has mobile dynamics that appears to have diluting and yielding effects, providing dissipative movement of CNC rods against each other that results in toughness.[7,20] Toughness and strain properties were inversely proportional to the average fluorescence lifetime, seen in **Figure 3.15.**

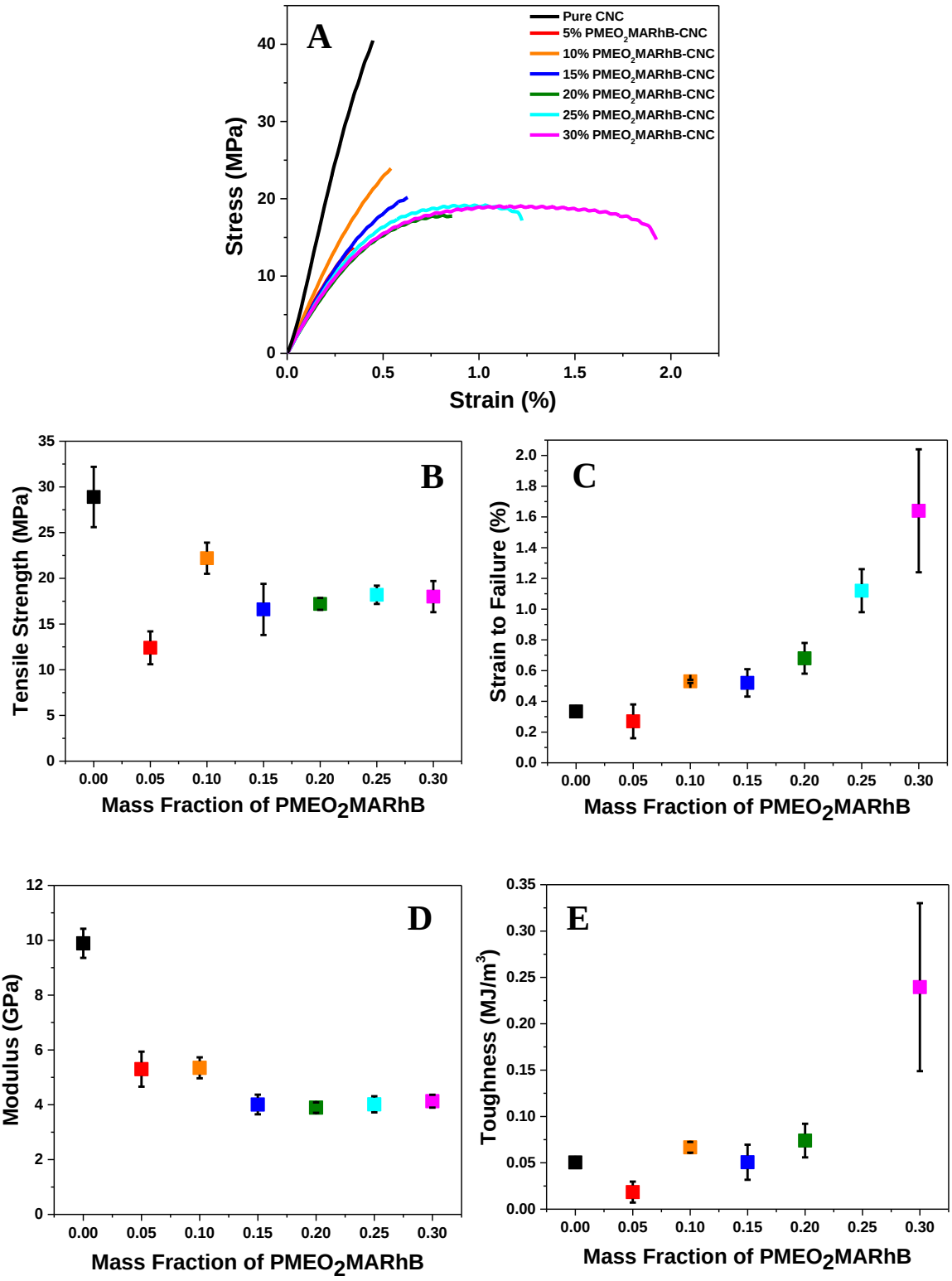

Figure 3.14. DMA curves for $PMEO_2MARhB$-CNC films where A) stress-strain curves, B) tensile strength, C) strain to failure, D) modulus, and E) toughness as a function of $PMEO_2MARhB$.

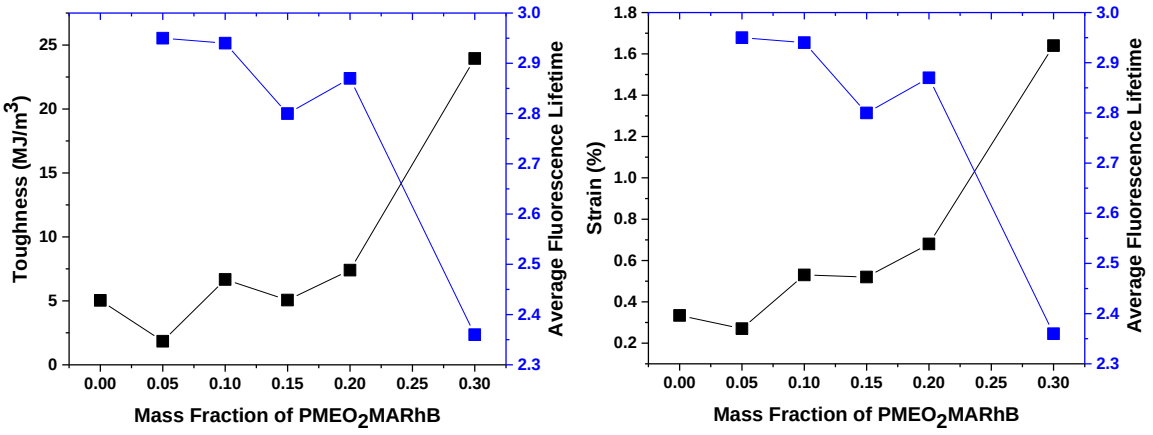

Figure 3.15. Toughness (left) and strain (right) plotted with average fluorescence lifetimes of various PMEO$_2$MARhB-CNC nanocomposites.

Similar to **Section 2.4**, phase images were taken by AFM to analyze the morphology of PMEO$_2$MARhB-CNC films top (sample-air interface) and bottom (sample-substrate interface) interfaces, shown in **Figure 3.16**. The bottom interface of 15% PMEO$_2$MARhB-CNC revealed structures that have distinct features that look like phase separation of the polymer from the CNCs. For 20% and 30% polymer loading, the bottom interfaces had a disordered structure that exhibit inhomogeneity. Phase separation can occur when unfavorable changes in entropy for the polymer to fill spaces between CNC structures is larger than entropy of mixing between the polymer system and the CNCs.[21] The AFM phase images showed the difference in morphology for various polymer loadings which results in variation of polymer confinement depending on which interface and sample depth that is being examined.

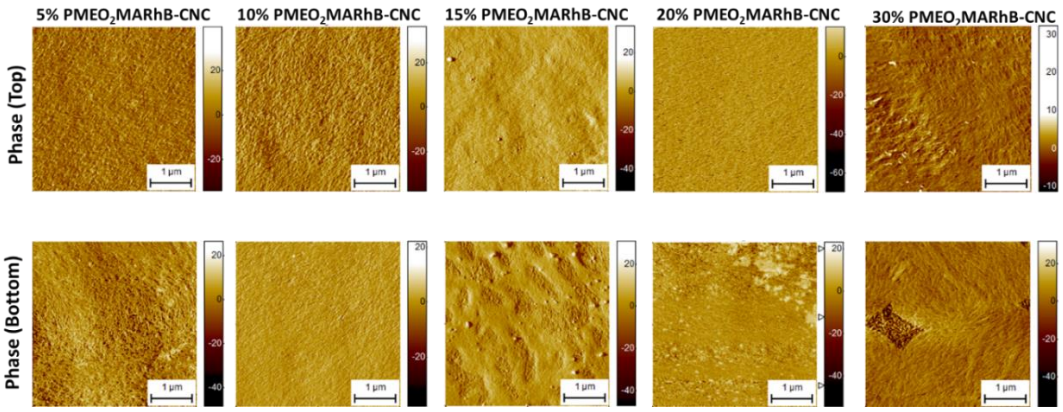

Figure 3.16. Phase AFM images for $PMEO_2MARhB$-CNC films. The top side of the CNC films (sample-air interface) are on top row and the bottom side of the films (sample-substrate interface) are on the bottom row.

3.3.6. Improving Polymer-CNC Interactions by Increasing Polymer Hydrophilicity

To increase polymer-CNC interactions, another LCST polymer system was adopted with a higher hydrophilicity compared to $PMEO_2MA$ called poly(oligo(ethylene glycol) methyl ether methacrylate) ($POEGMA_{300}$). The $POEGMA_{300}$ has a LCST of 64 °C because of the 4-5 repeating unit of PEO pendant group that makes it more hydrophilic, shown in **Figure 3.17**.[22] Their hydrophilic nature should be more compatible with CNCs, increasing the interactions between the two components due to hydrogen bonding that would result in better stress transfer.

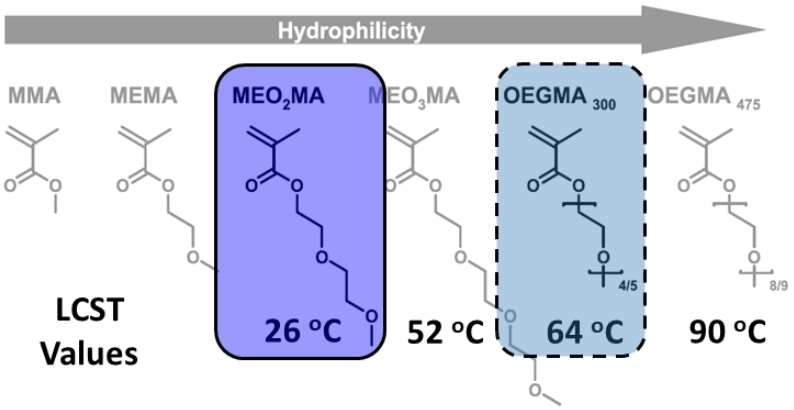

Figure 3.17. The structures of the oligo (ethylene oxide) methacrylate family and their corresponding polymers' LCSTs are listed below the monomer. Figure was modified from Ref. 22.

For some preliminary studies, the POEGMA chains were labelled with the same water-sensitive dye, yielding the resulting POEGMARhB with M_n = 12,300 g/mol and Đ = 1.2, **Figure 3.18**. The free-standing film of 15 % POEGMARhB-CNC was casted following the same procedure as mentioned in **Section 2.3**. Once the film was obtained, FLIM analysis revealed the average fluorescence lifetime to be around 3.1 ns, shown in **Figure 3.19**. The fluorescence lifetime for 15 % POEGMARhB-CNC was longer than the 15 % $PMEO_2MA$RhB-CNC with τ_m of 2.8 ns. When both POEGMARhB and $PMEO_2MA$RhB were compared, they had similar lifetime of 3.1 ns. This indicates that the POEGMARhB component in the 15 % sample had restricted mobility, which could be due to the attraction force between POEGMARhB and CNCs surfaces that caused the shift to longer fluorescence lifetime. For the 15 % $PMEO_2MA$RhB-CNC, the interaction with CNCs component might not be as strong and resulted in a shorter fluorescence lifetime due to more chain mobility.

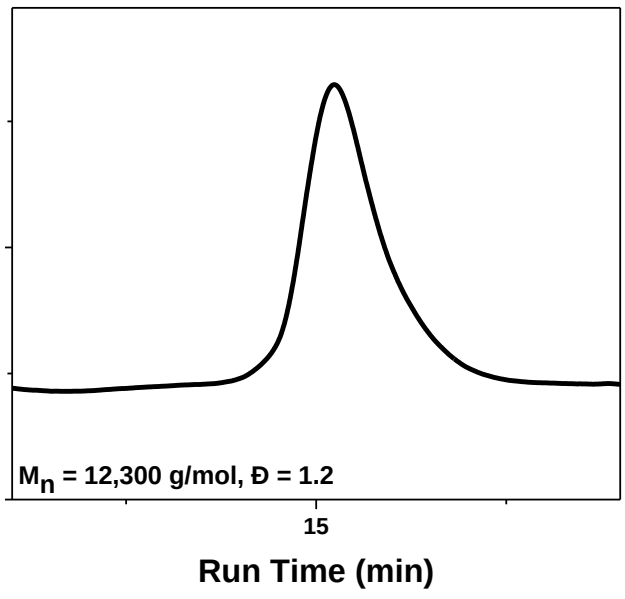

Figure 3.18. Molecular weight and dispersity of POEGMARhB polymer measured by DMF-GPC with PMMA standards.

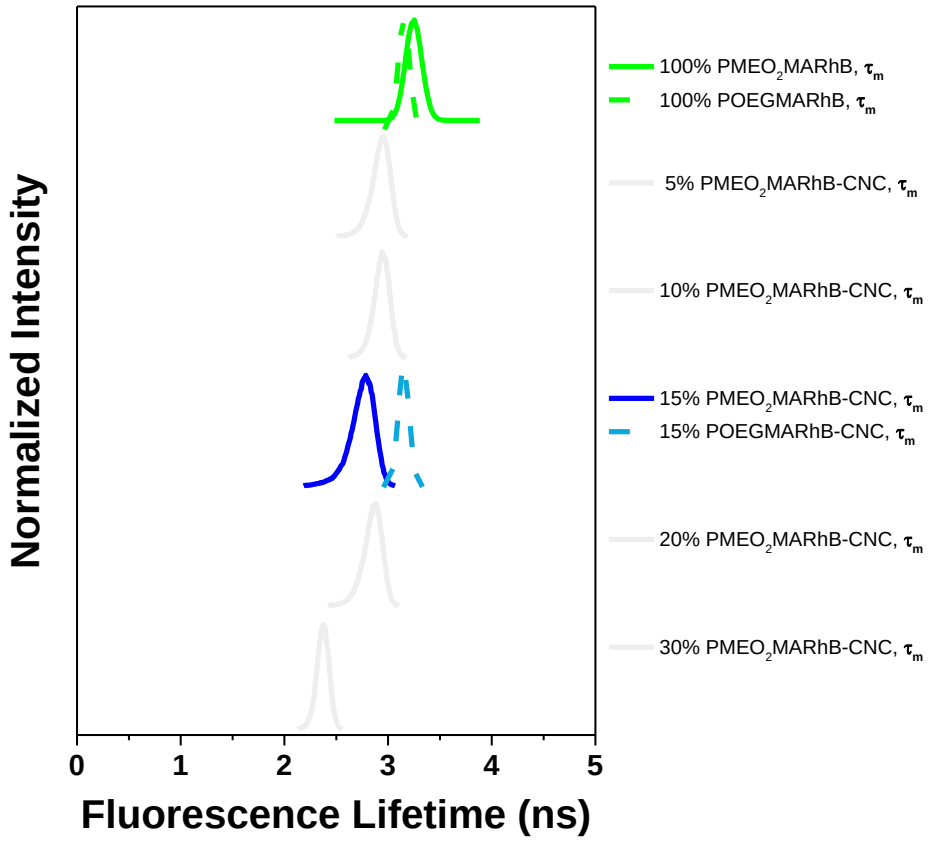

Figure 3.19. Comparison of fluorescence lifetimes between $PMEO_2MARhB$-CNC and POEGMARhB-CNC homopolymer and the 15 % polymer loadings.

To examine how the longer fluorescence lifetime in 15 % POEGMARhB-CNC translated to mechanical properties, the sample was analyzed via DMA with the same constant strain rate of 0.09 mm/min then compared to 15 % $PMEO_2MARhB$-CNC, **Figure 3.20**. Interestingly, there was an improvement in modulus and tensile strength with the POEGMARhB-CNC film. The observation indicated that POEGMARhB and CNCs have better stress transfer due to the increased interactions. Work done by Zhu *et al.* has shown the increase in hydrogen bonding in polymer systems leads to improved modulus for CNCs films.[23] However, the strain and toughness properties remained similar to the 15 % $PMEO_2MARhB$-CNC because the two systems should have the same amount of mobile polymer content that would aid in flexibility. The experiment provided insights on the

sensitivity of fluorescence lifetime measurements having the capability to track polymer interactions with CNCs component in the nanocomposites.

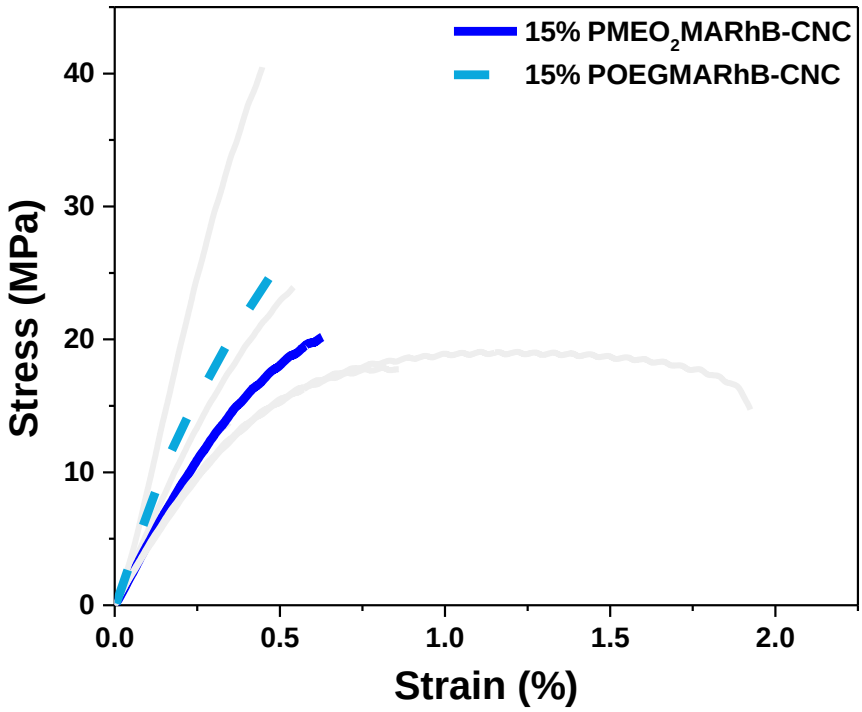

Figure 3.20. Comparison of stress-strain curves between 15 % $PMEO_2$MARhB-CNC and 15 % POEGMARhB-CNC.

3.4. Conclusions

These studies demonstrated FLIM as a method to investigate and visualize interfacial polymer nanosecond-dynamics in polymer-CNC nanocomposites. We observed three different environments that polymer chains were exposed to in the Bouligand structures. At ambient humidity, the shorter lifetimes (τ_1) are associated with more hydrated polymer domains while the longer fluorescence lifetimes (τ_2) are presumably associated with the polymer confined to the CNC interfaces. FLIM analysis was able to detect polymer conformation change as it underwent phase transition by increasing in fluorescence intensity and shift to longer fluorescence lifetime. There was a correlation

observed between fluorescence lifetime and mechanical properties, revealing polymer chains with high mobility aided in improvement in strain and toughness. When using POEGMARhB polymer system with higher hydrophilicity, there was a shift to longer lifetime and an improvement for modulus and tensile strength comparing to the corresponding $PMEO_2MARhB$-CNC film. From these studies, FLIM technique has demonstrated as a powerful methodology to examine composite systems. Future exploration could be pursued to combine FLIM acquisition with mechanical testing to visualize the polymer dynamics in real-time. Fundamental understanding of chain mobility will help us understand how polymer dynamics control material properties and provide insights into tuning nanocomposites.

3.5. References

(1) Seethamraju, S.; Obrzut, J.; Douglas, J. F.; Woodcock, J. W.; Gilman, J. W. Quantifying Fluorogenic Dye Hydration in an Epoxy Resin by Noncontact Microwave Dielectric Spectroscopy. *J. Phys. Chem. B* **2020**, *124* (14), 2914–2919. https://doi.org/10.1021/acs.jpcb.9b11622.

(2) Natarajan, B.; Emiroglu, C.; Obrzut, J.; Fox, D. M.; Pazmino, B.; Douglas, J. F.; Gilman, J. W. Dielectric Characterization of Confined Water in Chiral Cellulose Nanocrystal Films. *ACS Appl. Mater. Interfaces* **2017**, *9* (16), 14222–14231. https://doi.org/10.1021/acsami.7b01674.

(3) Natarajan, B.; Krishnamurthy, A.; Qin, X.; Emiroglu, C. D.; Forster, A.; Foster, E. J.; Weder, C.; Fox, D. M.; Keten, S.; Obrzut, J.; Gilman, J. W. Binary Cellulose Nanocrystal Blends for Bioinspired Damage Tolerant Photonic Films. *Adv. Funct. Mater.* **2018**, *28* (26), 1800032. https://doi.org/10.1002/adfm.201800032.

(4) Vargas, W.; Avendano, E.; Hernández-Jiménez, M.; Azofeifa, D.; Libby, E.; Solís, Á.; Barboza-Aguilar, C. Photonic Crystal Characterization of the Cuticles of Chrysina Chrysargyrea and Chrysina Optima Jewel Scarab Beetles. *Biomimetics* **2018**, *3* (4), 30. https://doi.org/10.3390/biomimetics3040030.

(5) Mitov, M. Cholesteric Liquid Crystals in Living Matter. *Soft Matter* **2017**, *13* (23), 4176–4209. https://doi.org/10.1039/c7sm00384f.

(6) Habibi, Y.; Lucia, L. A.; Rojas, O. J. Cellulose Nanocrystals: Chemistry, Self-Assembly, and Applications. *Chem. Rev.* **2010**, *110* (6), 3479–3500. https://doi.org/10.1021/cr900339w.

(7) Wang, B.; Walther, A. Self-Assembled, Iridescent, Crustacean-Mimetic Nanocomposites with Tailored Periodicity and Layered Cuticular Structure. *ACS Nano* **2015**, *9* (11), 10637–10646. https://doi.org/10.1021/acsnano.5b05074.

(8) Wan, H.; Li, X.; Zhang, L.; Li, X.; Liu, P.; Jiang, Z.; Yu, Z. Z. Rapidly Responsive and Flexible Chiral Nematic Cellulose Nanocrystal Composites as Multifunctional Rewritable Photonic Papers with Eco-Friendly Inks. *ACS Appl. Mater. Interfaces* **2018**, *10* (6), 5918–5925. https://doi.org/10.1021/acsami.7b19375.

(9) Yao, K.; Meng, Q.; Bulone, V.; Zhou, Q. Flexible and Responsive Chiral Nematic Cellulose Nanocrystal/Poly(Ethylene Glycol) Composite Films with Uniform and Tunable Structural Color. *Adv. Mater.* **2017**, *29* (28), 1–8. https://doi.org/10.1002/adma.201701323.

(10) Guidetti, G.; Atifi, S.; Vignolini, S.; Hamad, W. Y. Flexible Photonic Cellulose Nanocrystal Films. *Adv. Mater.* **2016**, *28* (45), 10042–10047. https://doi.org/10.1002/adma.201603386.

(11) Shundo, A.; Okada, Y.; Ito, F.; Tanaka, K. Fluorescence Behavior of Dyes in Thin Films of Various Polymers. *Macromolecules* **2012**, *45* (1), 329–335. https://doi.org/10.1021/ma201901x.

(12) Woodcock, J. W.; Beams, R.; Davis, C. S.; Chen, N.; Stranick, S. J.; Shah, D. U.; Vollrath, F.; Gilman, J. W. Observation of Interfacial Damage in a Silk-Epoxy Composite, Using a Simple Mechanoresponsive Fluorescent Probe. *Adv. Mater. Interfaces* **2017**, *4* (10), 1–5. https://doi.org/10.1002/admi.201601018.

(13) Zhang, C.; Peng, H.; Whittaker, A. K. NMR Investigation of Effect of Dissolved Salts on the Thermoresponsive Behavior of Oligo (Ethylene Glycol) - Methacrylate-Based Polymers. *J. Polym. Sci. Part A Polym. Chem.* **2014**, *52*, 2375–2385. https://doi.org/10.1002/pola.27252.

(14) Han, S.; Hagiwara, M.; Ishizone, T. Synthesis of Thermally Sensitive Water-Soluble Polymethacrylates by Living Anionic Polymerizations of Oligo (Ethylene Glycol) Methyl Ether Methacrylates. *Macromolecules* **2003**, *36* (22), 8312–8319. https://doi.org/10.1021/ma0347971.

(15) Weber, C.; Hoogenboom, R.; Schubert, U. S. Temperature Responsive Bio-Compatible Polymers Based on Poly(Ethylene Oxide) and Poly(2-Oxazoline)S. *Prog. Polym. Sci.* **2012**, *37* (5), 686–714. https://doi.org/10.1016/j.progpolymsci.2011.10.002.

(16) Okabe, K.; Inada, N.; Gota, C.; Harada, Y.; Funatsu, T.; Uchiyama, S. Intracellular Temperature Mapping with a Fluorescent Polymeric Thermometer and Fluorescence Lifetime Imaging Microscopy. *Nat. Commun.* **2012**, *3* (705), 1–9. https://doi.org/10.1038/ncomms1714.

(17) Vollick, B.; Kuo, P. Y.; Thérien-Aubin, H.; Yan, N.; Kumacheva, E. Composite Cholesteric Nanocellulose Films with Enhanced Mechanical Properties. *Chem. Mater.* **2017**, *29* (2), 789–795. https://doi.org/10.1021/acs.chemmater.6b04780.

(18) Tatsumi, M.; Teramoto, Y.; Nishio, Y. Polymer Composites Reinforced by Locking-in a Liquid-Crystalline Assembly of Cellulose Nanocrystallites. *Biomacromolecules* **2012**, *13* (5), 1584–1591. https://doi.org/10.1021/bm300310f.

(19) Hamad, W. Y. *Cellulose Nanocrystals: Properties, Production and Applications*; 2017. https://doi.org/10.1002/9781118675601.

(20) Bardet, R.; Belgacem, N.; Bras, J. Flexibility and Color Monitoring of Cellulose Nanocrystal Iridescent Solid Films Using Anionic or Neutral Polymers. *ACS Appl. Mater. Interfaces* **2015**, *7* (7), 4010–4018. https://doi.org/10.1021/am506786t.

(21) Natarajan, B.; Gilman, J. W. Bioinspired Bouligand Cellulose Nanocrystal Composites: A Review of Mechanical Properties. *Philos. Trans. A. Math. Phys. Eng. Sci.* **2018**, *376* (2112), 20170050. https://doi.org/10.1098/rsta.2017.0050.

(22) Lutz, J. F.; Hoth, A.; Schade, K. Design of Oligo(Ethylene Glycol)-Based Thermoresponsive Polymers: An Optimization Study. *Des. Monomers Polym.* **2009**, *12* (4), 343–353. https://doi.org/10.1163/156855509X448316.

(23) Zhu, B.; Merindol, R.; Benitez, A. J.; Wang, B.; Walther, A. Supramolecular Engineering of Hierarchically Self-Assembled, Bioinspired, Cholesteric Nanocomposites Formed by Cellulose Nanocrystals and Polymers. *ACS Appl. Mater. Interfaces* **2016**, *8*, 11031–11040. https://doi.org/10.1021/acsami.6b00410.

CHAPTER 4. DYNAMICS OF GRAFTED THERMORESPONSIVE POLYMERS ON CELLULOSE NANOCRYSTALS

4.1. Abstract

$PMEO_2MARhB$ chains were covalently bonded on CNCs surface and compared with the blended $PMEO_2MARhB$-CNC system to understand how restricting polymer chains will affect chain dynamics. Nanocomposite films containing 5% to 40 mass % of grafted $PMEO_2MARhB$ were prepared via *grafting-from* technique then films were cast under evaporation-induced self-assembly. FLIM was utilized to quantify the dynamics of the grafted chains by measuring the fluorescence lifetime of the water-sensitive dye attached on $PMEO_2MA$. In the blended $PMEO_2MARhB$-CNC system, the fraction of confined polymers at the CNCs interface decreases with increasing polymer loading, resulting in shorter fluorescence lifetimes. On the contrary, longer fluorescence lifetimes were observed for grafted $PMEO_2MARhB$-CNC due to polymer chains being restricted to the CNC rods' surface. Observation of transient polymer dynamics was performed by exposing the nanocomposite films to variations of relative humidity. Correlation between polymer dynamics and mechanical performances were observed and allowed for optimization of CNC nanocomposite films.

4.2. Experimental

Two common grafting approaches are "grafting-onto" and "grafting-from". As depicted in **Figure 4.1**, "grafting-onto" is when the polymer chain is synthesized with an appropriate functionality that will then attach to a surface, substrate, or another macromolecule. Through this technique, the molecular weight and dispersity of the polymer chains are known before coupling to the substrate. Since the chains tend to have

high molecular weight, steric hindrance generally leads to low grafting density. For the "grafting-from" technique, an initiator is attached to the surface, from this point of attachment, polymer chains can propagate outward from the substrate. This technique tends to yield higher grafting densities since steric hindrance is minimized. Unless the grafting-from chains can readily be cleaved, it is difficult to analyze the grafted polymer chain's molecular weight and dispersity.[1,2]

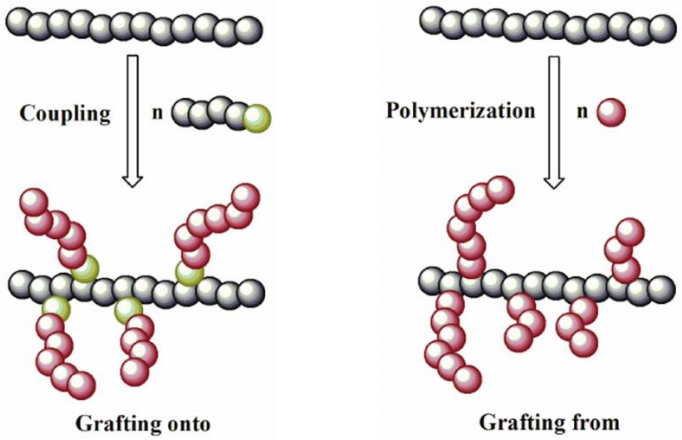

Figure 4.1. Schematic of "grafting-onto" and "grafting from" techniques. Image was from Ref. 1.

Based on the advantages mentioned, the "grafting-from" technique was chosen to graft $PMEO_2MA$ labelled with RhB-MMA to CNCs. This allowed higher grafting density to the CNCs surface while avoiding limitations of steric hindrance. ATRP was used to control the molecular weight as well as dispersity, the synthesis schematic is shown in **Figure 4.2**.

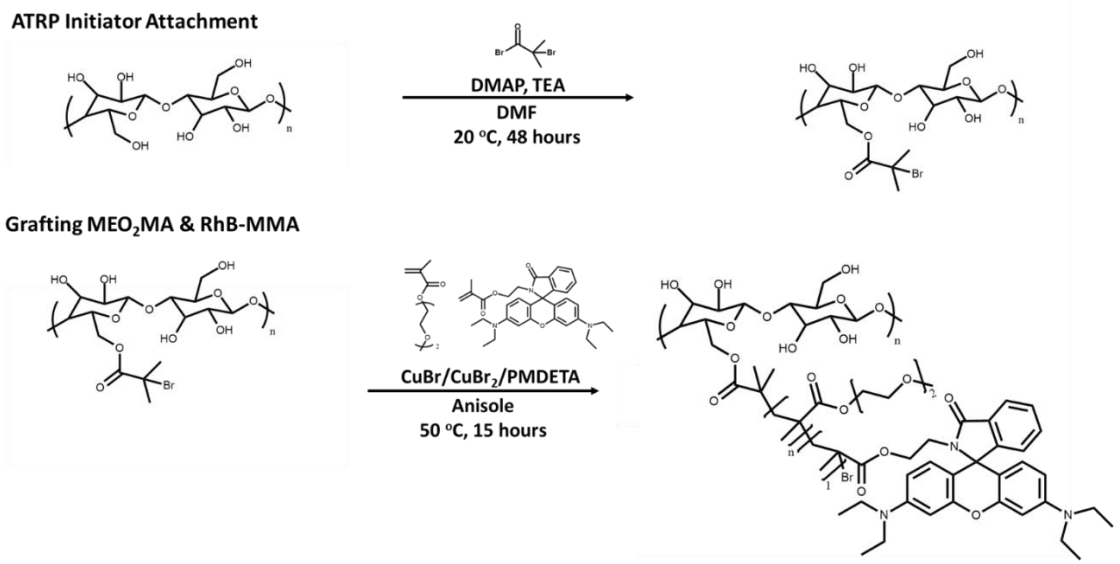

Figure 4.2. Synthesis scheme for "grafting-from" technique to synthesize CNC-*g*-PMEO$_2$MARhB.

4.2.1. Materials

12.1 mass % of sodium-neutralized sulfated wood cellulose nanocrystals (Na-CNCs) by mass in aqueous suspensions were obtained from the University of Maine Process Development Center. Di(ethylene glycol) methyl ether methacrylate (MEO_2MA, 95 %), copper (I) bromide (CuBr, 99.999 %), α-bromoisobutyryl bromide (BiB, 98 %) N,N,N',N'',N''-pentamethyldiethylenetriamine (PMDETA, 99 %), 4-(dimethylamino) pyridine (DMAP, ≥ 99 %), rhodamine B (RhB, ≥ 95 %), ethanolamine (≥ 95 %), methacryloyl chloride (97 %), anisole, anhydrous (99.7 %) were purchased from Sigma-Aldrich. Hexanes (95 %) dichloromethane (DCM), acetone, ethyl alcohol (EtOH, 200 proof), methanol (MeOH) were purchased from Fisher Scientific. N,N-dimethylformamide, anhydrous AcroSeal (DMF, 99 %), Copper (II) bromide ($CuBr_2$, 99 %) and triethylamine (TEA, 99 %) were purchased from Alfa Aesar. The chemicals were used as received.

4.2.2. Preparation of CNCs and Attachment of Initiator

A 12.1 mass % cellulose nanocrystals in water was obtained from the University of Maine. Roughly 2 g of dry CNCs mass was measured and diluted with DI water to 7 mass %. The diluted CNCs solution was solvent exchanged with acetone five times by forming a suspension, centrifuging, decanting excess solvent mixture of water and acetone. This removed a majority of the water content without "drying" the CNCs. Dried CNCs form irreversible aggregates that would limit solubility and accessible surface area for further functionalization.

In a 500 mL round-bottomed flask, 4-(dimethylamino) pyridine (DMAP 0.8 g, 7 mmol) was added. The CNC-acetone suspension was then added to the flask along with anhydrous DMF (~70 mL) and stirred under nitrogen. Once a clear solution was obtained, triethylamine (TEA 15 mL, 110 mmol) was added with stirring for 30 minutes. Dropwise addition of 2-bromoisobutyryl bromide (BiB 9 mL, 74 mmol) was followed by placing the reaction in an oil bath at 30 ^{o}C for at least 48 hours. The CNC-BiB suspension was isolated by centrifuging and decanting with ethanol four times, and with methanol two times to remove unreacted reagents.

4.2.3. Grafting MEO_2MA and RhB-MMA

The CNC-BiB in methanol was solvent exchanged with anisole by doing one cycle of centrifuging and decanting. The CNC-BiB anisole suspension (~0.1 g of dry CNC-BiB) was placed in a 20 mL reaction vial with $CuBr_2$ (0.004 g, 0.017 mmol) and CuBr (0.028 g, 0.195 mmol) before closing the vial to purge with nitrogen. Anisole (5 mL) and PMDETA (0.05 mL, 0.24 mmol) were added and stirred for 10 minutes. In the dark, MEO_2MA (0.9 mL, 5 mmol) and RhB-MMA (0.01g, 0.02 mmol) were added to the reaction vial and the

reaction was conducted for 15 hours at 70 °C. The suspension was washed with ethanol and DI water by the centrifuging and decanting method to obtain CNC-*g*-$PMEO_2MARhB$.

4.2.4. Film Preparation for CNC-*g*-$PMEO_2MARhB$

An aqueous suspension of 12.1 mass % Na-CNCs was diluted to 2 mass % with DI water and sonicated for 45 minutes. The CNC-*g*-$PMEO_2MARhB$ (74.4 % grafted polymer) was dispersed in DMF and vortexed, followed by sonication for 45 minutes in an ice-filled bath to maintain the temperature below the LCST. The CNCs and $PMEO_2MARhB$ dispersions were mixed together at respective quantities and sonicated in the ice-filled bath (45 minutes) to cast cholesteric films of varying CNC-*g*-$PMEO_2MARhB$ mass fractions. Each prepared CNC-*g*-$PMEO_2MARhB$-CNC mixture ([5, 10, 15, 40] mass % CNC-*g*-$PMEO_2MARhB$) was poured into polystyrene petri-dish (diameter = 50 mm), which was placed in the hood to dry. The films were formed via evaporation-induced self-assembly with an average drying rate of -2 mg min^{-1}. The casting duration lasted until the film's mass remained constant.

4.3. Results and Discussions

4.3.1. Chemical Characterization of CNC-*g*-$PMEO_2MA$

After multiple CNCs modifications, FT-IR and TGA were utilized to estimate the amount of polymer being grafted on CNCs surface. The FT-IR spectra for pure CNCs, CNC-BiB, and grafted CNCs are compared in **Figure 4.3**. Tracking the intensity of the carbonyl band (1723 cm^{-1}) indicated the attachment of the initiator and the grafting of $PMEO_2MA$ and $PMEO_2MARhB$. Pure CNCs did not have any carbonyl group present so the presence of a carbonyl peak in CNC-BiB sample meant only a fraction of the hydroxyl

groups on CNCs were attached with the 2-bromoisobutyryl bromide initiator. The carbonyl peak increased significantly in the grafted CNCs with $PMEO_2MA$ and $PMEO_2MARhB$ samples due to the carbonyl group in MEO_2MA monomer.

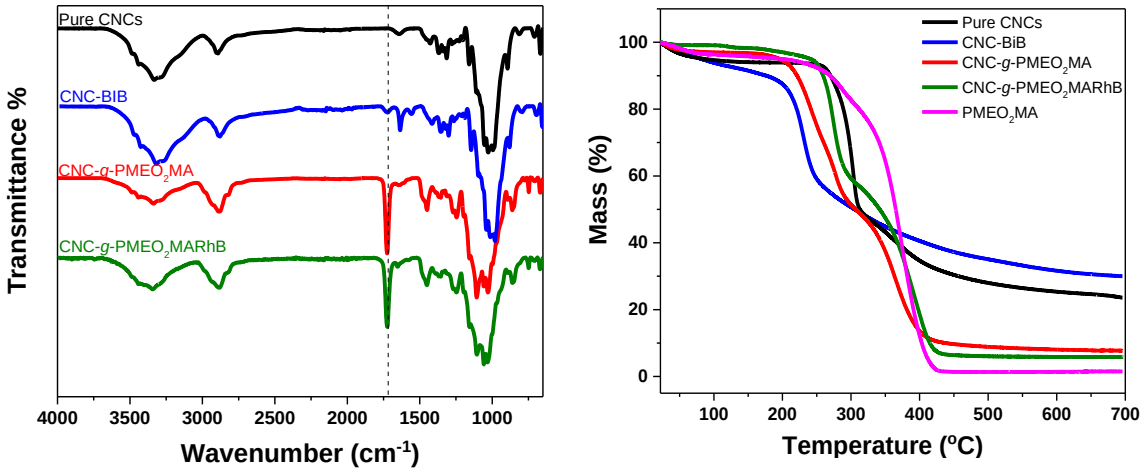

Figure 4.3. FTIR spectra for pure CNCs, CNC-BiB, and grafted CNCs (left) and TGA curves (right).

TGA of the grafted samples was acquired as a complimentary technique to determine the quantity of grafted $PMEO_2MARhB$ based on mass loss. After repeated washing with ethanol and water to remove any unattached polymer, TGA was conducted for pure CNCs, CNC-BiB, CNC-*g*-$PMEO_2MARhB$, and $PMEO_2MA$ homopolymer, shown in **Figure 4.3**. Pure CNCs began to degrade around 280 °C while CNC-BiB degraded closer to 200 °C. This shift in degradation suggested the attachment of the initiator. $PMEO_2MA$ homopolymer has the highest thermal stability, therefore, grafted CNCs were more thermal stable than CNC-BiB. The difference in thermal properties showed that the CNCs were functionalized with the initiator and $PMEO_2MA$ and $PMEO_2MARhB$.

The first derivative of mass loss curves provided an estimate of grafting ratio between $PMEO_2MARhB$ and CNCs. In **Figure 4.4**, the left plot showed the thermal curves for CNC-*g*-$PMEO_2MARhB$ at different polymer loadings. On the right plot, the first derivative

of the thermal curves revealed two peaks. The first peak (250-300 °C) and the second peak (300-450 °C) indicated the degradation of CNCs and $PMEO_2MARhB$, respectively. With the two distinct degradation peaks, the grafting ratio was calculated by integrating the two areas and using the equation below to obtain the estimated polymer grafted on CNCs (**Table 4.1**). For the derivative mass curve of CNC-*g*-$PMEO_2MARhB$ (74 mass %), there is another peak present around 200 °C that could be the degradation of CNC-BiB that did not have grafted $PMEO_2MARhB$ or excess solvent. Various grafting ratios of the polymer could be obtained by tuning the MEO_2MA feed. The CNC-*g*-$PMEO_2MARhB$ (74 mass %) sample was chosen to cast nanocomposite films with CNCs.

$$\boldsymbol{Grafting\ Ratio} = \frac{\boldsymbol{Area\ of\ PMEO_2MA\ degration\ peak}}{\boldsymbol{Area\ of\ CNCs\ degradation\ peak}}$$

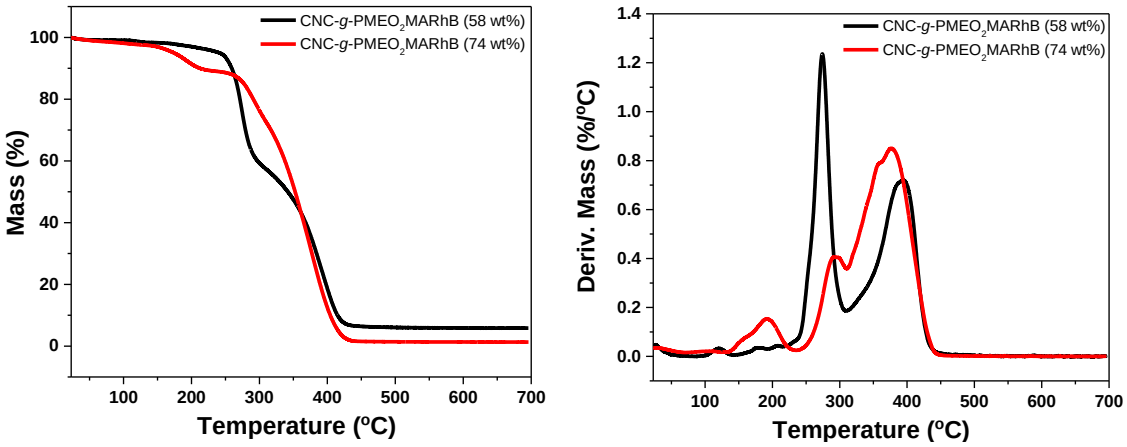

Figure 4.4. TGA curves for grafted CNCs with $PMEO_2MARhB$ at different polymer loading. The left plot shows the thermal curve from 22 °C to 700 °C while the right plot shows the first derivative of the thermal curves.

Table 4.1. Summary of the polymer loading of CNC-*g*-$PMEO_2MARhB$ from TGA data

Sample	g $PMEO_2MA$/ g CNCs	Mass % of $PMEO_2MA$
CNC-*g*-$PMEO_2MARhB$ (58 mass %)	1.39	58.2 %
CNC-*g*-$PMEO_2MARhB$ (74 mass %)	2.91	74.4 %

4.3.2. Optical and Structural Characterization of CNC-*g*-PMEO2MA Films

Optical properties of grafted-CNC films were examined via POM images for samples with and without extensive sonication. The casted films without sonication **Figure 4.5 (top)** had the same blue reflected color despite the various grafted-CNC loadings. The casted 30 % Grafted-CNC film exhibited heterogeneity where a section of the film had cholesteric structure and the other region was opaque (phase). This indicated that the opaque region was composed mostly of CNC-*g*-PMEO$_2$MARhB. To ensure the grafted-CNCs were well-mixed with pristine CNCs, the two solutions were sonicated for 1.5 hour and cast, POM images shown in **Figure 4.5 (bottom)**. There was a transition in color from blue to yellow-green going from 5 % to 15 % Grafted-CNC, respectively. For the 40 % Grafted-CNC sample, the film had an opaque appearance and POM image indicated some cholesteric structures. Based on the different reflected colors, it revealed that sonication is a crucial step to ensure the grafted-CNC is well incorporated within CNCs structures. The POM images were similar to blended polymer-CNC films from Chapter 2 and 3.

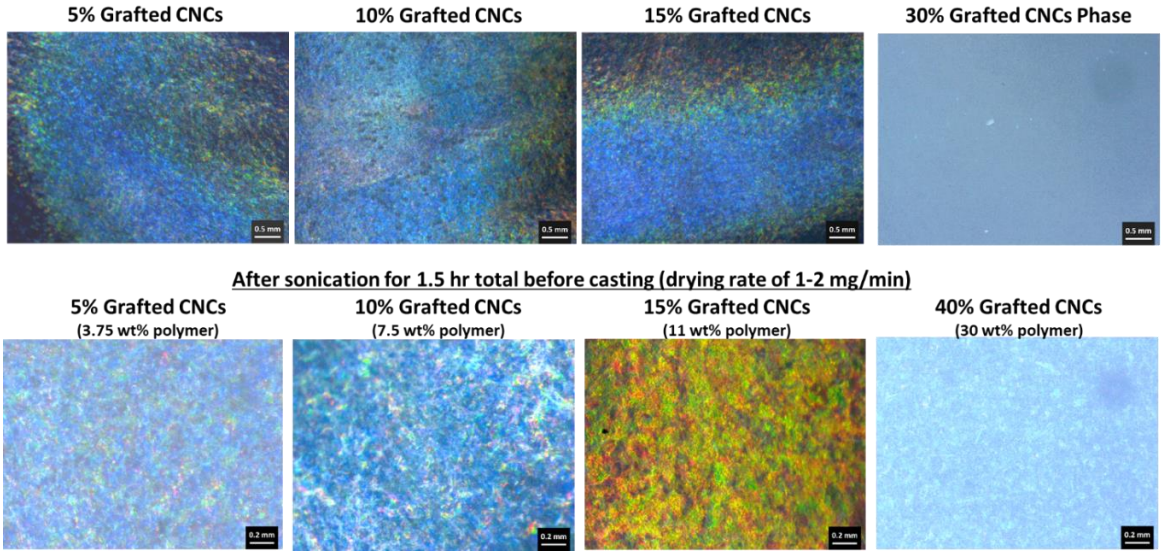

Figure 4.5. POM images of casted grafted CNC films without sonication (top) and with 1.5 hour of sonication (bottom) before casting the films.

Cross-sectional SEM images of the fractured films were taken for both the grafted-CNC film series to measure the films' thickness and pitch at multiple locations, **Table 4.2**. The grafted-CNC films were self-assembled into the Bouligand structures through the exhibition of the layered ordering. This has been observed in other grafted-CNC systems that were cast from aqueous solution.[3] For the series without sonication, there were polymer-rich regions and polymer aggregates, shown in **Figure 4.6 (top)**. These observations were not seen in the sonicated grafted-CNC films. The films were relatively homogenous with ordering layers even at the highest grafted-CNCs loadings. The 40 % Grafted-CNC sample did not have prominent CNC layers compared to the lower grafted-CNC loadings. The CNCs pitch is not well ordered or defined, hence the film lacked the vibrant reflected colors. When comparing the pitch measurements in **Table 4.2**, an increase in pitch was observed for the sonicated series as more CNC-*g*-PMEO$_2$MARhB was incorporated but not for the non-sonicated series. This further demonstrated how the CNC-*g*-PMEO$_2$MARhB were not distributed homogeneously throughout the films.

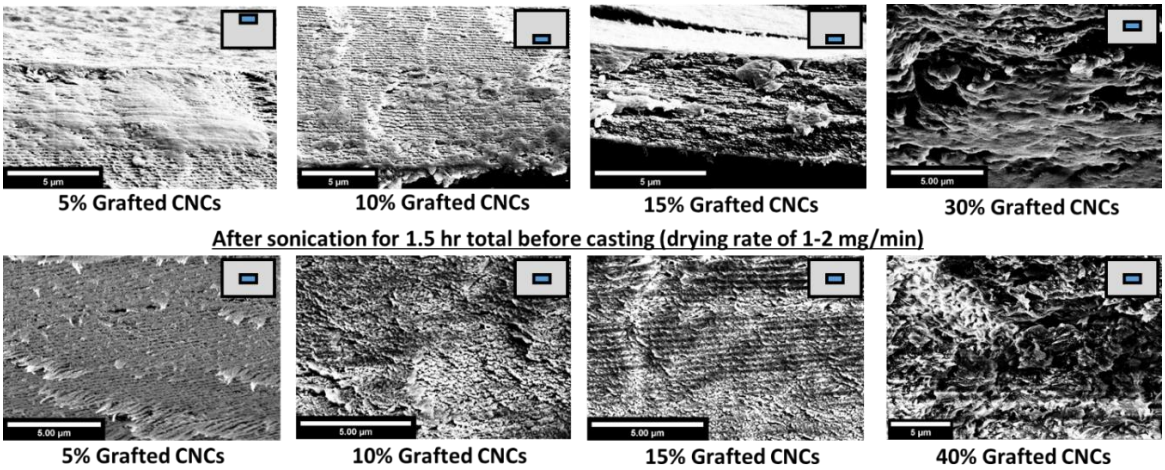

Figure 4.6. Cross-sectional SEM of the grafted CNC films without sonication (top) and with 1.5 hour of sonication (bottom) before film casting process.

Table 4.2. Summary of the grafted CNC films' thickness and pitch

	5% Grafted CNCs		10% Grafted CNCs		15% Grafted CNCs	
	Thickness (µm)	**Pitch (µm)**	**Thickness (µm)**	**Pitch (µm)**	**Thickness (µm)**	**Pitch (µm)**
No Sonication	67 ± 1.6	0.31 ± 0.05	26 ± 3.1	0.34 ± 0.05	55 ± 9.4	0.21 ± 0.03
Sonication	59 ± 0.64	0.32 ± 0.03	85 ± 0.48	0.35 ± 0.05	69 ± 1.2	0.44 ± 0.11

The pitch was further quantified by measuring the reflectance wavelength, shown in **Figure 4.7**. At ambient conditions (45-50 % RH), the reflectance peak shifted to higher wavelengths with the grafted-CNC loadings, going from 448 nm $\pm$ 32 nm to 585 nm $\pm$ 31 nm for the 5 % and 15 % Grafted-CNC samples, respectively. The reflectance peaks further shifted 140 nm to 185 nm to longer wavelengths when exposed to 95 % RH. The full-width at half height also increased when the samples were in higher relative humidity, going from 575 nm $\pm$ 45 nm to 770 nm $\pm$ 49 nm for the 5 % and 15 % Grafted-CNC. These observations were similar to the blended $PMEO_2MA$-CNC films shown in **Figure 2.7** where the reflectance for pure CNCs aligned with 5 % Grafted-CNC (3.75 mass % $PMEO_2MARhB$), 5% $PMEO_2MA$-CNC corresponded to 10 % Grafted-CNC (7.5 mass %), and 10 % $PMEO_2MA$-CNC to 15 % Grafted-CNC sample (11 mass %).

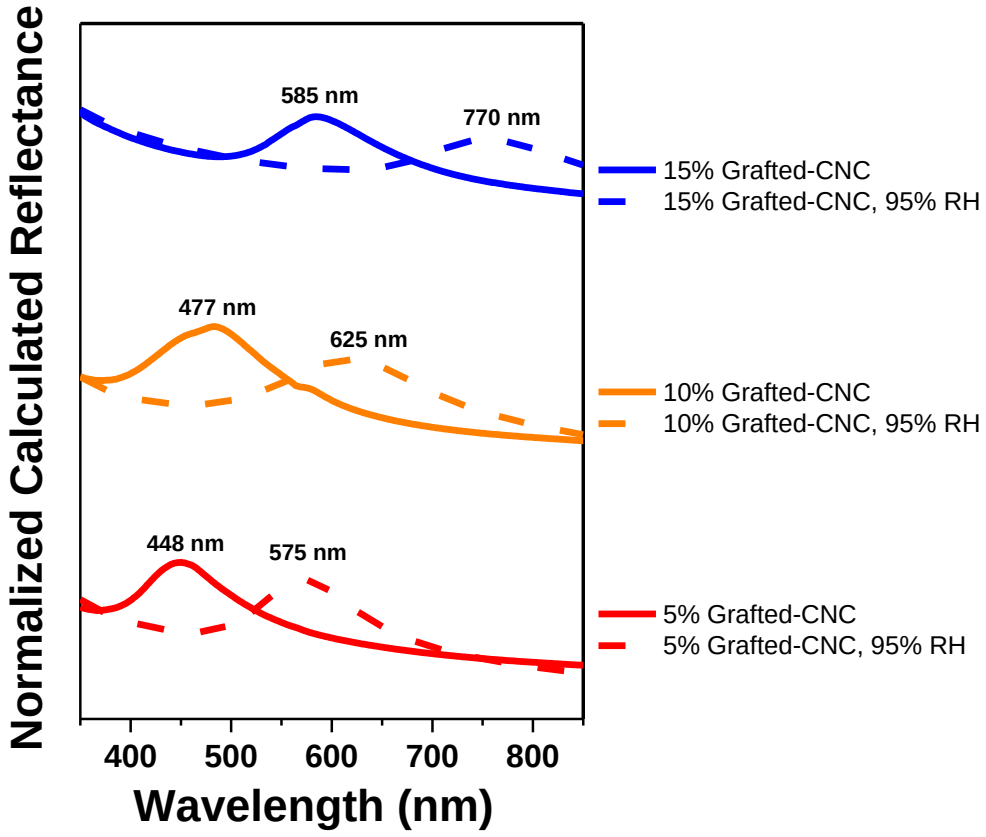

Figure 4.7. UV-vis spectra of the CNC films at 55 % and 95 % RH. When the samples are hydrated for at least 3 days, the wavelength shows an increase of about 130 nm – 185 nm with increasing difference correlating with grafted CNC loadings.

In terms of the water adsorption at 45 % RH and 95 % RH, the grafted-CNC films, in **Figure 4.8**, had similar trend as the blended system (**Figure 2.8**). All samples adsorbed more water at 95 % RH than 45 % RH and samples with higher CNCs content retaining water content. This observation is due to CNCs hydrophilic nature and the polymer not being as hydrophilic at temperatures close to its LCST. The 40 % Grafted-CNC behaved similar to the $PMEO_2MA$ homopolymer by having a difference of 3 mass % water.

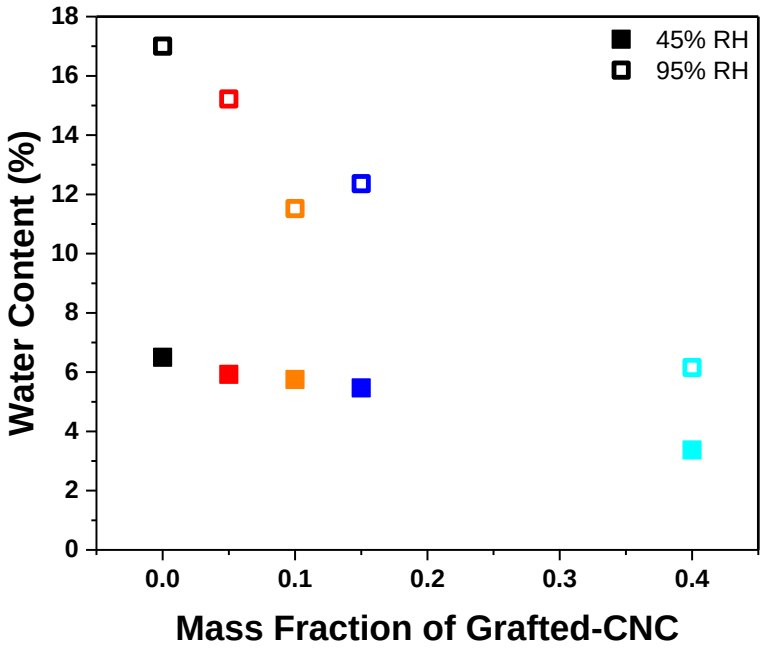

Figure 4.8. Comparison of water content for pure CNCs, 5 % to 40 % CNC-*g*-PMEO$_2$MARhB at 45 % RH and 95 % RH.

To observe the thermoresponsive behavior of PMEO$_2$MA, the procedure in section 2.3.2. was followed. In **Figure 4.9**, the 5 % and 18 % Grafted-CNC samples were soaked with water and exposed to 0 °C to 50 °C but they did not show significant optical changes within this temperature range. The observation differed from the blended PMEO$_2$MA-CNC films where the phase transition was apparent, going from clear to opaque with increasing temperature. In literature that studied LCST polymers, poly(N-isopropylacrylamide), poly(oligoethylene glycol methacrylate), and Jeffermine® polyetheramine, being grafted on CNCs, the grafted materials underwent phase transition in aqueous solutions similar to their homopolymer counterpart.[4–10] To explore why the grafted-CNC films were not responsive to temperature, the grafted-CNC film was added to a solution of water and sonicated in an ice bath to break up any aggregates that prevented phase transition. Unfortunately, those experiments were not successful in having the grafted-CNC films being optically responsive to changes in temperature. Dynamic light scattering could be

implemented to observe the difference in particle sizes for the blended and grafted-CNC systems and determine whether phase transition might be occurring that could not be detected optically.

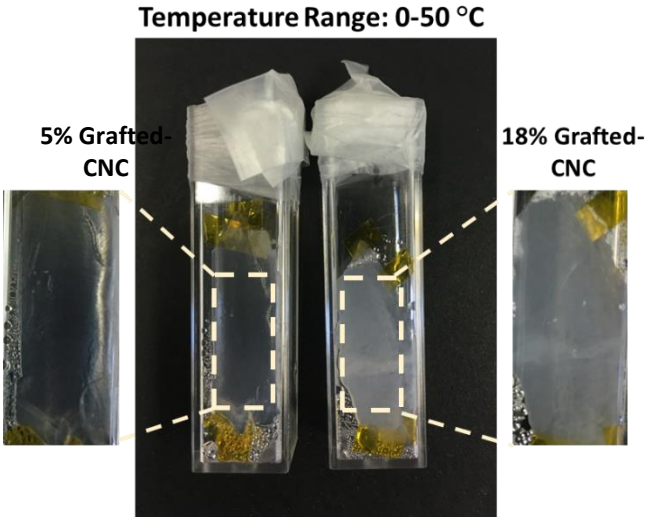

Figure 4.9. Images of 5 % and 18 % CNC-*g*-PMEO$_2$MA films after being exposed to 0 °C to 50 °C without significant change in optical properties.

4.3.3. Fluorescence lifetime imaging microscopy of CNC-*g*-PMEO2MA Films

Based on work done by Woodcock *et al.*, they observed a difference in shift and distribution of fluorescence lifetime between physically absorbed and covalently bonded mechanophores to silk fibers, shown in **Figure 4.10**. The physically adsorbed dye had a shorter lifetime and broader distribution than the covalently bonded dye. The longer lifetime was due to the dye being restricted and bounded to the surface of the silk fiber, having lower mobility to undergo fluorescence relaxation processes.[11] We hypothesized the grafted polymers would have a similar observation when compared to the blended PMEO$_2$MARhB-CNC in Chapter 3.

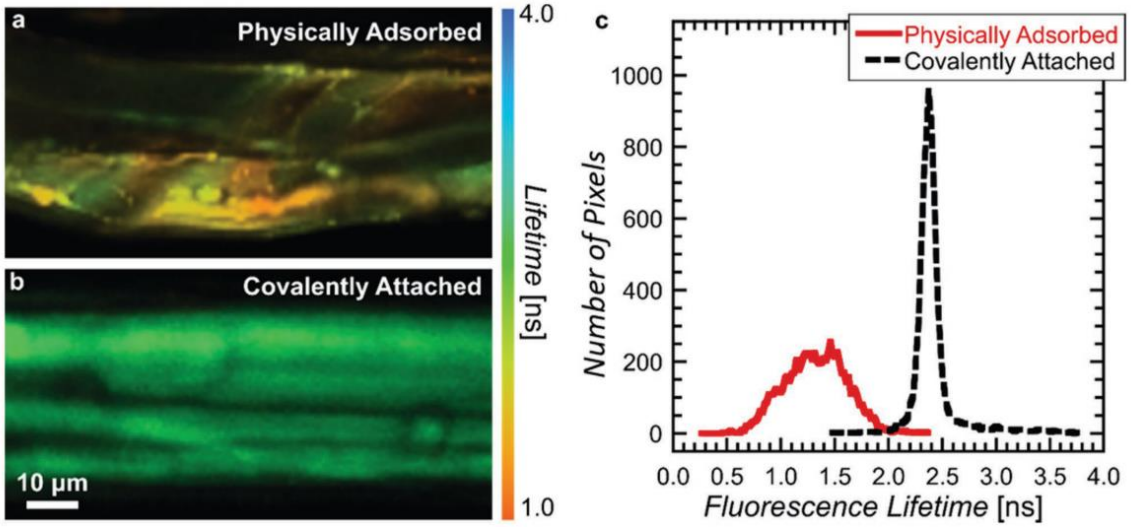

Figure 4.10. Two-photon-FLIM of a) physically absorbed and covalently attached mechanophores to silk fiber lifetime distributions. The covalently attached dye has a narrow and longer lifetime distribution than the physically absorbed dye. Data was taken from Ref. 11.

FLIM images revealed the distribution of lifetimes in the grafted-CNC films, **Figure 4.11 (top)**, with the images scaled to the same color scheme. Despite extensive sonication, the grafted-CNC films exhibited more heterogeneity than blended $PMEO_2MARhB$-CNC. The 5 % Grafted-CNC sample revealed shorter lifetimes while 100% CNC-*g*-$PMEO_2MARhB$ had mainly longer lifetimes. From 10 % to 40 % Grafted-CNC, they were in the middle of the spectrum with lifetime around 3.1 ns. Since $PMEO_2MARhB$ chains were anchored to the surface of CNCs, the fluorescence lifetime did not vary greatly being around 2.9 ns to 3.1 ns. Despite more polymer content present, confinement was the dominating factor that influenced chain mobility. The observation aligned with the P2VP/SiO_2 matrix-free polymer nanocomposites work done by Holt *et al.* where they examined the influence of grafted polymer chains molecular weight on segmental dynamics.[12] At lower M_w, the grafted chains have slower dynamics comparing to bulk polymer at the same M_w. The difference in dynamics decreased at higher M_w grafted

chains and they exhibited similar dynamics to bulk polymer since interfacial effects were not prominent when most polymer segments were far from the nanoparticles surface.[12] Therefore, the fluorescence lifetime between grafted $PMEO_2MARhB$ and $PMEO_2MARhB$ homopolymer were similar due to the high molecular weight of the grafted polymer.

A single exponential was sufficient to fit the decay curves for Grafted-CNC samples in contrary to the two-component needed for the blended polymer system. The grafted polymer had longer lifetimes than the physically adsorbed polymer chains with the difference between the two system being more prominent with increasing polymer loadings, show in **Figure 4.11 (bottom)**. The observation revealed that not all polymer chains in the blended system were physically adsorbed to the CNCs surface. At high polymer content, the unbounded polymers with high mobility have shortened average fluorescence lifetime. Other investigators have also seen slower dynamics for covalently bonded polymer system comparing to physically adsorbed chains using broadband dielectric spectroscopy (BDS) and NMR techniques.[13,14]

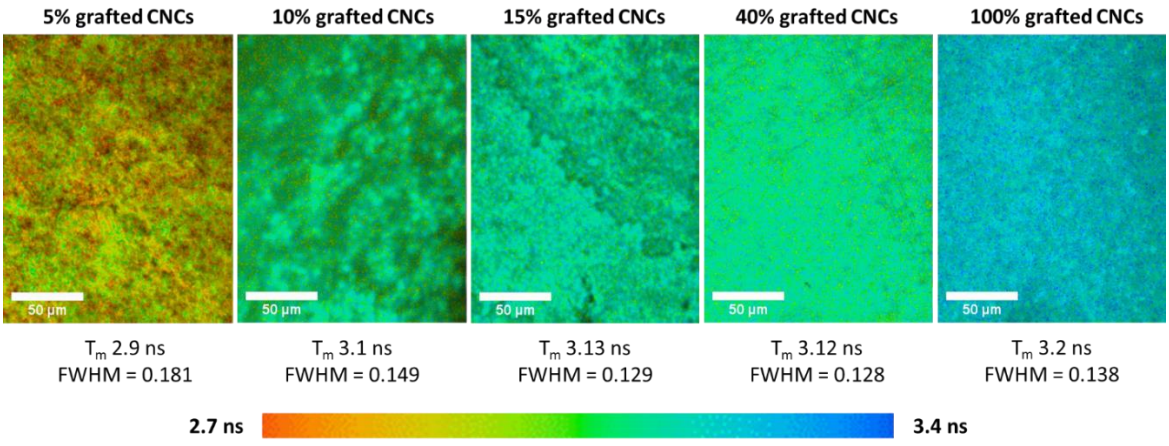

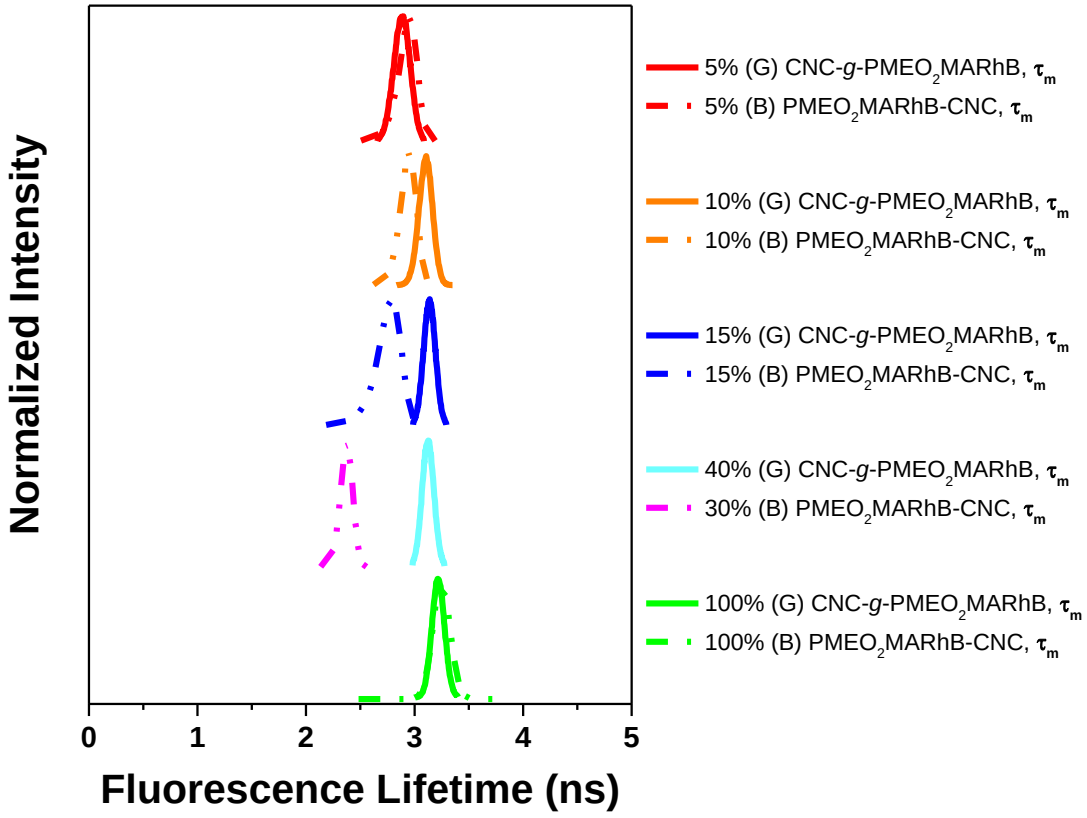

Figure 4.11. The FLIM images of the CNC-*g*-PMEO$_2$MARhB series (top) and normalized fluorescence lifetime for CNC-*g*-PMEO$_2$MARhB (bottom) shown in solid and the dashes represents average fluorescence lifetimes of PMEO$_2$MARhB-CNC series.

To observe how 10 % Grafted-CNC responded to water, it was exposed in 95 % RH environment then FLIM measurements were acquired as water evaporated from the sample. The FLIM images of the sample re-equilibrating to ambient conditions showed a shift in color and the τ_m shifted to longer lifetime by about 0.1 ns, **Figure 4.12**. Since there is only a single lifetime, the change in fluorescence lifetime is not as prominent compared to the two-component fitting in the blended system. The darker regions where most CNCs content is concentrated appeared to have an affinity for water due to the shorter lifetime residing there. This revealed that water retention was not homogeneous throughout the sample and CNC-*g*-PMEO$_2$MARhB content was helpful in water desorption.

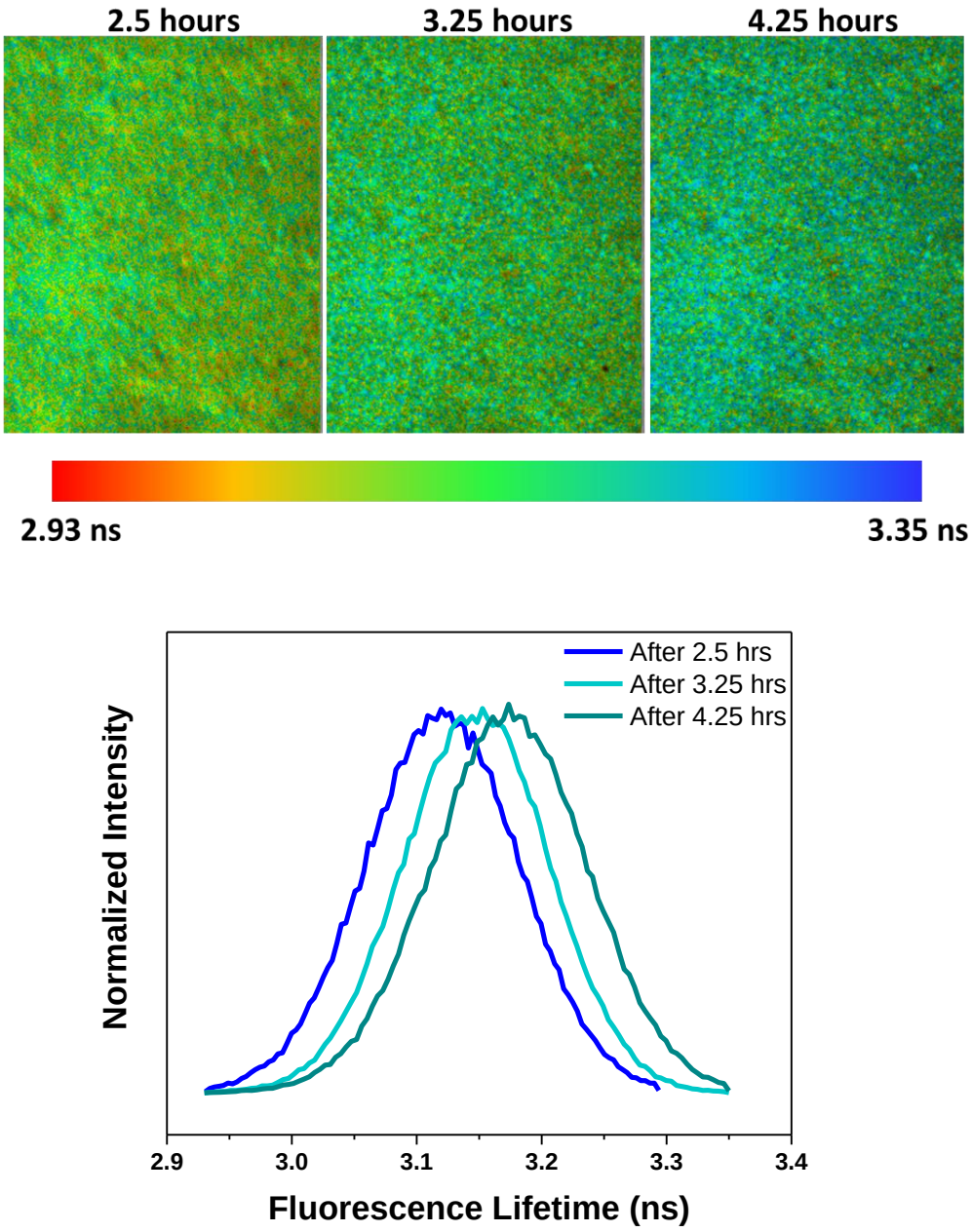

Figure 4.12. Normalized FLIM images and fluorescence lifetime of 10 % CNC-*g*-PMEO$_2$MARhB after 3 and 4 hours outside of 95 % RH environment.

4.3.4. Morphology and Mechanical Characterization of CNC-*g*-PMEO2MA Films

Studies done by Keten *et al.* looked at different parameters to optimize mechanical stiffness and toughness. They discovered that grafting density and polymer chain length are the influencing parameters to tune mechanical properties. According to their computational work, CNC nanoparticles should be more than 60 mass % and the grafted chains must be above the critical length to be in the semi-dilute brush regime.[15] For our grafted-CNC system, the 74 mass % grafted polymer sample was chosen to blend with pristine CNCs to cast films. The mechanical performances were determined at ambient conditions, shown in **Figure 4.13** and compared to blended $PMEO_2MA$RhB-CNC films**.** The grafted-CNC samples were plotted to reflect the actual mass fraction of $PMEO_2MA$RhB calculated from TGA results. Therefore, the 5 %, 15 %, and 40 % Grafted-CNC films corresponded to 3.75, 11, and 30 mass % of $PMEO_2MA$RhB, respectively.

With polymer chains being restricted to CNCs, we expected the grafted-CNC films to have higher stress-transfer efficiency comparing to the blended $PMEO_2MA$-CNC. The 5 % and 15 % Grafted-CNC samples performed better than the 5 % to 15 % $PMEO_2MA$RhB-CNC films in tensile strength and modulus with improvement for strain and toughness. The increase in strength indicated how covalently bonding polymer inhibited chain motions, resulted in improvement in stress transfer between CNCs and polymer components. Increase in strength could also be due to chain entanglements or intermolecular bonding that restricted polymer mobility. Specifically, covalent bonds and even secondary intermolecular bonds, like van der Waals, could result in improvement in tensile strength. An increase in modulus often occurs when secondary forces and chain alignment contribute to mechanical performance.[16]

Interestingly, the 40 % Grafted-CNC sample behaved differently from the 5 % and 15 % Grafted-CNC samples. The 40 % Grafted-CNC has roughly 30 mass % of $PMEO_2MARhB$, making it comparable to the 30 % $PMEO_2MARhB$-CNC. The tensile strength and modulus were similar for both systems with no improvement in stress transfer between CNCs and the grafted polymer. However, the strain and toughness dropped by a factor of three for the Grafted-CNC comparing to the 30 % $PMEO_2MARhB$-CNC. FLIM provided insights to these observations. Due to being restricted to CNC surface, the 40 % Grafted-CNC has an average fluorescence lifetime of 3.1 ns while 30 % $PMEO_2MARhB$-CNC has two-component fluorescence lifetimes with the average fluorescence lifetime around 2.4 ns. The shorter fluorescence lifetime in 30 % $PMEO_2MARhB$-CNC resulted from polymer saturation and the mobile polymer component, represented as τ_1, allowed CNC rods to glide pass one another. The unbounded polymer greatly improved the strain and toughness of CNCs nanocomposites. Despite having the same amount of polymer content, 40 % Grafted-CNC lacked the mobile polymer that would provide lubrication for the CNC rods, therefore resulted in a drop in strain and toughness.

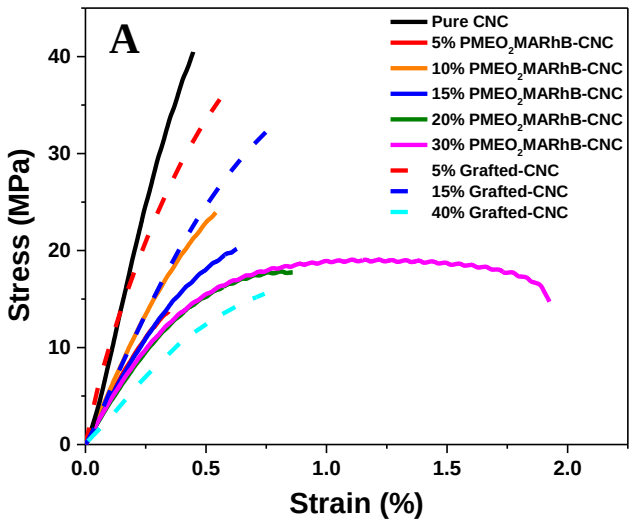

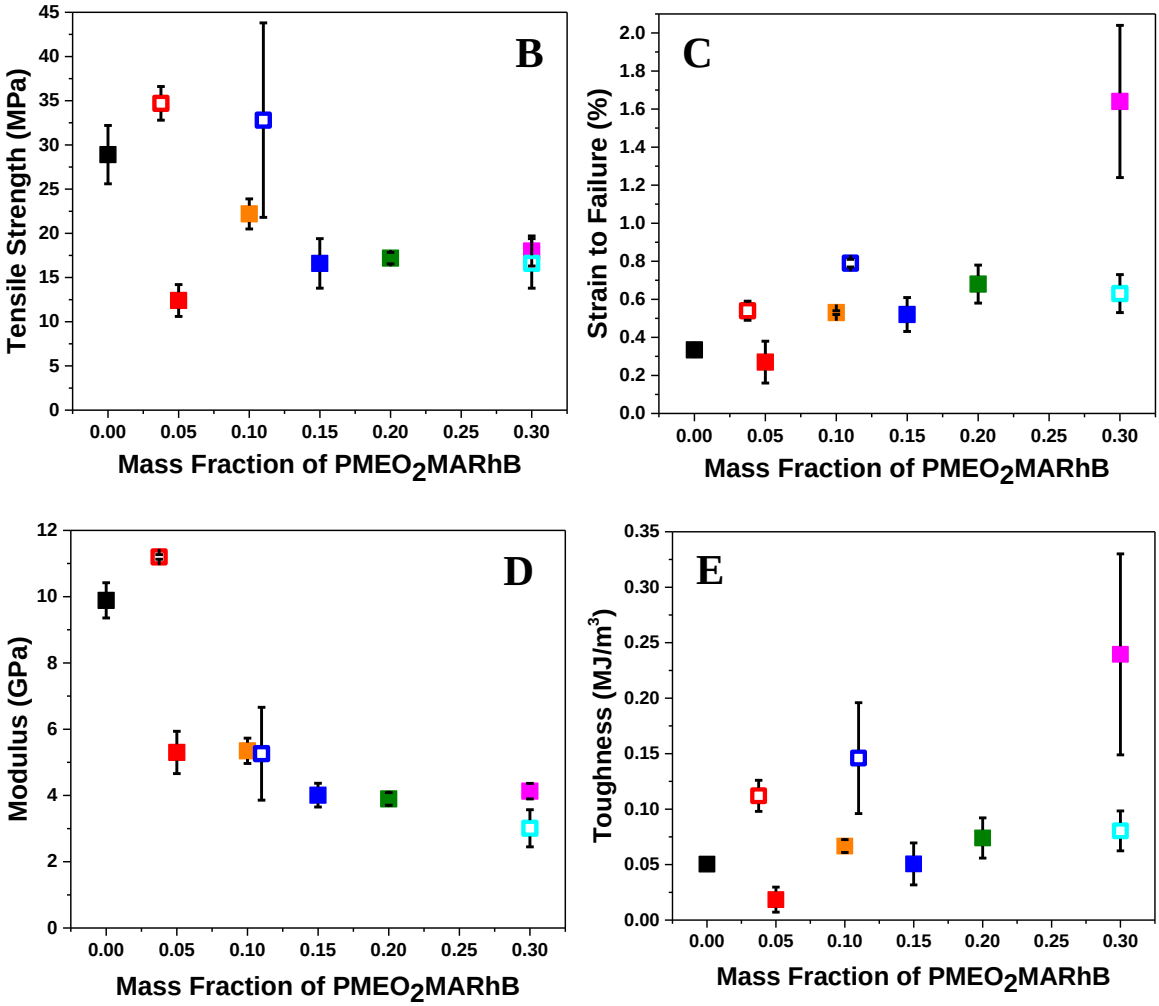

Figure 4.13. Mechanical properties for blended (solid lines or close squares) and Grafted-CNC films (dashed lines or open squares) were compared A) stress-strain curves, B) tensile strength, C) strain to failure, D) modulus, and E) toughness as a function of $PMEO_2MARhB$.

Phase images of films interfaces were obtained from AFM to gain insights on mechanical performance. From **Figure 4.14**, the top (sample-air) and bottom (sample-substrate) interfaces exhibited cholesteric assembly and were similar for samples at and below 15 % CNC-*g*-$PMEO_2MARhB$. The polymer content in 40 % Grafted-CNC sample was not well incorporated into the CNC structures with some saturated at the surface. Despite grafting polymer chains to CNCs, polymer saturation still occurred and was also observed from the fractured films from SEM images. The polymer saturation might explain why the 40% grafted-CNC sample did not perform as well in strain and toughness as

expected. However, the mechanical performance could be different if CNC-*g*-$PMEO_2MARhB$ sample was directly cast without the pure CNC.

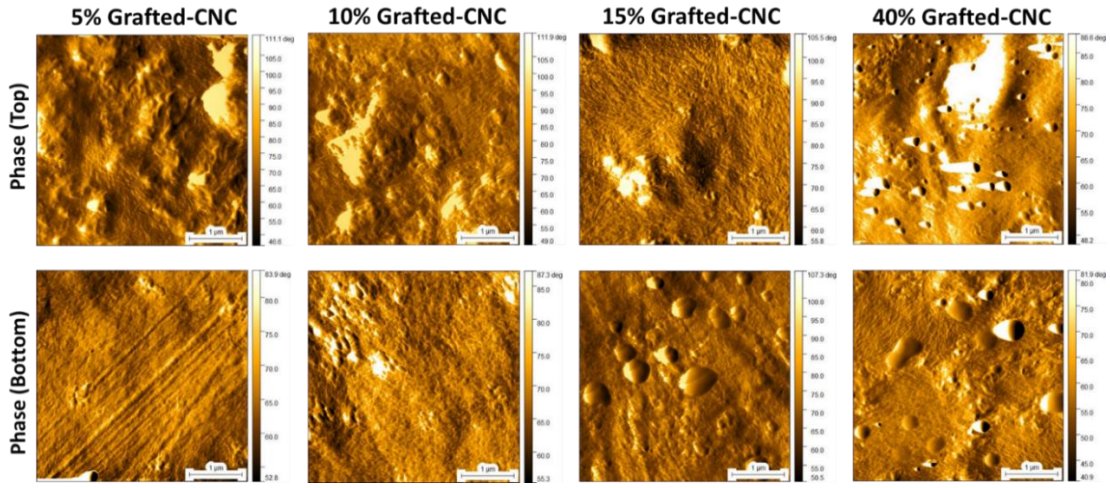

Figure 4.14. Phase images for 5 %, 10 %, 15 %, and 40 % Grafted-CNC films. The top side of the films (sample-air interface) are on the top row and the bottom side (sample-substrate interface) are on the bottom row. Scale bar is 1 µm.

4.4. Conclusions

We successfully grafted $PMEO_2MARhB$ polymer chains to CNC and casted free-standing films. The Grafted-CNC films had similar reflected colors trend and retained responsive to relative humidity conditions like the blended system. Through FLIM measurements, the Grafted-CNC films consistently had longer fluorescence lifetimes than the blended polymer-CNC due to restricted mobility of polymer chains. We postulated that polymer chains were mainly experiencing one environment within the CNC Bouligand structures. It appeared that the Grafted-CNC had better stress-transfer in comparison to the blended system because the polymer dynamics was confined to CNCs. However, this resulted in a sacrifice in toughness and strain because there is no mobile polymer to help the CNC rods slide pass one another and improve flexibility. The comparison between blended and grafted $PMEO_2MARhB$-CNC systems provided insights to how FLIM measurements correlate with the mechanical properties of CNC nanocomposites.

4.5. References

(1) Jain, A.; Gulbake, A.; Shilpi, S.; Jain, A.; Hurkat, P. A New Horizon in Modifications of Chitosan : Syntheses and Applications A New Horizon in Modifications of Chitosan : Syntheses and Applications. **2013**, No. March. https://doi.org/10.1615/CritRevTherDrugCarrierSyst.2013005678.

(2) Rubio, N.; Au, H.; Leese, H. S.; Hu, S.; Clancy, A. J.; Sha, M. S. P. Grafting from versus Graf Ting to Approaches for the Functionalization of Graphene Nanoplatelets with Poly(Methyl Methacrylate). **2017**. https://doi.org/10.1021/acs.macromol.7b01047.

(3) Thielemans, W.; Wohlhauser, S.; Delepierre, G.; Labet, M.; Weder, C.; Zoppe, J. O. Grafting Polymers from Cellulose Nanocrystals : Synthesis , Properties , and Applications. *Macromolecules* **2018**, *51*, 6157–6189. https://doi.org/10.1021/acs.macromol.8b00733.

(4) Risteen, B.; Delepierre, G.; Srinivasarao, M.; Weder, C.; Russo, P.; Reichmanis, E.; Zoppe, J. Thermally Switchable Liquid Crystals Based on Cellulose Nanocrystals with Patchy Polymer Grafts. *Small* **2018**, *14* (46), 1–10. https://doi.org/10.1002/smll.201802060.

(5) Zoppe, J. O.; Dupire, A. V. M.; Lachat, T. G. G.; Lemal, P.; Rodriguez-Lorenzo, L.; Petri-Fink, A.; Weder, C.; Klok, H. A. Cellulose Nanocrystals with Tethered Polymer Chains: Chemically Patchy versus Uniform Decoration. *ACS Macro Lett.* **2017**, *6* (9), 892–897. https://doi.org/10.1021/acsmacrolett.7b00383.

(6) Zoppe, J. O.; Österberg, M.; Venditti, R. A.; Laine, J.; Rojas, O. J. Surface Interaction Forces of Cellulose Nanocrystals Grafted with Thermoresponsive Polymer Brushes. *Biomacromolecules* **2011**, *12* (7), 2788–2796. https://doi.org/10.1021/bm200551p.

(7) Porsch, C.; Hansson, S.; Nordgren, N.; Malmström, E. Thermo-Responsive Cellulose-Based Architectures: Tailoring LCST Using Poly(Ethylene Glycol) Methacrylates. *Polym. Chem.* **2011**, *2* (5), 1114–1123. https://doi.org/10.1039/c0py00417k.

(8) Zoppe, J. O.; Habibi, Y.; Rojas, O. J.; Venditti, R. A.; Johansson, L. S.; Efimenko, K.; Österberg, M.; Laine, J. Poly(N -Isopropylacrylamide) Brushes Grafted from Cellulose Nanocrystals via Surface-Initiated Single-Electron Transfer Living Radical Polymerization. *Biomacromolecules* **2010**, *11* (10), 2683–2691. https://doi.org/10.1021/bm100719d.

(9) Azzam, F.; Siqueira, E.; Fort, S.; Hassaini, R.; Pignon, F.; Travelet, C.; Putaux, J. L.; Jean, B. Tunable Aggregation and Gelation of Thermoresponsive Suspensions of Polymer-Grafted Cellulose Nanocrystals. *Biomacromolecules* **2016**, *17* (6), 2112–2119. https://doi.org/10.1021/acs.biomac.6b00344.

(10) Grishkewich, N.; Akhlaghi, S. P.; Zhaoling, Y.; Berry, R.; Tam, K. C. Cellulose Nanocrystal-Poly(Oligo(Ethylene Glycol) Methacrylate) Brushes with Tunable LCSTs. *Carbohydr. Polym.* **2016**, *144*, 215–222. https://doi.org/10.1016/j.carbpol.2016.02.044.

(11) Woodcock, J. W.; Beams, R.; Davis, C. S.; Chen, N.; Stranick, S. J.; Shah, D. U.; Vollrath, F.; Gilman, J. W. Observation of Interfacial Damage in a Silk-Epoxy Composite, Using a Simple Mechanoresponsive Fluorescent Probe. *Adv. Mater. Interfaces* **2017**, *4* (10), 1–5. https://doi.org/10.1002/admi.201601018.

(12) Holt, A. P.; Bocharova, V.; Cheng, S.; Kisliuk, A. M.; White, B. T.; Saito, T.; Uhrig, D.; Mahalik, J. P.; Kumar, R.; Imel, A. E.; Etampawala, T.; Martin, H.; Sikes, N.; Sumpter, B. G.; Dadmun, M. D.; Sokolov, A. P. Controlling Interfacial Dynamics : Covalent Bonding versus Physical Adsorption in Polymer Nanocomposites. *ACS Nano* **2016**, *10* (7), 6843–6852. https://doi.org/10.1021/acsnano.6b02501.

(13) Klonos, P. A.; Goncharuk, O. V; Pakhlov, E. M.; Sternik, D.; Dery, A.; Kyritsis, A.; Gun, V. M.; Pissis, P. Morphology , Molecular Dynamics , and Interfacial Phenomena in Systems Based on Silica Modi Fi Ed by Grafting Polydimethylsiloxane Chains and Physically Adsorbed Polydimethylsiloxane. *Macromolecules* **2019**, *52* (7), 2863–2877. https://doi.org/10.1021/acs.macromol.9b00155.

(14) Berriot, J.; Lequeux, F.; Monnerie, L.; Montes, H. Filler – Elastomer Interaction in Model Filled Rubbers , a 1 H NMR Study. *J. Non. Cryst. Solids* **2002**, *310*, 719–724.

(15) Hansoge, N. K.; Huang, T.; Sinko, R.; Xia, W.; Chen, W.; Keten, S. Materials by Design for Stiff and Tough Hairy Nanoparticle Assemblies. *ACS Nano* **2018**, *12* (8), 7946–7958. https://doi.org/10.1021/acsnano.8b02454.

(16) Callister, W. D.; Rethwisch, D. G. *Materials Science and Engineering*, 8th ed.; John Wiley & Sons, 2011.

CHAPTER 5. CONCLUSIONS AND PERSPECTIVE

5.1. Introduction

This final chapter will present the significant findings from the three previous chapters and how these studies have enhanced the understanding of CNCs nanocomposites. Beyond these results, there is still work needed to explored to further the comprehension of the structure-property relationship of nanocomposites, especially on local dynamic responses and how they translate to mechanical performance. Some proposed future directions will be introduced as a possible continuation of this body of work.

5.2. Summary of Conclusions

In Chapter 2, there was the first reported study of phase transition via LCST that occurred in a solid-state film. This was done by blending poly(diethylene glycol methyl ether methacrylate) (LCST of 26 °C) with cellulose nanocrystals and forming thermoresponsive films through controlled evaporation-induced self-assembly. The structural coloration of the resulting CNC nanocomposite films can be tuned by polymer loadings, humidity, and temperature conditions. Increasing polymer loading led to reflected color transitioning from blue to red. Exposure to various relative humidity further shift the peak of reflectance to higher wavelength due to water molecules expanding the CNCs structures. The process is reverted when water is allowed to evaporate and the film's color returns to the initial state. The resulting films demonstrated additional reversible dynamic responses with temperature, going from transparent to opaque with increasing temperature. The transition is comparable to when $PMEO_2MA$ is in aqueous solution. The optical responses were within the visible light spectrum, making the CNC nanocomposites ideal as visual detectors for use in sensors and materials sensitive to human-contact.

Utilizing the same polymer-CNCs system, Chapter 3 focused on the experimental investigation of polymer chain dynamics via fluorescence lifetime measurements. Simply by labelling $PMEO_2MA$ homopolymer with a Rhodamine B-based water-sensitive dye, FLIM generated a fluorescence lifetime distribution within the film that probed different polymer dynamics. From the results, there are three postulated environments the polymer chains were experiencing in the CNCs composites. Longer fluorescence lifetimes are most likely associated with the polymer confined at the CNC interface and/or with less hydrated polymer domains while the shorter lifetimes are associated with more hydrated polymer domains. FLIM technique could be implemented in other water-sensitive systems and/or filler-matrix interfaces to study dynamic responses in the nanosecond regime. Fundamental understanding of polymer mobility will provide insights on how microscopic responses correlate to material properties.

Chapter 4 explored how the chain dynamics was altered when the polymer chains were anchored to CNCs surface via *grafting-from* technique. The Grafted-CNC films exhibited reflected colors and remained responsive to humidity conditions but not thermally. From FLIM results, the Grafted-CNC films had longer fluorescence lifetimes than the blended polymer-CNC due to one chain-end being restricted. There appeared to be one dominant mode of polymer dynamics within the CNC Bouligand structures for the Grafted-CNC films. For mechanical performance, the Grafted-CNCs films showed improvement in stress-transfer in comparison to the blended system. This was based on the higher strength the films exhibited likely due to the polymer being restricted to CNCs interface. The increase in strength came as a sacrifice in terms of strain and toughness because there was no excess polymer chain present to lubricate the CNC rods slide past

one another. This revealed the important presence of non-covalently mobile polymer component to improve flexibility in CNCs films.

5.3. Future Perspective

5.3.1. Explore Grafting Density and Polymer Loadings on CNCs Surface

For the grafted-CNCs system, the 74 % grafted polymer on CNCs was chosen to blend with pure CNCs in order to cast cholesteric films. However, computational studies done by Keten *et al.* have looked at different parameters to optimize mechanical stiffness and toughness and discovered that grafting density and polymer chain length are the influencing parameters to optimize mechanical properties. To achieve high mechanical performance, the mass percent of CNC should be more than 60 % and the grafted chains above the critical length needed for semi-dilute brush regime.[1] Due to these criteria, we have synthesized another sample with 58 % polymer loading (42 mass % CNCs) that would be interesting to study and compare with the lower CNCs content of the 74 % grafted polymer (26 mass % CNCs).

To determine whether the grafted chains are above the critical length of semidilute brush regime, a cleavable initiator should be used to examine polymer chains. The "*grafting-from*" technique yields higher polymer grafting density but the challenge is to quantify the chains length. In addition, the implemented ATRP initiator has similar carbonyl chemical structure as MEO_2MA monomer, which makes it difficult to selectively cleave the initiator without also cleaving the polymer side chains. A solution is to adopt an initiator with a different functional group that can be targeted without compromising the grafted polymer. Work done by Wohlhauser *et al.* grafted polymethacrylates by using 4-benzoylphenyl-(6-isocyanatohexyl) carbamate that could be selectively cleaved via

chlorosilane-induced cleavage of the urethane bond, seem in **Figure 5.1**.[2] By adopting the initiator, one could analyze the grafting chains and able to tune the chain length based on monomer feed.

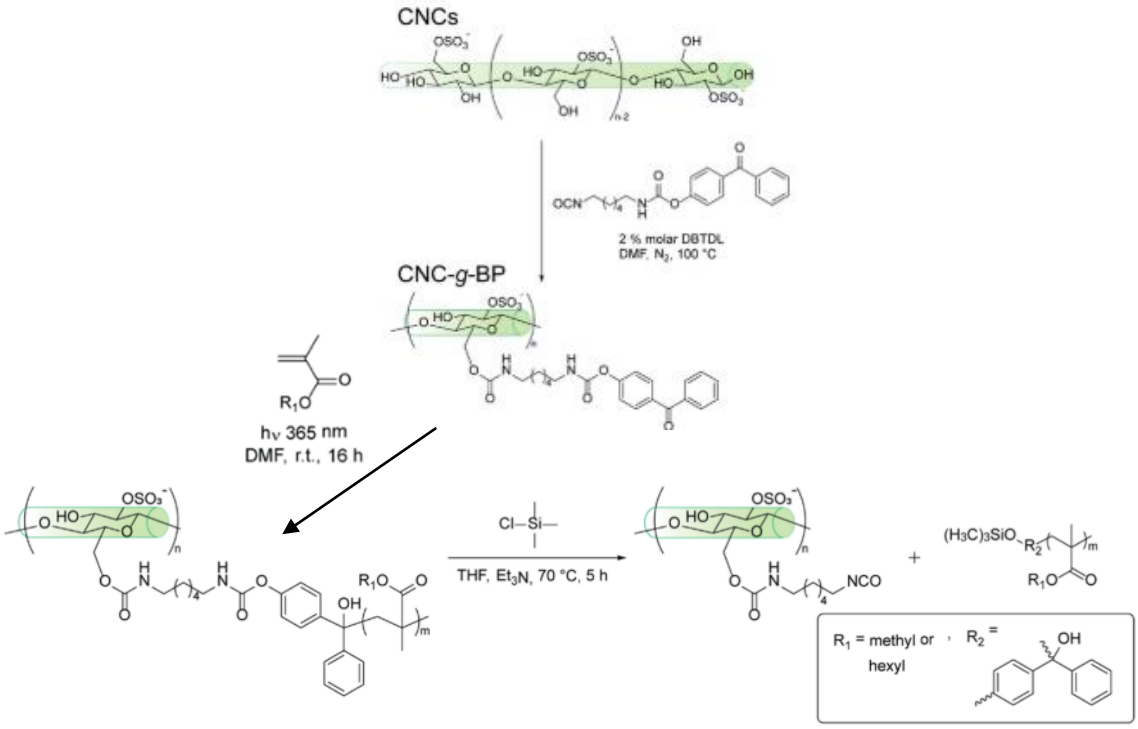

Figure 5.1. Surface functionalization of CNCs with 4-benzoylphenyl-(6-isocyanatohexyl) carbamate and grafting polymethacrylates on CNCs surface. To cleave the grafted polymer chains, chlorosilane-induced cleavage of urethane bond was done to obtain the polymer. Image is taken from Ref. 2.

5.3.2. Further Examinations with $POEGMA_{300}$ and PNIPAM Systems

Other thermoresponsive polymers could be studied beyond the $PMEO_2MA$ polymer that was examined in this dissertation. Since $PMEO_2MA$ belong in the oligoethylene glycol methacrylate family of LCST polymers, $POEGMA_{300}$ can be explored. The $POEGMA_{300}$ has a LCST of 64 °C because of the 4-5 repeating units of the PEO pendant group that makes it more hydrophilic in nature.[3] Based on preliminary results in Chapter 3, the increase in hydrophilic character would be interesting to observe whether

the interaction between $POEGMA_{300}$ and CNCs is improved and how it would be reflected in the fluorescence lifetime. Another well-known LCST polymer to explore is poly(N - isopropylacrylamide) (PNIPAM) with an LCST of 32 °C (**Figure 5.2)**.[4] Several polymer parameters can influence polymer dynamics in nanocomposites, such as molecular weight, architecture, and polymer stiffness.[5] A recent simulation work done by Keten *et al.* looked at the effects of polymer chemistry and chain conformation in CNC structures. By examining common polymers, the rigidity of polymer chains has an effect on the critical chain length that then relates back to achieving semi-dilute brush regime.[6] In comparison to $PMEO_2MA$ and the oligoethylene glycol methacrylate family, PNIPAM has more chain rigidity. The difference in rigidity and chemical structures within LCST polymers would tune thermoresponsive polymer-CNCs interactions that leads to mechanical property enhancements.

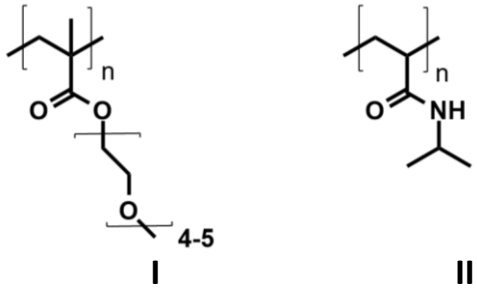

Figure 5.2. Schematic of $POEGMA_{300}$ with LCST of 64 °C (I) and PNIPAM with LCST of 32 °C (II).

5.3.3. Mechanical Performance in Various Relative Humidities

The CNC nanocomposites mechanical properties have been examined under ambient conditions (45 to 50 % RH) but not many literature reports have explored the films' responses to higher % RH. Based on a work of blended PVOH/CNC films, the samples were exposed to 99 % RH that ultimately caused plasticization of the interactions

between PVOH and CNC interface. This resulted in a longer elongation of break of up to 100 % strain.[7] We would like to replicate this experiment at high relative humidity in combination with temperatures above and below $PMEO_2MA$ LCST. Observing the films' behavior at various water content and temperature provides crucial insights on how the mechanical properties could be tuned dynamically.

5.3.4. Exploring Laser-Induced Projectile Impact Testing (LIPIT)

Uniaxial tensile-testing via DMA is often used to analyze the stress-strain curves of CNC nanocomposite films at a constant strain-rate but that only probes how these films behave in one configuration. The laser-induced projectile impacting testing (LIPIT) is a microscopic ballistic test that mimics the impacts of micro-particles in nature, such as sand, ice, and space particles, to determine the performance of thin films at ultra-high strain rate of 10^{-7} s^{-1}, shown in **Figure 5.3**. To determine the impact energy of the material, LIPIT measures the speed of micro-sized silica particle before and after impact.[8,9] This would be the first time CNC nanocomposites are being examined using two possible methodologies: impacting surface and penetrating through. Impacting surface testing is when the silica particle bounces off from the film's surface to understand the mechanical integrity for coating applications. The penetrating through test allows the silica particle to puncture through the sample to measure the impact energy, which is more suitable to examine high-impact materials.

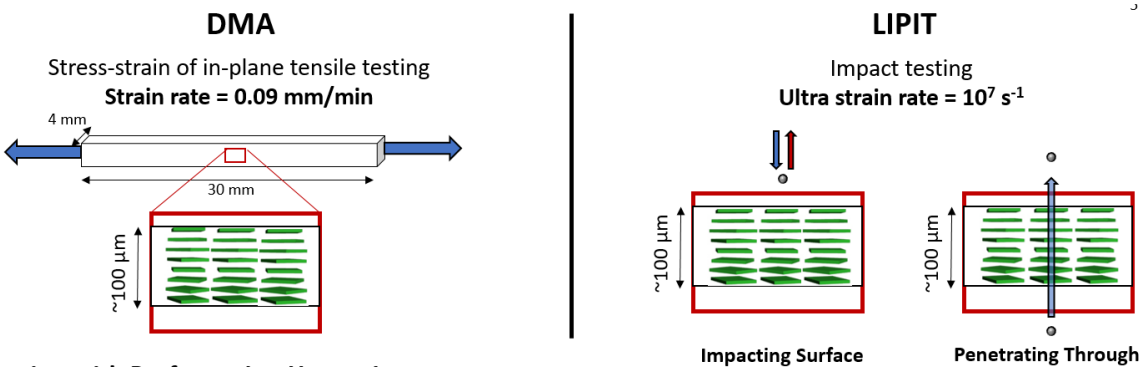

Figure 5.3. Schematic of DMA testing in comparison to the two LIPIT methodologies.

5.3.5. Correlating FLIM measurements to QENS studies

The FLIM measurements allowed polymer dynamics in CNC nanocomposites to be indirectly probed through fluorescence lifetime of the water-sensitive dye. For a direct measurements of polymer dynamics, quasi-elastic neutron scattering (QENS) could be used to correlate with the fluorescence lifetimes measurements.[10] The technique has been adopted to study water transport and polymer chain dynamics in membranes on the nanometers and nano- to picoseconds timescales.[11] This would allow further understanding to both the water diffusion within the CNC nanocomposite films and the chains motions under various humidity and temperature conditions. Obtaining the dynamic values from QENS will serve as reference points to connect the fluorescence lifetime to physical motions in CNC nanocomposites.

5.4. Outlook

With the increasing interest in utilizing cellulose nanocrystals in advanced applications, there are many explorations that has yet been done in the field to better understand how to design these renewable materials. The dissertation work done here should be extended and developed further in order to increase implementation of the renewable CNCs into novel materials. There are other polymer systems and

characterization techniques that should be examined to understand polymer interactions with CNCs structures. Additional investigations would propel and expand the applications to active coatings, smart-sensors, photonics, and high-impact materials.

5.5. References

(1) Hansoge, N. K.; Huang, T.; Sinko, R.; Xia, W.; Chen, W.; Keten, S. Materials by Design for Stiff and Tough Hairy Nanoparticle Assemblies. *ACS Nano* **2018**, *12* (8), 7946–7958. https://doi.org/10.1021/acsnano.8b02454.

(2) Wohlhauser, S.; Kuhnt, T.; Meesorn, W.; Espinosa, L. M. De; Zoppe, J. O.; Weder, C. One-Component Nanocomposites Based on Polymer-Grafted Cellulose Nanocrystals. *Macromolecules* **2020**, *53* (3), 821–834. https://doi.org/10.1021/acs.macromol.9b01612.

(3) Lutz, J. F.; Hoth, A.; Schade, K. Design of Oligo(Ethylene Glycol)-Based Thermoresponsive Polymers: An Optimization Study. *Des. Monomers Polym.* **2009**, *12* (4), 343–353. https://doi.org/10.1163/156855509X448316.

(4) Lutz, J. Thermo-Switchable Materials Prepared Using The. *Adv. Mater.* **2011**, *23* (19), 2237–2243. https://doi.org/10.1002/adma.201100597.

(5) Bailey, E. J.; Winey, K. I. Dynamics of Polymer Segments , Polymer Chains , and Nanoparticles in Polymer Nanocomposite Melts : A Review. *Prog. Polym. Sci.* **2020**, *105*, 101242. https://doi.org/10.1016/j.progpolymsci.2020.101242.

(6) Hansoge, N. K.; Keten, S. Effect of Polymer Chemistry on Chain Conformations in Hairy Nanoparticle Assemblies. *ACS Macro Lett.* **2019**, *8* (10), 1209–1215. https://doi.org/10.1021/acsmacrolett.9b00526.

(7) Wang, B.; Walther, A. Self-Assembled, Iridescent, Crustacean-Mimetic Nanocomposites with Tailored Periodicity and Layered Cuticular Structure. *ACS Nano* **2015**, *9* (11), 10637–10646. https://doi.org/10.1021/acsnano.5b05074.

(8) Lee, J. H.; Veysset, D.; Singer, J. P.; Retsch, M.; Saini, G.; Pezeril, T.; Nelson, K. A.; Thomas, E. L. High Strain Rate Deformation of Layered Nanocomposites. *Nat. Commun.* **2012**, *3* (1164). https://doi.org/10.1038/ncomms2166.

(9) Lee, J.; Veysset, D.; Nelson, K. A.; Thomas, E. L. Laser Induced Projectile Impact Test (LIPIT) A Micro-Scale Ballistic Test for High-Strain Rate Mechanical Study of Nano-Structures. *APS March 2012* **2012**.

(10) Jan, B.; Embs, P.; Juranyi, F.; Hempelmann, R. Introduction to Quasielastic Neutron Scattering. *Z. Phys. Chem.* **2010**, *224*, 5–32.

(11) Chan, E. P.; Frieberg, B. R.; Ito, K.; Tarver, J.; Tyagi, M.; Zhang, W.; Coughlin, E. B.; Sta, C. M.; Roy, A.; Rosenberg, S.; Soles, C. L. Insights into the Water Transport Mechanism in Polymeric Membranes from Neutron Scattering. *Macromolecules* **2020**, *53* (4), 1443–1450. https://doi.org/10.1021/acs.macromol.9b02195.

APPENDIX

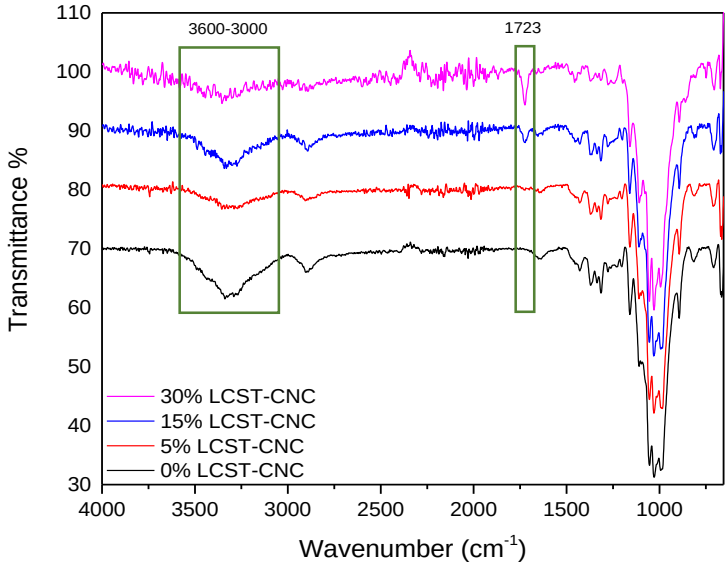

A1. FTIR spectra of the $PMEO_2MA$-CNC films (left), showing the increase of C=O band as $PMEO_2MA$ concentration increases.

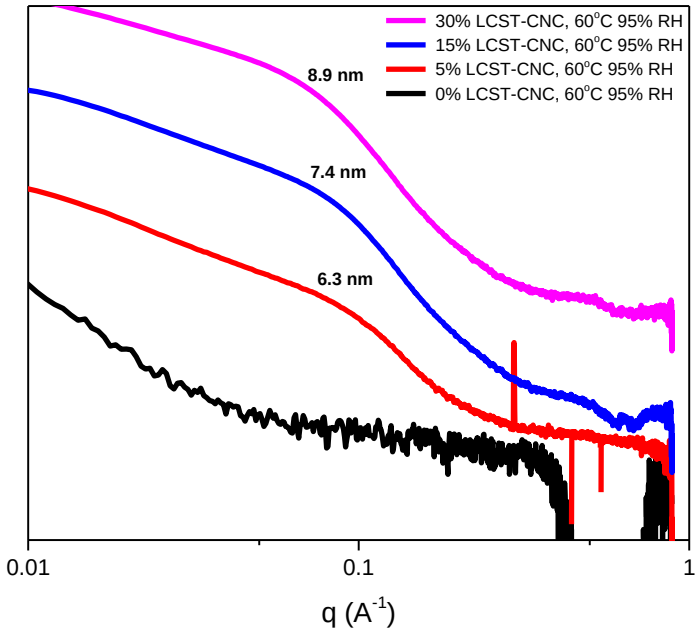

A2. GISAXS data for pure CNCs, 5%, 15%, and 30% $PMEO_2MA$-CNC after being soaked in water then maintained at 95 % RH at 60 °C.

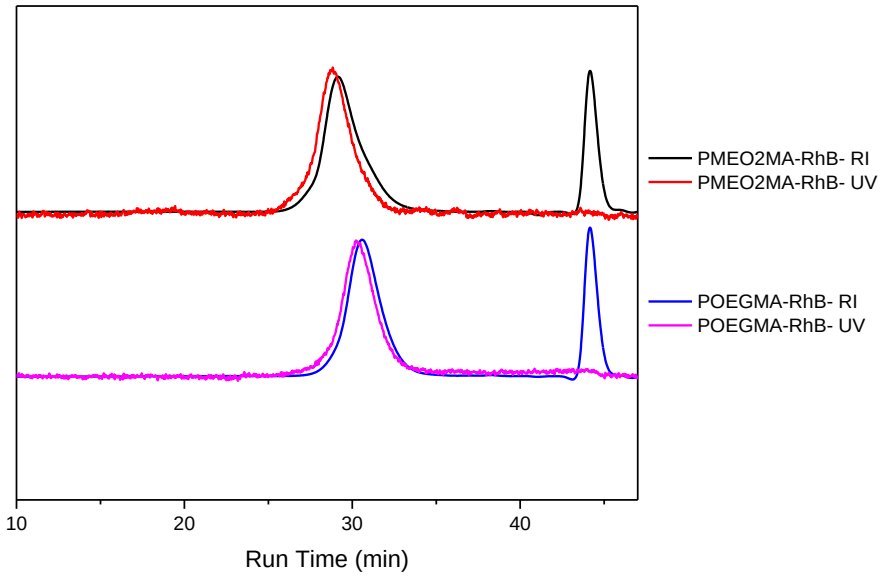

Sample	M_n (g/mol)	M_w (g/mol)	Đ	DP	Target M_n (g/mol)
$PMEO_2MA$-RHB	12,000	20,000	1.3	63	28,200
POEGMA-RHB	7,100	9,900	1.4	23	27,000

A3. DMF-GPC of $PMEO_2MA$-RhB and POEGMA-RhB with RI and UV (254 nm) detection (PEG Standards).

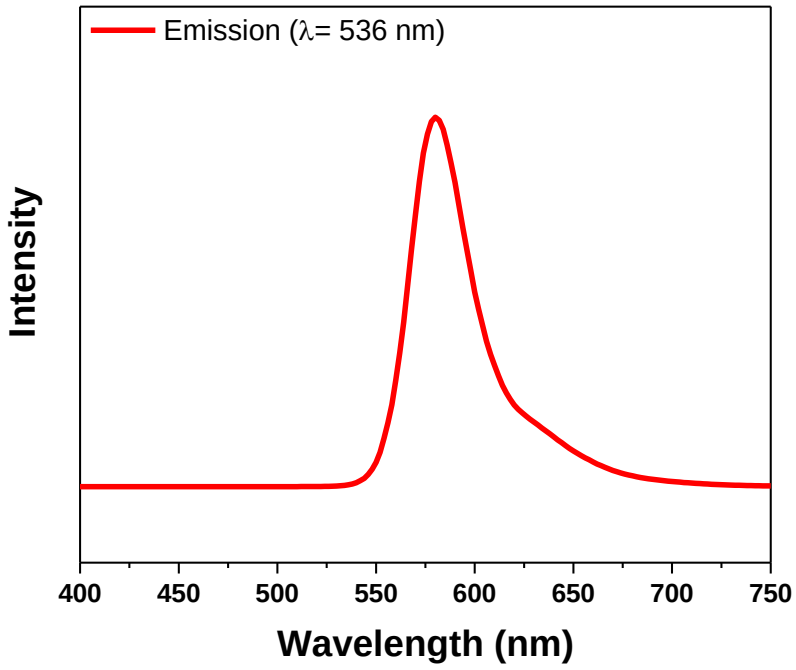

A4. Emission of RhB-MMA at 590 nm (excited at 536 nm).

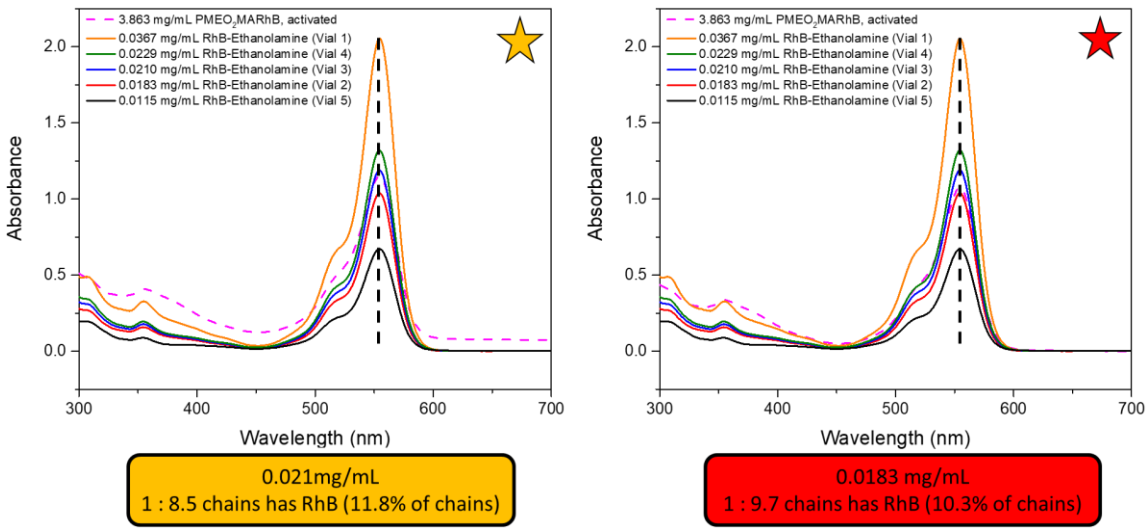

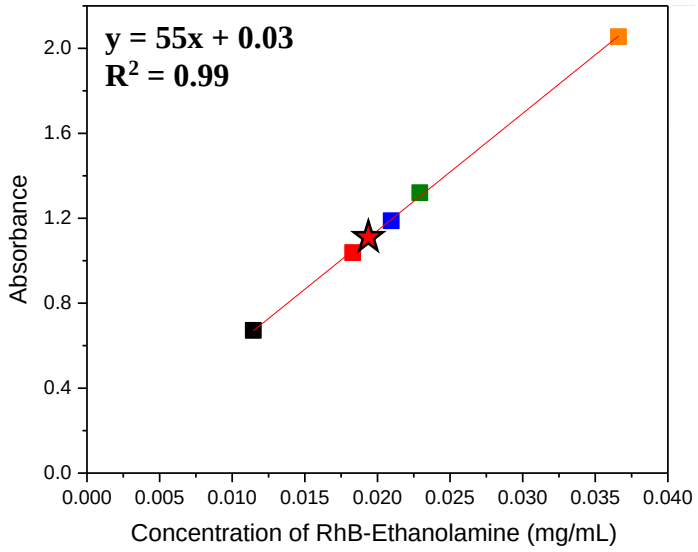

A5. Estimate RhB-ethanolamine in $PMEO_2MARhB$ using UV-vis spectrometer.

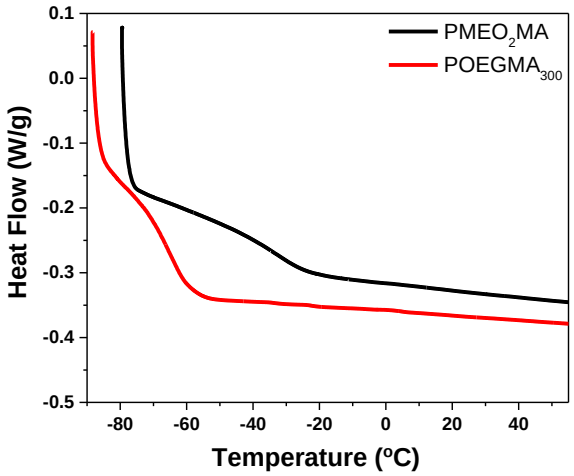

A6. DSC curves for $PMEO_2MA$ with $T_g = -33$ °C and $POEGMA_{300}$ with $T_g = -65$ °C.

BIBLIOGRAPHY

Anglès, M. N.; Dufresne, A. Plasticized Starch/Tunicin Whiskers Nanocomposite Materials. 2: Mechanical Behavior. *Macromolecules* **2001**, *34* (9), 2921–2931. https://doi.org/10.1021/ma001555h.

Aulin, C.; Ahok, S.; Josefsson, P.; Nishino, T.; Hirose, Y.; Österberg, M.; Wågberg, L. Nanoscale Cellulose Films with Different Crystallinities and Mesostructures - Their Surface Properties and Interaction with Water. *Langmuir* **2009**, *25* (13), 7675–7685. https://doi.org/10.1021/la900323n.

Azzam, F.; Siqueira, E.; Fort, S.; Hassaini, R.; Pignon, F.; Travelet, C.; Putaux, J. L.; Jean, B. Tunable Aggregation and Gelation of Thermoresponsive Suspensions of Polymer-Grafted Cellulose Nanocrystals. *Biomacromolecules* **2016**, *17* (6), 2112–2119. https://doi.org/10.1021/acs.biomac.6b00344.

Bailey, E. J.; Gri, P. J.; Tyagi, M.; Winey, K. I. Quasi-Elastic Neutron Scattering Study. *Macromolecules* **2019**, *52* (2), 669–678. https://doi.org/10.1021/acs.macromol.8b01716.

Bailey, E. J.; Winey, K. I. Dynamics of Polymer Segments , Polymer Chains , and Nanoparticles in Polymer Nanocomposite Melts : A Review. *Prog. Polym. Sci.* **2020**, *105*, 101242. https://doi.org/10.1016/j.progpolymsci.2020.101242.

Bardet, R.; Belgacem, N.; Bras, J. Flexibility and Color Monitoring of Cellulose Nanocrystal Iridescent Solid Films Using Anionic or Neutral Polymers. *ACS Appl. Mater. Interfaces* **2015**, *7* (7), 4010–4018. https://doi.org/10.1021/am506786t.

Berriot, J.; Lequeux, F.; Monnerie, L.; Montes, H. Filler – Elastomer Interaction in Model Filled Rubbers , a 1 H NMR Study. *J. Non. Cryst. Solids* **2002**, *310*, 719–724.

Blacker, T. S.; Mann, Z. F.; Gale, J. E.; Ziegler, M.; Bain, A. J.; Szabadkai, G.; Duchen, M. R. Separating NADH and NADPH Fluorescence in Live Cells and Tissues Using FLIM. *Nat. Commun.* **2014**, *5* (3936). https://doi.org/10.1038/ncomms4936.

Callister, W. D.; Rethwisch, D. G. *Materials Science and Engineering*, 8th ed.; John Wiley & Sons, 2011.

Carroll, B.; Cheng, S.; Sokolov, A. P. Analyzing the Interfacial Layer Properties in Polymer Nanocomposites by Broadband Dielectric Spectroscopy. *Macromolecules* **2017**, *50* (16), 6149–6163. https://doi.org/10.1021/acs.macromol.7b00825.

Chan, E. P.; Frieberg, B. R.; Ito, K.; Tarver, J.; Tyagi, M.; Zhang, W.; Coughlin, E. B.; Sta, C. M.; Roy, A.; Rosenberg, S.; Soles, C. L. Insights into the Water Transport Mechanism in Polymeric Membranes from Neutron Scattering. *Macromolecules* **2020**, *53* (4), 1443–1450. https://doi.org/10.1021/acs.macromol.9b02195.

Chen, P. Y.; Lin, A. Y. M.; McKittrick, J.; Meyers, M. A. Structure and Mechanical Properties of Crab Exoskeletons. *Acta Biomater.* **2008**, *4* (3), 587–596. https://doi.org/10.1016/j.actbio.2007.12.010.

Christie, D.; Register, R. A.; Priestley, R. D. Direct Measurement of the Local Glass Transition in Self-Assembled Copolymers with Nanometer Resolution. *ACS Cent. Sci.* **2018**, *4*, 504–511. https://doi.org/10.1021/acscentsci.8b00043.

Christie, D.; Register, R. A.; Priestley, R. D. Role of Chain Connectivity across an Interface on the Dynamics of a Nanostructured Block Copolymer. *Phys. Rev. Lett.* **2018**, *121* (24), 247801. https://doi.org/10.1103/PhysRevLett.121.247801.

Dagnon, K. L.; Shanmuganathan, K.; Weder, C.; Rowan, S. J. Water-Triggered Modulus Changes of Cellulose Nanofiber Nanocomposites with Hydrophobic Polymer Matrices. *Macromolecules* **2012**, *45* (11), 4707–4715. https://doi.org/10.1021/ma300463y.

Davis, D. A.; Hamilton, A.; Yang, J.; Cremar, L. D.; Van Gough, D.; Potisek, S. L.; Ong, M. T.; Braun, P. V.; Martínez, T. J.; White, S. R.; Moore, J. S.; Sottos, N. R. Force-Induced Activation of Covalent Bonds in Mechanoresponsive Polymeric Materials. *Nature* **2009**, *459* (7243), 68–72. https://doi.org/10.1038/nature07970.

Geng, S.; Yao, K.; Zhou, Q.; Oksman, K. High-Strength, High-Toughness Aligned Polymer-Based Nanocomposite Reinforced with Ultralow Weight Fraction of Functionalized Nanocellulose. *Biomacromolecules* **2018**, *19* (10), 4075–4083. https://doi.org/10.1021/acs.biomac.8b01086.

Grishkewich, N.; Akhlaghi, S. P.; Zhaoling, Y.; Berry, R.; Tam, K. C. Cellulose Nanocrystal-Poly(Oligo(Ethylene Glycol) Methacrylate) Brushes with Tunable LCSTs. *Carbohydr. Polym.* **2016**, *144*, 215–222. https://doi.org/10.1016/j.carbpol.2016.02.044.

Grunenfelder, L. K.; Herrera, S.; Kisailus, D. Crustacean-Derived Biomimetic Components and Nanostructured Composites. *Small* **2014**, *10* (16), 3207–3232. https://doi.org/10.1002/smll.201400559.

Guarín-Zapata, N.; Gomez, J.; Yaraghi, N.; Kisailus, D.; Zavattieri, P. D. Shear Wave Filtering in Naturally-Occurring Bouligand Structures. *Acta Biomater.* **2015**, *23*, 11–20. https://doi.org/10.1016/j.actbio.2015.04.039.

Guidetti, G.; Atifi, S.; Vignolini, S.; Hamad, W. Y. Flexible Photonic Cellulose Nanocrystal Films. *Adv. Mater.* **2016**, *28* (45), 10042–10047. https://doi.org/10.1002/adma.201603386.

Guidetti, G.; Atifi, S.; Vignolini, S.; Hamad, W. Y. Flexible Photonic Cellulose Nanocrystal Films. *Adv. Mater.* **2016**, *28* (45), 10042–10047. https://doi.org/10.1002/adma.201603386.

Habibi, Y.; Goffin, A. L.; Schiltz, N.; Duquesne, E.; Dubois, P.; Dufresne, A. Bionanocomposites Based on Poly(ε-Caprolactone)-Grafted Cellulose Nanocrystals by Ring-Opening Polymerization. *J. Mater. Chem.* **2008**, *18* (41), 5002–5010. https://doi.org/10.1039/b809212e.

Habibi, Y.; Lucia, L. A.; Rojas, O. J. Cellulose Nanocrystals: Chemistry, Self-Assembly, and Applications. *Chem. Rev.* **2010**, *110* (6), 3479–3500. https://doi.org/10.1021/cr900339w.

Hamad, W. Y. *Cellulose Nanocrystals: Properties, Production and Applications*; 2017. https://doi.org/10.1002/9781118675601.

Han, S.; Hagiwara, M.; Ishizone, T. Synthesis of Thermally Sensitive Water-Soluble Polymethacrylates by Living Anionic Polymerizations of Oligo (Ethylene Glycol) Methyl Ether Methacrylates. *Macromolecules* **2003**, *36* (22), 8312–8319. https://doi.org/10.1021/ma0347971.

Hansoge, N. K.; Huang, T.; Sinko, R.; Xia, W.; Chen, W.; Keten, S. Materials by Design for Stiff and Tough Hairy Nanoparticle Assemblies. *ACS Nano* **2018**, *12* (8), 7946–7958. https://doi.org/10.1021/acsnano.8b02454.

Hansoge, N. K.; Keten, S. Effect of Polymer Chemistry on Chain Conformations in Hairy Nanoparticle Assemblies. *ACS Macro Lett.* **2019**, *8* (10), 1209–1215. https://doi.org/10.1021/acsmacrolett.9b00526.

He, Y.; Zhang, Z.; Xue, J.; Wang, X.; Song, F.; Wang, X.; Zhu, L.; Wang, Y. Biomimetic Optical Cellulose Nanocrystal Films with Controllable Iridescent Color and Environmental Stimuli-Responsive Chromism. *ACS Appl. Mater. Interfaces* **2018**, *10* (6), 5805–5811. https://doi.org/10.1021/acsami.7b18440.

Holt, A. P.; Bocharova, V.; Cheng, S.; Kisliuk, A. M.; White, B. T.; Saito, T.; Uhrig, D.; Mahalik, J. P.; Kumar, R.; Imel, A. E.; Etampawala, T.; Martin, H.; Sikes, N.; Sumpter, B. G.; Dadmun, M. D.; Sokolov, A. P. Controlling Interfacial Dynamics : Covalent Bonding versus Physical Adsorption in Polymer Nanocomposites. *ACS Nano* **2016**, *10* (7), 6843–6852. https://doi.org/10.1021/acsnano.6b02501.

Ishikawa-ankerhold, H. C.; Ankerhold, R.; Drummen, G. P. C.; Biology, C.; Zeiss, C.; Gmbh, M.; Program, B.; Stress, C.; Program, A. Advanced Fluorescence Microscopy Techniques—FRAP , FLIP , FLAP , FRET and FLIM. *Molecules* **2012**, *17* (4), 4047–4132. https://doi.org/10.3390/molecules17044047.

Jain, A.; Blum, C.; Subramaniam, V. Chapter 4 - Fluorescence Lifetime Spectroscopy and Imaging of Visible Fluorescent Proteins. In *Advances in Biomedical Engineering*; 2009; pp 147–176.

Jain, A.; Gulbake, A.; Shilpi, S.; Jain, A.; Hurkat, P. A New Horizon in Modifications of Chitosan : Syntheses and Applications A New Horizon in Modifications of Chitosan : Syntheses and Applications. **2013**, No. March. https://doi.org/10.1615/CritRevTherDrugCarrierSyst.2013005678.

Jan, B.; Embs, P.; Juranyi, F.; Hempelmann, R. Introduction to Quasielastic Neutron Scattering. *Z. Phys. Chem.* **2010**, *224*, 5–32.

Kim, S.; Hewlett, S. A.; Roth, C. B.; Torkelson, J. M. Confinement Effects on Glass Transition Temperature , Transition Breadth , and Expansivity : Comparison of Ellipsometry And. *Eur. Phys. J. E* **2009**, *92* (30), 83–92. https://doi.org/10.1140/epje/i2009-10510-y.

Klemm, D.; Kramer, F.; Moritz, S.; Lindström, T.; Ankerfors, M.; Gray, D.; Dorris, A. Nanocelluloses: A New Family of Nature-Based Materials. *Angew. Chemie - Int. Ed.* **2011**, *50* (24), 5438–5466. https://doi.org/10.1002/anie.201001273.

Klonos, P. A.; Goncharuk, O. V; Pakhlov, E. M.; Sternik, D.; Dery, A.; Kyritsis, A.; Gun, V. M.; Pissis, P. Morphology , Molecular Dynamics , and Interfacial Phenomena in Systems Based on Silica Modi Fi Ed by Grafting Polydimethylsiloxane Chains and Physically Adsorbed Polydimethylsiloxane. *Macromolecules* **2019**, *52* (7), 2863–2877. https://doi.org/10.1021/acs.macromol.9b00155.

Kose, O.; Tran, A.; Lewis, L.; Hamad, W. Y.; Maclachlan, M. J. Unwinding a Spiral of Cellulose Nanocrystals for Stimuli-Responsive Stretchable Optics. *Nat. Commun.* **2019**, *10* (510). https://doi.org/10.1038/s41467-019-08351-6.

Kremer, F.; Schonhals, A. *Broadband Dielectric Spectroscopy*; Springer-Verlag: Berlin, 2002.

Lee, J. H.; Veysset, D.; Singer, J. P.; Retsch, M.; Saini, G.; Pezeril, T.; Nelson, K. A.; Thomas, E. L. High Strain Rate Deformation of Layered Nanocomposites. *Nat. Commun.* **2012**, *3* (1164). https://doi.org/10.1038/ncomms2166.

Lee, J.; Veysset, D.; Nelson, K. A.; Thomas, E. L. Laser Induced Projectile Impact Test (LIPIT) A Micro-Scale Ballistic Test for High-Strain Rate Mechanical Study of Nano-Structures. *APS March 2012* **2012**.

Lenhart, J. L.; Van Zanten, J. H.; Dunkers, J. P.; Parnas, R. S. Studying the Buried Interfacial Region with an Immobilized Fluorescence Probe. *Macromolecules* **2001**, *34* (7), 2225–2231. https://doi.org/10.1021/ma0015572.

Lin, C. C.; Parrish, E.; Composto, R. J. Macromolecule and Particle Dynamics in Confined Media. *Macromolecules* **2016**, *49* (16), 5755–5772. https://doi.org/10.1021/acs.macromol.6b00471.

Lutz, J. F.; Hoth, A.; Schade, K. Design of Oligo(Ethylene Glycol)-Based Thermoresponsive Polymers: An Optimization Study. *Des. Monomers Polym.* **2009**, *12* (4), 343–353. https://doi.org/10.1163/156855509X448316.

Lutz, J. Thermo-Switchable Materials Prepared Using The. *Adv. Mater.* **2011**, *23* (19), 2237–2243. https://doi.org/10.1002/adma.201100597.

Lutz, Jean-Francois and Hoth, A. Preparation of Ideal PEG Analogues with a Tunable Thermosensitivity by Controlled Radical Copolymerization of 2-(2-Methoxyethoxy)Ethyl Methacrylate and Oligo(Ethylene Glycol) Methacrylate. *Macromolecules* **2006**, *39* (2), 893–896. https://doi.org/10.1021/ma0517042.

Lutz, Jean-Francois, Weichenhan, Katja, Akdemir, Ozgur, Hoth, A. About the Phase Transitions in Aqueous Solutions of Thermoresponsive Copolymers and Hydrogels Based on 2- (2-Methoxyethoxy) Ethyl Methacrylate and Oligo (Ethylene Glycol) Methacrylate. *Macromolecules* **2007**, *40* (7), 2503–2508. https://doi.org/10.1021/ma062925q.

Matsumoto, K.; Sakikawa, N.; Miyata, T. Thermo-Responsive Gels That Absorb Moisture and Ooze Water. *Nat. Commun.* **2018**, *9* (1), 1–7. https://doi.org/10.1038/s41467-018-04810-8.

Mitov, M. Cholesteric Liquid Crystals in Living Matter. *Soft Matter* **2017**, *13* (23), 4176–4209. https://doi.org/10.1039/c7sm00384f.

Munster, E. B. Van; Gadella, T. W. J. Fluorescence Lifetime Imaging Microscopy (FLIM) Alternating Current. In *Microscopy Techniques*; 2005; Vol. 95, pp 143–175. https://doi.org/10.1007/b102213.

Natarajan, B.; Emiroglu, C.; Obrzut, J.; Fox, D. M.; Pazmino, B.; Douglas, J. F.; Gilman, J. W. Dielectric Characterization of Confined Water in Chiral Cellulose Nanocrystal Films. *ACS Appl. Mater. Interfaces* **2017**, *9* (16), 14222–14231. https://doi.org/10.1021/acsami.7b01674.

Natarajan, B.; Emiroglu, C.; Obrzut, J.; Fox, D. M.; Pazmino, B.; Douglas, J. F.; Gilman, J. W. Dielectric Characterization of Confined Water in Chiral Cellulose Nanocrystal Films. *ACS Appl. Mater. Interfaces* **2017**, *9* (16), 14222–14231. https://doi.org/10.1021/acsami.7b01674.

Natarajan, B.; Gilman, J. W. Bioinspired Bouligand Cellulose Nanocrystal Composites: A Review of Mechanical Properties. *Philos. Trans. A. Math. Phys. Eng. Sci.* **2018**, *376* (2112), 20170050. https://doi.org/10.1098/rsta.2017.0050.

Natarajan, B.; Krishnamurthy, A.; Qin, X.; Emiroglu, C. D.; Forster, A.; Foster, E. J.; Weder, C.; Fox, D. M.; Keten, S.; Obrzut, J.; Gilman, J. W. Binary Cellulose Nanocrystal Blends for Bioinspired Damage Tolerant Photonic Films. *Adv. Funct. Mater.* **2018**, *28* (26), 1800032. https://doi.org/10.1002/adfm.201800032.

Okabe, K.; Inada, N.; Gota, C.; Harada, Y.; Funatsu, T.; Uchiyama, S. Intracellular Temperature Mapping with a Fluorescent Polymeric Thermometer and Fluorescence Lifetime Imaging Microscopy. *Nat. Commun.* **2012**, *3* (705), 1–9. https://doi.org/10.1038/ncomms1714.

Padilla-Parra, S.; Tramier, M. FRET Microscopy in the Living Cell: Different Approaches, Strengths and Weaknesses. *BioEssays* **2012**, *34* (5), 369–376. https://doi.org/10.1002/bies.201100086.

Porsch, C.; Hansson, S.; Nordgren, N.; Malmström, E. Thermo-Responsive Cellulose-Based Architectures: Tailoring LCST Using Poly(Ethylene Glycol) Methacrylates. *Polym. Chem.* **2011**, *2* (5), 1114–1123. https://doi.org/10.1039/c0py00417k.

Priestley, R. D.; Cangialosi, D.; Napolitano, S. On the Equivalence between the Thermodynamic and Dynamic Measurements of the Glass Transition in Con Fi Ned Polymers. *J. Non. Cryst. Solids* **2015**, *407*, 288–295. https://doi.org/10.1016/j.jnoncrysol.2014.09.048.

Provenzano, P. P.; Eliceiri, K. W.; Keely, P. J. Multiphoton Microscopy and Fluorescence Lifetime Imaging Microscopy (FLIM) to Monitor Metastasis and the Tumor Microenvironment. *Clin Exp Metastasis* **2009**, *26*, 357–370. https://doi.org/10.1007/s10585-008-9204-0.

Raabe, D.; Sachs, C.; Romano, P. The Crustacean Exoskeleton as an Example of a Structurally and Mechanically Graded Biological Nanocomposite Material. *Acta Mater.* **2005**, *53* (15), 4281–4292. https://doi.org/10.1016/j.actamat.2005.05.027.

Richter, D.; Monkenbusch, S. D. Neutron Scattering. In *Polymer science: a comprehensive reference*; Matyjaszewski, K., Moller, M., Eds.; Elsevier BV: Amsterdam, 2012; pp 331–360.

Risteen, B.; Delepierre, G.; Srinivasarao, M.; Weder, C.; Russo, P.; Reichmanis, E.; Zoppe, J. Thermally Switchable Liquid Crystals Based on Cellulose Nanocrystals with Patchy Polymer Grafts. *Small* **2018**, *14* (46), 1–10. https://doi.org/10.1002/smll.201802060.

Rittigstein, P.; Torkelson, J. M. Polymer – Nanoparticle Interfacial Interactions in Polymer Nanocomposites : Confinement Effects on Glass Transition Temperature and Suppression of Physical Aging. *J. Polym. Sci. Part B Polym. Phys.* **2006**, *44* (20), 2935–2943. https://doi.org/10.1002/polb.

Robertson, C. G.; Roland, C. M. Glass Transition and Interfacial Segmental Dynamics in Polymer-Particle Composites. *Rubber Chem. Technol.* **2008**, *81* (3), 506–522.

Rubinstein, M.; Colby, R. *Polymer Physics*; Oxford University Press: New York, 2003.

Rubio, N.; Au, H.; Leese, H. S.; Hu, S.; Clancy, A. J.; Sha, M. S. P. Grafting from versus Graf Ting to Approaches for the Functionalization of Graphene Nanoplatelets with Poly(Methyl Methacrylate). **2017**. https://doi.org/10.1021/acs.macromol.7b01047.

Sacui, I. A.; Nieuwendaal, R. C.; Burnett, D. J.; Stranick, S. J.; Jorfi, M.; Weder, C.; Foster, E. J.; Olsson, R. T.; Gilman, J. W. Comparison of the Properties of Cellulose Nanocrystals and Cellulose Nanofibrils Isolated from Bacteria, Tunicate, and Wood Processed Using Acid, Enzymatic, Mechanical, and Oxidative Methods. *ACS Appl. Mater. Interfaces* **2014**, *6* (9), 6127–6138. https://doi.org/10.1021/am500359f.

Salajkova, M.; Noh, J.; Park, J. H.; Lagerwall, J. P. F.; Schu, C. Cellulose Nanocrystal-Based Materials : From Liquid Crystal Self-Assembly and Glass Formation to Multifunctional Thin Films. *NPG Asia Mater.* **2014**, No. 6, 1–12. https://doi.org/10.1038/am.2013.69.

Seethamraju, S.; Obrzut, J.; Douglas, J. F.; Woodcock, J. W.; Gilman, J. W. Quantifying Fluorogenic Dye Hydration in an Epoxy Resin by Noncontact Microwave Dielectric Spectroscopy. *J. Phys. Chem. B* **2020**, *124* (14), 2914–2919. https://doi.org/10.1021/acs.jpcb.9b11622.

Sharpe, L. H. The Interphase in Adhesion†. *J. Adhes.* **1972**, *4* (1), 51–64. https://doi.org/10.1080/00218467208072210.

Shundo, A.; Okada, Y.; Ito, F.; Tanaka, K. Fluorescence Behavior of Dyes in Thin Films of Various Polymers. *Macromolecules* **2012**, *45* (1), 329–335. https://doi.org/10.1021/ma201901x.

Sinko, R.; Keten, S. Effect of Moisture on the Traction-Separation Behavior of Cellulose Nanocrystal Interfaces. *Appl. Phys. Lett.* **2014**, *105* (24), 243702. https://doi.org/10.1063/1.4904708.

Tatsumi, M.; Teramoto, Y.; Nishio, Y. Polymer Composites Reinforced by Locking-in a Liquid-Crystalline Assembly of Cellulose Nanocrystallites. *Biomacromolecules* **2012**, *13* (5), 1584–1591. https://doi.org/10.1021/bm300310f.

Thielemans, W.; Wohlhauser, S.; Delepierre, G.; Labet, M.; Weder, C.; Zoppe, J. O. Grafting Polymers from Cellulose Nanocrystals : Synthesis , Properties , and Applications. *Macromolecules* **2018**, *51*, 6157–6189. https://doi.org/10.1021/acs.macromol.8b00733.

Tito, N. B.; Lipson, E. G.; Milner, S. T. Soft Matter Lattice Model of Mobility at Interfaces : Free Surfaces ,. *Soft Matter* **2013**, *9*, 9403–9413. https://doi.org/10.1039/c3sm51287h.

Vargas, W.; Avendano, E.; Hernández-Jiménez, M.; Azofeifa, D.; Libby, E.; Solís, Á.; Barboza-Aguilar, C. Photonic Crystal Characterization of the Cuticles of Chrysina Chrysargyrea and Chrysina Optima Jewel Scarab Beetles. *Biomimetics* **2018**, *3* (4), 30. https://doi.org/10.3390/biomimetics3040030.

Velasco-Hogan, A.; Xu, J.; Meyers, M. A. Additive Manufacturing as a Method to Design and Optimize Bioinspired Structures. *Adv. Mater.* **2018**, *30* (52), 1800940. https://doi.org/10.1002/adma.201800940.

Viet, D.; Beck-Candanedo, S.; Gray, D. G. Dispersion of Cellulose Nanocrystals in Polar Organic Solvents. *Cellulose* **2007**, *14* (2), 109–113. https://doi.org/10.1007/s10570-006-9093-9.

Vollick, B.; Kuo, P. Y.; Thérien-Aubin, H.; Yan, N.; Kumacheva, E. Composite Cholesteric Nanocellulose Films with Enhanced Mechanical Properties. *Chem. Mater.* **2017**, *29* (2), 789–795. https://doi.org/10.1021/acs.chemmater.6b04780.

Wallrabe, H.; Periasamy, A. Imaging Protein Molecules Using FRET and FLIM Microscopy. *Curr. Opin. Biotechnol.* **2005**, *16* (1), 19–27. https://doi.org/10.1016/j.copbio.2004.12.002.

Wan, H.; Li, X.; Zhang, L.; Li, X.; Liu, P.; Jiang, Z.; Yu, Z. Z. Rapidly Responsive and Flexible Chiral Nematic Cellulose Nanocrystal Composites as Multifunctional Rewritable Photonic Papers with Eco-Friendly Inks. *ACS Appl. Mater. Interfaces* **2018**, *10* (6), 5918–5925. https://doi.org/10.1021/acsami.7b19375.

Wang, B.; Walther, A. Self-Assembled, Iridescent, Crustacean-Mimetic Nanocomposites with Tailored Periodicity and Layered Cuticular Structure. *ACS Nano* **2015**, *9* (11), 10637–10646. https://doi.org/10.1021/acsnano.5b05074.

Weber, C.; Hoogenboom, R.; Schubert, U. S. Temperature Responsive Bio-Compatible Polymers Based on Poly(Ethylene Oxide) and Poly(2-Oxazoline)S. *Prog. Polym. Sci.* **2012**, *37* (5), 686–714. https://doi.org/10.1016/j.progpolymsci.2011.10.002.

Wohlhauser, S.; Kuhnt, T.; Meesorn, W.; Espinosa, L. M. De; Zoppe, J. O.; Weder, C. One-Component Nanocomposites Based on Polymer-Grafted Cellulose Nanocrystals. *Macromolecules* **2020**, *53* (3), 821–834. https://doi.org/10.1021/acs.macromol.9b01612.

Woodcock, J. W.; Beams, R.; Davis, C. S.; Chen, N.; Stranick, S. J.; Shah, D. U.; Vollrath, F.; Gilman, J. W. Observation of Interfacial Damage in a Silk-Epoxy Composite, Using a Simple Mechanoresponsive Fluorescent Probe. *Adv. Mater. Interfaces* **2017**, *4* (10), 1–5. https://doi.org/10.1002/admi.201601018.

Yao, K.; Meng, Q.; Bulone, V.; Zhou, Q. Flexible and Responsive Chiral Nematic Cellulose Nanocrystal/Poly(Ethylene Glycol) Composite Films with Uniform and Tunable Structural Color. *Adv. Mater.* **2017**, *29* (28), 1–8. https://doi.org/10.1002/adma.201701323.

Zhang, B.; Cheng, Y.; Wang, H.; Ye, B.; Shang, L.; Zhao, Y.; Gu, Z. Multifunctional Inverse Opal Particles for Drug Delivery and Monitoring. *Nanoscale* **2015**, *7*, 10590–10594. https://doi.org/10.1039/c5nr02324f.

Zhang, C.; Peng, H.; Whittaker, A. K. NMR Investigation of Effect of Dissolved Salts on the Thermoresponsive Behavior of Oligo (Ethylene Glycol) -Methacrylate-Based Polymers. *J. Polym. Sci. Part A Polym. Chem.* **2014**, *52*, 2375–2385. https://doi.org/10.1002/pola.27252.

Zhu, B.; Merindol, R.; Benitez, A. J.; Wang, B.; Walther, A. Supramolecular Engineering of Hierarchically Self-Assembled, Bioinspired, Cholesteric Nanocomposites Formed by Cellulose Nanocrystals and Polymers. *ACS Appl. Mater. Interfaces* **2016**, *8*, 11031–11040. https://doi.org/10.1021/acsami.6b00410.

Zoppe, J. O.; Dupire, A. V. M.; Lachat, T. G. G.; Lemal, P.; Rodriguez-Lorenzo, L.; Petri-Fink, A.; Weder, C.; Klok, H. A. Cellulose Nanocrystals with Tethered Polymer Chains: Chemically Patchy versus Uniform Decoration. *ACS Macro Lett.* **2017**, *6* (9), 892–897. https://doi.org/10.1021/acsmacrolett.7b00383.

Zoppe, J. O.; Habibi, Y.; Rojas, O. J.; Venditti, R. A.; Johansson, L. S.; Efimenko, K.; Österberg, M.; Laine, J. Poly(N -Isopropylacrylamide) Brushes Grafted from Cellulose Nanocrystals via Surface-Initiated Single-Electron Transfer Living Radical Polymerization. *Biomacromolecules* **2010**, *11* (10), 2683–2691. https://doi.org/10.1021/bm100719d.

Zoppe, J. O.; Österberg, M.; Venditti, R. A.; Laine, J.; Rojas, O. J. Surface Interaction Forces of Cellulose Nanocrystals Grafted with Thermoresponsive Polymer Brushes. *Biomacromolecules* **2011**, *12* (7), 2788–2796. https://doi.org/10.1021/bm200551p.